AD-A083 222 LOCKHEED MISSILES AND SPACE CO INC HUNTSVILLE AL HUN--ETC F/6 20/5
PLASMA CHEMISTRY PROCESSES IN THE CLOSED CYCLE EDL.(U)
JUL 79 J THOENES, S C KURZIUS DAAH40-78-C-0196
UNCLASSIFIED LMSC-HREC-TR-D568999 DRCPM-HEL-CR-79-11-VOL-1 NL

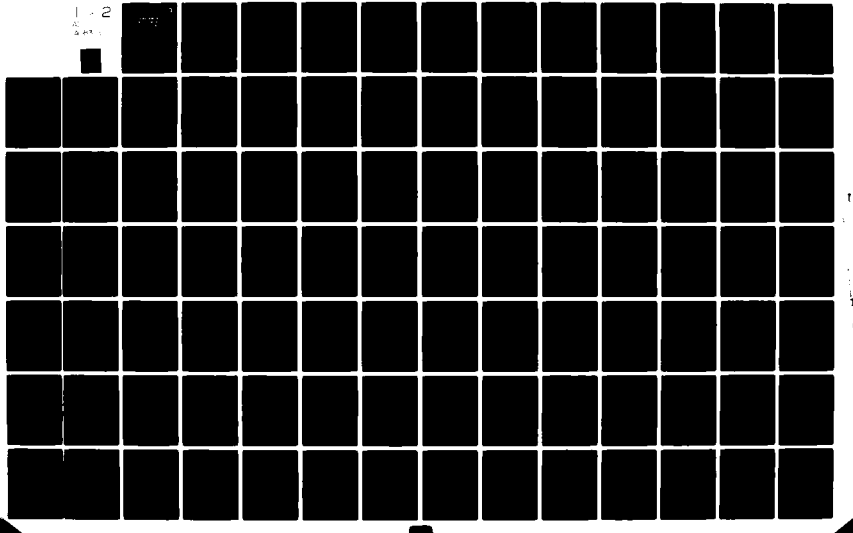

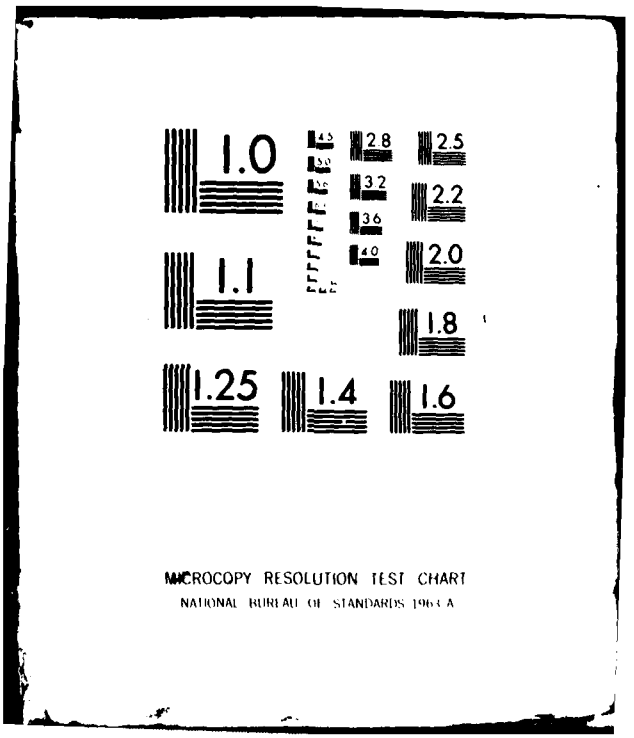
1.0
1.1
1.25
1.4
1.6
1.8
2.0
2.2
2.5
2.8
3.2
3.6
4.0
MICROCOPY RESOLUTION TEST CHART
NATIONAL BUREAU OF STANDARDS 1963 A

Technical Report DRCPM-HEL-CR-79-11

Volume I

PLASMA CHEMISTRY PROCESSES IN THE CLOSED CYCLE EDL

Jürgen Thoenes
Shelby C. Kurzius

Lockheed Missiles & Space Company, Inc.
Huntsville Research & Engineering Center
4800 Bradford Drive, Huntsville, AL 35807

July 1979

Prepared for

Laser Science Directorate
Army High Energy Laser Laboratory
U. S. Army Missile R&D Command, Redstone Arsenal, AL 35809

DISCLAIMER

The findings in this report are not to be construed as an official Department of the Army position unless so designated by other authorized documents.

DISPOSITION INSTRUCTIONS

Destroy this report when it is no longer needed.
Do not return it to the originator.

TRADE NAMES

Use of trade names or manufacturers in this report does not constitute an official endorsement or approval of the use of such commercial hardware or software.

SECURITY CLASSIFICATION OF THIS PAGE (When Data Entered)

REPORT DOCUMENTATION PAGE	READ INSTRUCTIONS BEFORE COMPLETING FORM
1. REPORT NUMBER: TR DRCPM-HEL CR-79-11-Vol-1	3. RECIPIENT'S CATALOG NUMBER
4. TITLE (and Subtitle): PLASMA CHEMISTRY PROCESSES IN THE CLOSED CYCLE EDL	5. TYPE OF REPORT & PERIOD COVERED: Final Report 5 Jul 78 — 5 Jul 79
	6. PERFORMING ORG. REPORT NUMBER: LMSC-HREC-TR-D568999
7. AUTHOR(s): Jürgen Thoenes and Shelby C. Kurzius	8. CONTRACT OR GRANT NUMBER(s): DAAH40-78-C-0196
9. PERFORMING ORGANIZATION NAME AND ADDRESS: Lockheed Missiles & Space Company, Inc. Huntsville Research & Engineering Center Huntsville, Alabama 35807	10. PROGRAM ELEMENT, PROJECT, TASK AREA & WORK UNIT NUMBERS: 1L161
11. CONTROLLING OFFICE NAME AND ADDRESS	12. REPORT DATE: July 1979
	13. NUMBER OF PAGES: 161
14. MONITORING AGENCY NAME & ADDRESS (if different from Controlling Office): Laser Science Directorate Army High Energy Laser Laboratory Redstone Arsenal, AL 35812	15. SECURITY CLASS. (of this report): Unclassified
	15a. DECLASSIFICATION/DOWNGRADING SCHEDULE

16. DISTRIBUTION STATEMENT (of this Report)

Contractual Distribution List Attached

17. DISTRIBUTION STATEMENT (of the abstract entered in Block 20, if different from Report)

This document has been approved for public release and sale; its distribution is unlimited.

18. SUPPLEMENTARY NOTES

19. KEY WORDS (Continue on reverse side if necessary and identify by block number)

Repetitively Pulsed Laser
Electric Discharge
Plasma Chemistry
Closed Cycle Operation

20. ABSTRACT (Continue on reverse side if necessary and identify by block number)

Theoretical modeling of plasma chemistry effects on the performance of closed cycle, pulsed, electron beam sustained electric discharge lasers is described. The one-dimensional model considers the mutual interaction of the electron beam, the discharge, the plasma and laser radiation. The most important processes are modeled in terms of experimentally controllable parameters which include the post-foil electron beam current density, primary electron energy, applied electric potential, electrode spacing, initial gas composition, temperature and pressure, electron beam and discharge pulse width, and laser cavity characteristics. Results obtained for several laser gas mixtures are described and compared with experimental data. A detailed analysis has been made of test cases for closed cycle devices under development, including the effect on performance of variations in the electric field, the electron beam current, and the gas mixture composition. Electrophilic plasma by-products have been identified, and recommendations have been developed for experimental efforts to verify the predictions.

DD FORM 1 JAN 73 1473 EDITION OF 1 NOV 65 IS OBSOLETE

SECURITY CLASSIFICATION OF THIS PAGE (When Data Entered)

FOREWORD

This report presents results of work performed by the Lockheed-Huntsville Research & Engineering Center under Contract DAAH40-78-C-0196, for the U.S. Army Missile R&D Command, Redstone Arsenal, Alabama.

This work was jointly monitored by Mr. Charles M. Cason, Chief, Electric Laser Branch, Army High Energy Laser Center (Prov.), and Capt. John Filcoff of the Electric Laser Branch, Air Force Weapons Laboratory. The period of performance covered by this report was from 5 July 1978 through 5 July 1979.

This is Volume I of a two-volume report.

- "Plasma Chemistry Processes in the Closed Cycle EDL," Volume I
- "EDLAMP User's Manual," Volume II.

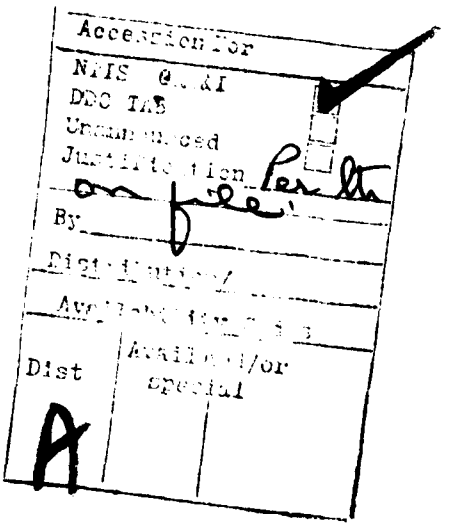

CONTENTS

LIST OF TABLES

LIST OF FIGURES

1. INTRODUCTION AND SUMMARY

Closed cycle operation of CO_2 electric discharge lasers has been shown to be substantially influenced by the presence of molecular species with high electron attachment cross sections, negative ions which increase the plasma heating, and species which efficiently deactivate the upper laser level (Refs. 1 and 2). Depending on the origin of these electrophilic species we can distinguish basically three kinds. First, impurities which are certain trace species present in the initial laser gas mixture before the discharge. Second, outgassing and material degradation of the device hardware produce what we shall call contaminants. Finally, plasma by-products are produced from the ideal laser gas mixture during and after the discharge due to plasma chemistry. The present study is mainly concerned with plasma by-products and, to some degree, with initial impurities and their influence on laser performance.

The plasma chemistry important in the formation of these by-products has been studied in greatest detail for $He/N_2/CO_2$ mixtures loaded by a dc discharge. The Army and the Air Force are currently pursuing methods for eliminating helium mixtures in repetitively pulsed laser systems. Thus, particularly for closed cycle operation, there exists interest in determining dominant processes detrimental to sustained repetitive high energy density pulsed loading of generic $H_2/N_2/CO_2$ laser mixtures which might also contain CO, H_2O or other species characteristic of hydrocarbon fuel combustion products.

The purpose of the effort described here was to identify chemical reactions leading to the generation of plasma by-products in several laser gas mixtures, to determine the relative importance of the various plasma by-products in degrading assessed laser performance, and to furnish predictions of all important molecular species production and decay rates during and following

the electrical pulse. In doing this, maximum use was to be made of existing kinetic data and of the existing continuous wave electric laser code previously developed by the authors (Ref. 3).

Furthermore, the steady state buildup of byproduct concentrations under repetitively pulsed operations was to be examined, and key experimental efforts to verify predicted results were to be recommended.

The essential features of the modeling approach used in this effort are described in Section 2. The discussion includes the basic equations as well as some details of the plasma kinetics model employed. Results obtained for several laser gas mixtures are described and compared with experimental data in Section 3. The good agreement achieved lends credibility to the theoretical model and suggests that application of the analysis to other laser gas mixtures may be made with confidence.

Section 4 presents a detailed analysis of test cases for two closed cycle EDL devices currently under development. The study includes the effects on performance of variations in the electric field, the effective electron beam current, gas mixture composition, cycle simulation and gas contamination by water vapor.

Section 5 presents the conclusions derived from the work accomplished. Also presented are recommendations for key experimental efforts that should be undertaken to verify predicted results as well as for future theoretical efforts that should be performed to improve the computer model.

Briefly summarizing, a theoretical model is presented which can be used to analyze plasma chemistry effects on the performance of pulsed, electron beam sustained electric discharge lasers. The one-dimensional model contains descriptions of the configuration components of primary importance which are the electron beam, the discharge, the plasma and its composition, laser radiation, and their mutual interaction. All important processes are modeled in terms of experimentally controllable parameters which include

the post-foil electron beam current density, the primary electron energy, the applied electric field potential, discharge electrode spacing, initial laser gas composition, temperature and pressure, both electron beam and electric discharge pulse widths and relative sequencing, as well as cavity geometric data such as mirror reflectivities, transmissivities and gain length.

Finally, a complete list of rate mechanisms and coefficients as used in this work is presented in an Appendix to this report.

2. MODELING APPROACH

2.1 CAVITY DISCHARGE MODEL

This section presents a brief description of the essential features which a theoretical model must possess to adequately describe plasma chemistry processes in pulsed electric discharge lasers. This model incorporates descriptions of the electron beam, the discharge, the plasma composition and laser radiation, and their mutual interaction. The effect of both single and repetitive pulsing can be modeled. To simulate selective removal of detrimental species (scrubbing) the plasma composition can be modified between successive pulses when recirculation and repetitive pulsing are to be considered. Modeling as many of the basic features of a device as possible serves to minimize simplifying assumptions which always have to be made. One such simplification made in this work is the assumption of spatially uniform conditions in the cavity resulting in a one-dimensional model. On the other hand, this analysis fully couples the energy equation into the system of species rate equations, eliminating the often made assumption that variations in the gas temperature, which is of prime importance to laser operation, can be ignored.

Considering uniformly excited laser cavity volumes of the order of a few liters, and electric discharge pulses of approximately microsecond duration it can easily be shown that a constant density, time-dependent treatment of the plasma chemistry should adequately describe the important processes occurring in a pulsed discharge. For repetitively pulsed discharges and closed loop operation of the laser, the flow velocity around the cycle is assumed to be sufficiently small that pressure changes due to varying flow velocity can be neglected. Plasma composition changes around the recirculation loop can then be treated in the same time-dependent manner as in the cavity, provided that post-discharge expansion of the plasma as well as cooling by heat exchangers is appropriately accounted for.

The laser gas mixture consists of neutral and charged particles, vibrationally and electronically excited particles, and electrons. Therefore a multitude of species must be tracked during the calculations. It is assumed that different quantum states of various particles can be treated as separate species. For simplicity, it is also assumed that a single vibrational-rotational radiative transition sufficiently accounts for laser output. While not generally true, this is a reasonable assumption if lasing of the CO_2 molecule is considered.

The model outlined in this section adequately represents phenomena occurring in the positive column. While a detailed description of cathode sheath phenomena is outside the scope of this work, a procedure will be outlined at the end of this section which permits us to estimate the effect of heating in the cathode sheath on plasma chemistry and the generation of plasma byproducts.

Under the above stated assumptions the basic governing equations can be written as follows:

Continuity:

$$\frac{d\rho}{dt} = 0 \tag{1}$$

Species:

$$\rho \frac{dF_i}{dt} = \dot{w}_i + (\delta_{i1} - \delta_{i2}) \frac{\alpha I}{\epsilon} \tag{2}$$

Here ρ denotes the density, F_i the mol/mass ratio of the i^{th} species, and $\dot{w}_i$ its overall net rate of production due to any reaction mechanism except for radiation. For an arbitrary reaction of the form

$$\sum_{i=1}^{N} \nu_i' A_i \rightleftharpoons \sum_{i=1}^{N} \nu_i'' A_i \tag{3}$$

the net rate of production for any participating species for which $\nu_i'' - \nu_i' \neq 0$ can be written as

$$\dot{w}_i = (\nu_i'' - \nu_i') \left\{ k_f \prod_{i=1}^{N} (\rho F_i)^{\nu_i'} - k_b \prod_{i=1}^{N} (\rho F_i)^{\nu''} \right\} \tag{4}$$

where k_f and k_b denote the forward and backward rate constant, respectively. By the law of mass action, this formulation presumes thermal equilibrium of the species at a temperature, T (or electron energy, u). The rate constants are then functions of T (or u).

Laser radiation, its intensity denoted by I, depletes the upper laser level and replenishes the lower laser level, as indicated by the Kronecker symbols in Eq. (2). Gain and photon energy are denoted by α and ϵ, respectively.

Energy:

$$\frac{d}{dt}(\rho e) = j_D E - \kappa \bar{\alpha} I \tag{5}$$

which simply states that any change of internal energy of the laser gas is due to discharge energy pumped into the plasma, or due to radiation leaving the gas in the cavity. Here j_D denotes the drift field current density and E the electric field strength. The quantity κ represents a correction factor and is defined as

$$\kappa \equiv \frac{1 - \exp(-\bar{\alpha}L)}{\bar{\alpha}L} \tag{6}$$

where $\bar{\alpha}$ is the cavity threshold gain. The set of governing equations is completed by adding an equation of state. Species thermodynamic data including specific heats, entropy and enthalpy are used in tabular form for all species considered.

Assuming a Fabry-Perot cavity, the threshold gain can be expressed in terms of mirror reflectivities and optical path length through the gain medium as

$$\bar{\alpha} = -\frac{\ell n(r_1 r_2)}{2L} \tag{7}$$

Note that for $\bar{\alpha}L \ll 1$, which is most often the case, κ reduces to unity. Lasing commences when the medium gain exceeds the cavity gain, and ceases when the pumping reactions fail to maintain the medium gain at the cavity gain level.

The medium gain can be expressed as

$$\alpha = \rho \epsilon (S_{21} F_2 - S_{12} F_1) V \tag{8}$$

where F_2 and F_1 are the mol/mass ratios of the upper and the lower laser level, respectively. All spectroscopic data enter the equation through S_{21} and S_{12} which are functions of temperature only. V denotes the Voigt function which basically represents a generalized line shape function,

$$V(\eta) = \exp(\eta^2) [1 - \mathrm{erf}(\eta)] \tag{9}$$

with η being the ratio of the Lorentz line width to the Doppler line width, i.e.,

$$\eta = (\ell n 2)^{1/2} \frac{\Delta\nu_L}{\Delta\nu_D} \tag{10}$$

The set of basic equations is completed by the equation of state,

$$p = \rho \Re T \sum_{i=1}^{NS} F_i \tag{11}$$

which determines the pressure as a function of density, temperature and gas composition.

Energizing the laser gas in an electric discharge requires the presence of free electrons which are, at least initially, here assumed to be generated by electron-beam ionization. Assuming that both the effective electron-beam current density, j_{EB}, and the effective electron beam energy, E_{EB}, are specified, the number density of primary electrons in the laser gas can be expressed as

$$n_{EB} = \frac{j_{EB}}{q_e V_{EB}} \tag{12}$$

where q_e is the electron charge, and V_{EB}, the relativistic electron beam velocity, is given by

$$V_{EB} = c\left[1 - \left(\frac{E_{EB}}{E_{REF}} + 1\right)^{-2}\right]^{1/2} \tag{13}$$

Here c denotes the speed of light, and E_{REF} the electron rest mass energy equivalence ($m_e c^2$ = 511 keV). Knowing the primary electron density, the rate of ionization and production of secondary electrons due to the electron beam only can be determined according to the reaction

$$A_i + n_{EB} \xrightarrow{k_{f,i}} A_i^+ + n_e + n_{EB} \tag{14}$$

where the primary ionization rate constant, $k_{f,i}$, can be evaluated as a function of the ion mass, the beam ionizing power and the beam electron velocity (Section 2.2).

The drift field current density, and therefore the energy which can be pumped into the gas, is proportional to the number of free electrons and their drift velocity such that, to good approximation,

$$j_D = n_e q_e V_D \tag{15}$$

The drift velocity, V_D, is a function of the gas mixture composition and the electric field/density ratio. It is obtained from an evaluation of the electron energy distribution function (Boltzmann code, see Section 2.2) and can be expressed as

$$V_D = C_1 + C_2\left(\frac{E}{N}\right)^n \tag{16}$$

The volumetric rate of energy addition in the discharge can then be expressed as

$$j_D E = n_e q_e E\left[C_1 + C_2\left(\frac{E}{N}\right)^n\right] \tag{17}$$

where C_1, C_2 and n are mixture dependent constants.

Equation (17) is not only used to evaluate the energy added in the discharge but also to determine the secondary electron energy which is essential in evaluating electron impact excitation rates. Postulating a basic electron impact excitation mechanism as

$$A_i + e \xrightarrow{k_{f,i}} A_i^* + e \tag{18}$$

the power consumed by this mechanism can be expressed as

$$\Delta P = \sum_i n_e n_i k_{f,i} \Delta H_i \tag{19}$$

where the summation indicates that more than one mechanism may be involved. In fact, as will be seen later (see Section 2.2) the summation extends over excitation mechanisms including vibrational excitation, electronic excitation, and ionization. The $k_{f,i}$ which appear here are those which normally result from a full Boltzmann analysis of electron kinetics in the primary laser gas but exclusive of electron kinetics in the plasma discharge byproducts.

Applying conservation of energy by equating the right-hand sides of Eqs. (17) and (19) then leads to the important relation

$$q_e E\left[C_1 + C_2\left(\frac{E}{N}\right)^n\right] = \sum_i n_i k_{f,i} \Delta H_i \tag{20}$$

Since the impact excitation rate constants, $k_{f,i}$ can be expressed as functions of the electron energy which itself is a function of E/N, Eq. (20) constitutes an implicit relation for the electron energy, and simultaneously states its functional dependence on E/N in terms of input functions. It is through Eq. (20)

that coupling of the Boltzmann code and the discharge calculations is put into effect. If all electron excitation mechanisms considered in the Boltzmann code are included on the right-hand side of Eq. (20), the average electron energy iteratively computed from Eq. (20) will accurately compare with the average electron energy computed by the Boltzmann code for the given E/N.

The reason for using the Boltzmann code in terms of Eq. (20) is both historical and practical. In earlier work we did not have a Boltzmann code. We therefore had to fit available results which then led to Eq. (20). The practical reason for retaining this approach is the fact that the Boltzmann code requires more than twice the core storage used by the remainder of the analysis rendering inclusion of the Boltzmann code as a subroutine both costly and impractical.

Equations (1) through (20), in conjunction with a detailed set of reactions and rate coefficients, to be discussed in Section 2.2, provide the basic framework to evaluate plasma conditions in the positive column of the discharge as a function of time, and if desired, the radiative output of the laser cavity.

In the remainder of this subsection an approach will be outlined to assess plasma chemistry effects in the electrode sheaths. Because the heating in the anode sheath is not intense (Ref. 2) we can confine our considerations to the cathode fall region.

In the thin cathode sheath region, the local heating rate is very high. This produces a relatively high local pressure initially, and interferograms indicate that changes of density are small initially (Ref. 4). Owing to the high temperatures which accompany heating near the cathode it can be expected that heat transfer from the gas to the cathode cannot be ignored. On the other hand, as pointed out by Long (Ref. 5) convective cooling of the cathode sheath can be ignored if the flow velocity in the positive column is small enough. Ignoring convective cooling therefore is consistent with our model presented here. In order to compute the gas composition in the sheath, knowledge of the temperature in that region is most important. According to

Ref. 5, the maximum temperature rise in the cathode sheath as a function of bulk energy input and heat transfer to the cathode can be estimated from

$$T_c - T_o = \frac{1}{6} \frac{\dot{Q} d_c^2}{k_o} \tag{21}$$

where T_c is the maximum temperature in the sheath, T_o is the cathode wall temperature, k_o is the thermal conductivity of the gas, and d_c is the cathode sheath thickness. $\dot{Q}$ represents the bulk energy input into the cathode sheath. Assuming current continuity, $\dot{Q}$ is given by

$$\dot{Q} = j_D E_c \tag{22}$$

where j_D is the discharge current density, and E_c represents the average electric field in the cathode sheath.

To compute the temperature increase according to Eq. (21) the cathode sheath thickness and the cathode fall potential must be known. Values for these quantities are, unfortunately extremely scarce. Since the dominant constituent of laser gases of interest here is N_2, and since we can only expect to obtain some more or less qualitative information using this simplified approach anyhow, results presented in the form of Fig. 1 for N_2 will be used to obtain values for the cathode fall potential V_c. In Fig. 1, p_o denotes the reduced pressure at the cathode surface, i.e.,

$$p_o = p \frac{273(K)}{T_o} \tag{23}$$

The procedure described above yields a maximum temperature in the cathode sheath which is in excellent agreement with the example given in Ref. 5.

Having thus determined a representative cathode sheath temperature, the initial pressure is given by the equation of state, assuming constant density. It is reasonable to assume that the relatively high temperature and pressure will promote quick establishment of thermochemical equilibrium.

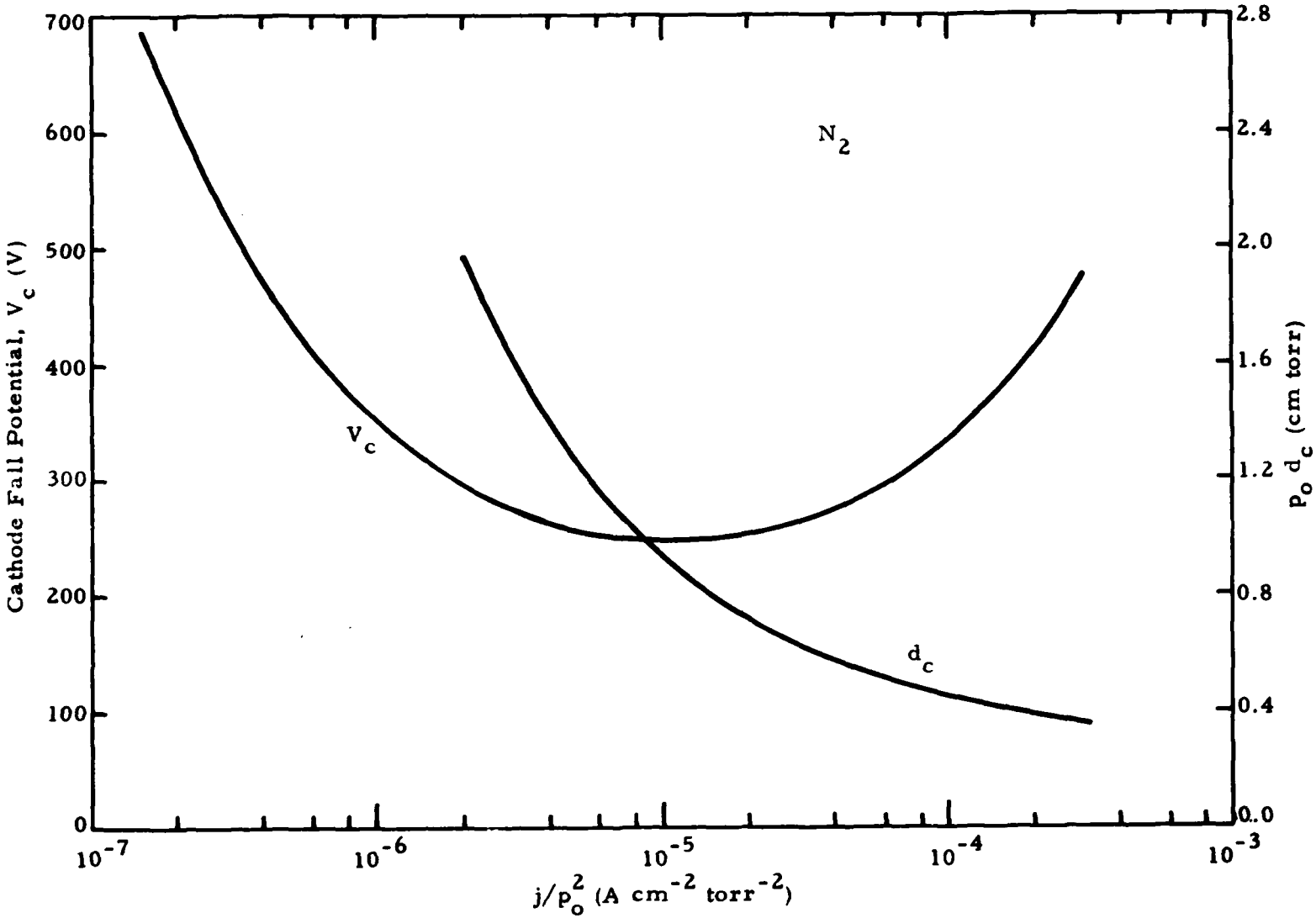

Fig. 1 - Voltage-Current Characteristic and Cathode Fall Distance in N_2 (Ref. 5)

Therefore, under these conditions, the resulting gas composition is easily computed using the CEC program (Ref. 6).

The overall effect of possible contaminants generated in the thin cathode sheath on the plasma chemistry processes occurring in the positive column, which forms the bulk of the discharge, must take into consideration the different conditions involved. Resulting concentrations, averaged over the sheath and the positive column, can be obtained by performing a non-reactive mixing calculation, which defines the average mole fraction of the i^{th} species as

$$\bar{X}_i = \frac{n_{i,p} + n_{i,c}}{\sum n_{i,p} + \sum n_{i,c}} \tag{24}$$

where $n_{i,p}$ and $n_{i,c}$ are the number densities of the i^{th} species in the positive column and in the cathode sheath, respectively. Expressing the number densities in terms of pressure, temperature, volume and mole fraction, Eq. (24) can also be written in the more convenient form

$$\bar{X}_i = \frac{X_{i,p} + X_{i,c} \cdot R}{1 + R} \tag{25}$$

where

$$R = \frac{p_c V_c}{p_p V_p} \left(\frac{T_p}{T_c} \right) \tag{26}$$

Because the volume of the cathode sheath is likely to be orders of magnitude smaller than that of the positive column, and because $T_c >> T_p$ due to heating of cathode gases, we can reasonably expect that $R << 1$, and then Eq. (25) shows that concentrations of plasma byproducts formed in the cathode fall region will have to be extremely large to have a measurable effect on the overall gas composition.

2.2 PLASMA KINETICS

2.2.1 Primary Ionization

In order to obtain high efficiency in electric discharge lasers it has been found that it is advantageous to separate excitation into primary and secondary processes, each tailored to its task. Primary ionization can be realized by various means, most currently using an electron beam.

To predict the yield of secondary electrons due to electron beam ionization according to Eq. (14) we need to know $k_{f,i}$, the primary ionization rate constant. The rate at which secondary electrons are produced may be written as

$$\frac{dn_e}{dt} = \frac{j_{EB}}{q_e} \sum_i \frac{\rho_i}{E_i} \left(\frac{dE}{dm}\right)_i \tag{27}$$

where ρ_i is the mass density of the ith species, E_i is its effective ionization energy, and $(dE/dm)_i$ is the primary electron energy loss rate due to interaction with the ith species of the gas.

From Eq. (14) we obtain similarly

$$\frac{dn_e}{dt} = n_{EB} \sum_i k_{f,i}\, n_i \tag{28}$$

Combining the above two expressions and using Eq. (12) it is found that

$$k_{f,i} = \frac{c}{N_A} \left(\frac{W_i}{E_i}\right) \frac{V_{EB}}{c} \left(\frac{dE}{dm}\right)_i \tag{29}$$

Figure 2 shows V_{EB} and $(dE/dm)_i$ for various species of interest as a function of effective electron beam energy. Noticing that the product of V_{EB} and $(dE/dm)_i$ is a function of E_{EB} as shown in Fig. 3, the primary ionization rate constant $k_{f,i}$ can be expressed as a function of E_{EB} only. Using the curves

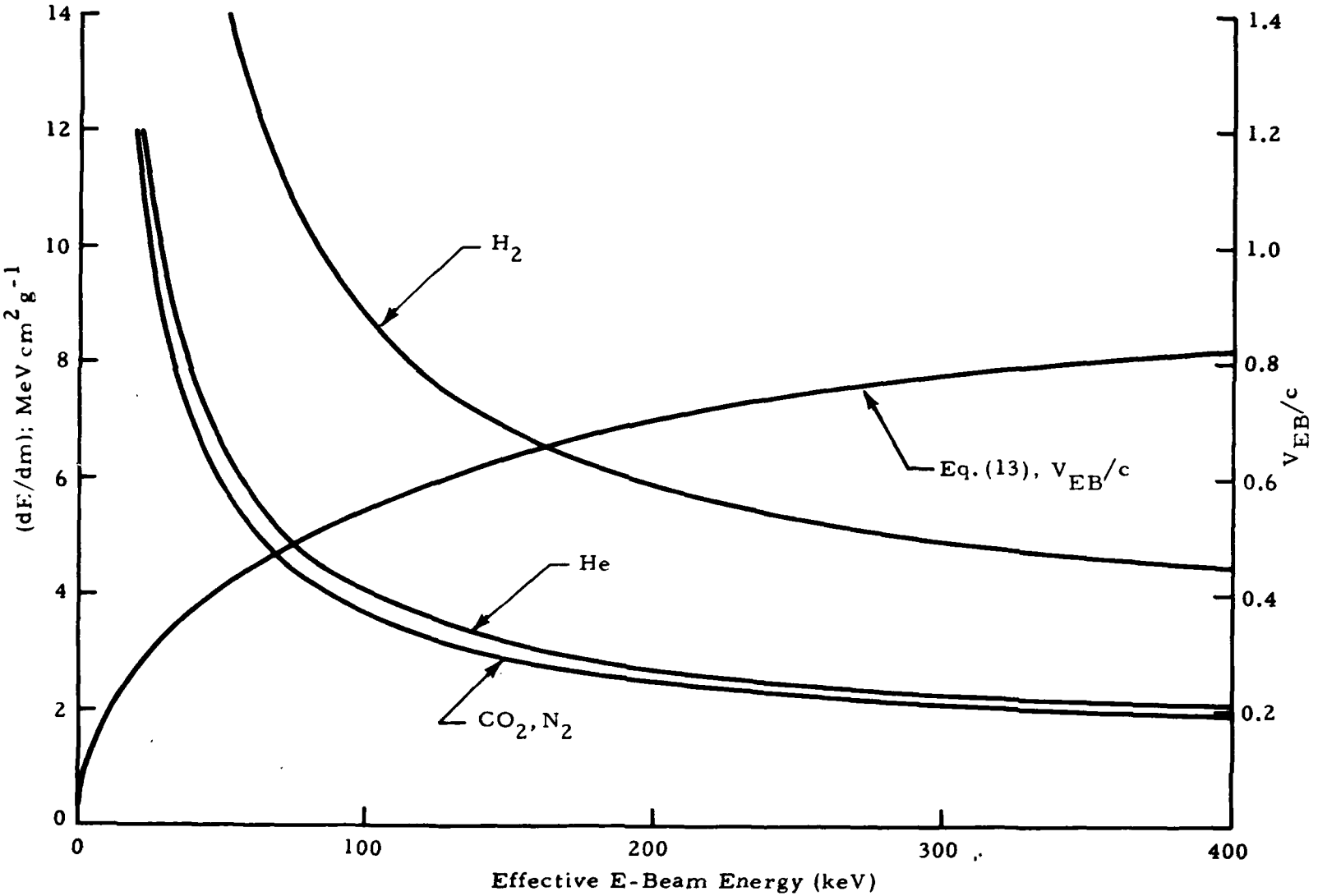

Fig. 2 - Beam Electron Energy, and Electron Energy Loss Rate for Typical Gases (Ref. 7)

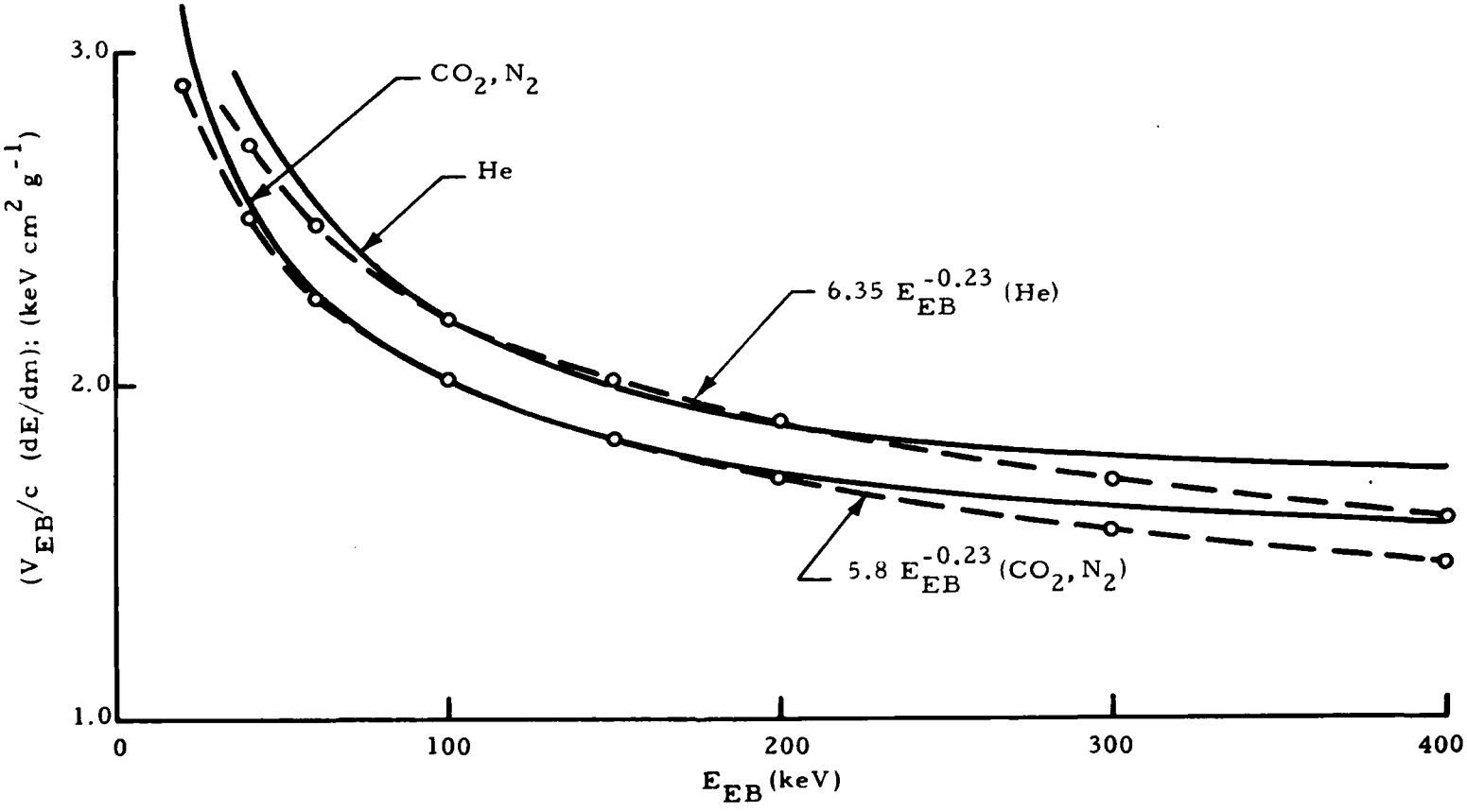

Fig. 3 - Product of Beam Electron Velocity and Electron Energy Loss Rate as a Function of E-Beam Energy for Various Gases

shown in Fig. 3 it is found that an $E_{EB}^{-0.23}$ dependence reproduces those curves to within 5% for $40 \leq E_{EB}$ (keV) ≤ 300.

2.2.2 Secondary Excitation

In order to analyze in quantitative detail the electron, atomic and/or molecular physics of electrically excited laser discharges, it is necessary to accurately determine all of the laser level excitation rates and transport properties which determine the gross properties of these discharges (Ref. 8). To obtain these parameters, knowledge of the electron distribution function is required. Early work assumed that the distribution was Maxwellian, but more recent work has shown this assumption to be incorrect (Ref. 9). Consequently, it is necessary to numerically solve the Boltzmann transport equation for the particular value of E/N and gas mixture in order to obtain accurate values for these excitation rates and transport properties.

The Boltzmann code used in the present work was obtained from the Air Force Weapons Laboratory (Ref. 10). The code uses the method of finite differences to solve the Boltzmann equation for a spatially uniform gas in the presence of a steady electric field, as described by Nighan (Ref. 9). Elastic heating, vibrational excitation, ionization, electronic excitation and disociative attachment processes are included, however, superelastic and electron-electron interactions are not. The electron impact cross sections employed here are the same as computed by Phelps and coworkers (Ref. 11).

The output data consist of the fractional discharge energy transfer to the various excitation modes and the corresponding rate constants as well as several macroscopic parameters such as electron drift velocity, characteristic energy, diffusion coefficient, and effective average electron energy. The latter is defined such that, for a Maxwellian energy distribution, it corresponds to the electron temperature, i.e.,

$$u_e = \frac{2}{3} \int_0^\infty u^{3/2} f(u)\, du \qquad (30)$$

where u denotes electron energy and f(u) is the distribution function. An energy conservation check is performed at the end of each computation to indicate the validity of the results.

This code has been designated primarily for use with CO_2 mixtures. Angularly averaged cross-section data are provided for CO_2, N_2, CO, H_2, O_2 and He. The vibrational levels have been separately considered but several electronic and ionization levels for each gas have been lumped together. Additional modifications have been incorporated in order to obtain consistency between the Boltzmann code and the general kinetic rate model used in the present work. Specifically, to keep the number of reaction mechanisms and species manageable, the consideration of CO_2 vibrational levels is limited to $CO_2(000)$, $CO_2(100)$, $CO_2(0n0$ with n = 1, 2, 3 and $CO_2(001)$. For all diatomic molecules only the first vibrational level is considered in the plasma chemistry aside from the ground level. Since the Boltzmann code considers up to eight vibrational levels for each molecule, simply ignoring the upper levels would have led to an inconsistency in the energy balance. Instead, we added an additional calculation which computes from the rate constants for the upper vibrational levels an energy weighted average rate constant consistent with conservation of energy and the reaction mechanisms used in the plasma chemistry analysis. The number of levels over which the averaging is performed can be selected by the program user depending on how many of the higher vibrational levels of the same molecule are considered in the plasma kinetics.

Transport data consisting of the drift velocity and the average electron energy for various laser gas mixtures are shown in Figs. 4 and 5, respectively. For a given electron density, the drift velocity determines the discharge current density and thus, when multiplied by the electric field strength, determines the volumetric energy addition to the gas in the discharge. For each gas mixture the drift velocity shown in Fig. 4 is curve fitted according to Eq. (16) for use in computing the average electron energy from Eq. (20). The drift velocity

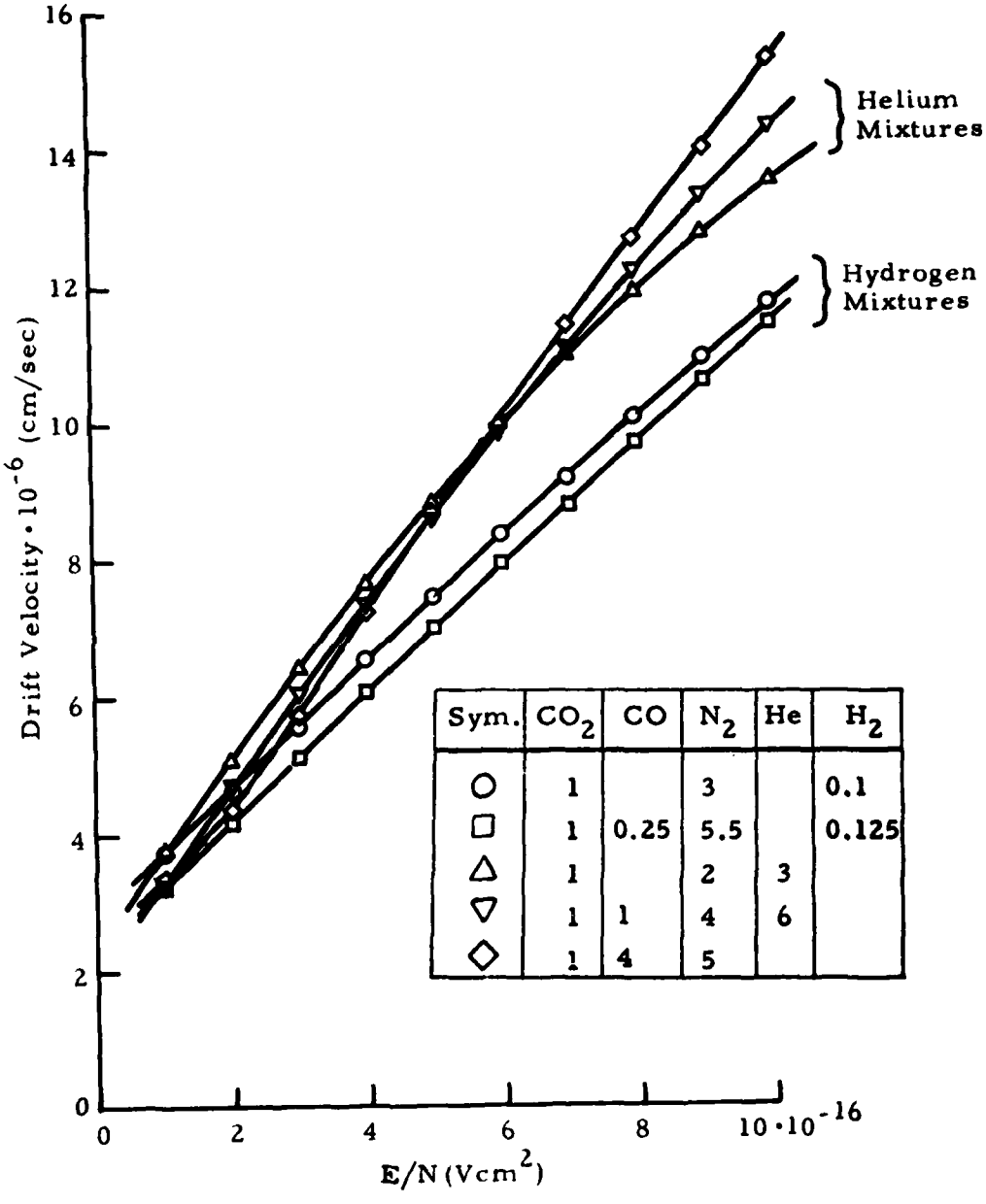

Fig. 4 - Electron Drift Velocity as a Function of E/N for Various Gas Mixtures

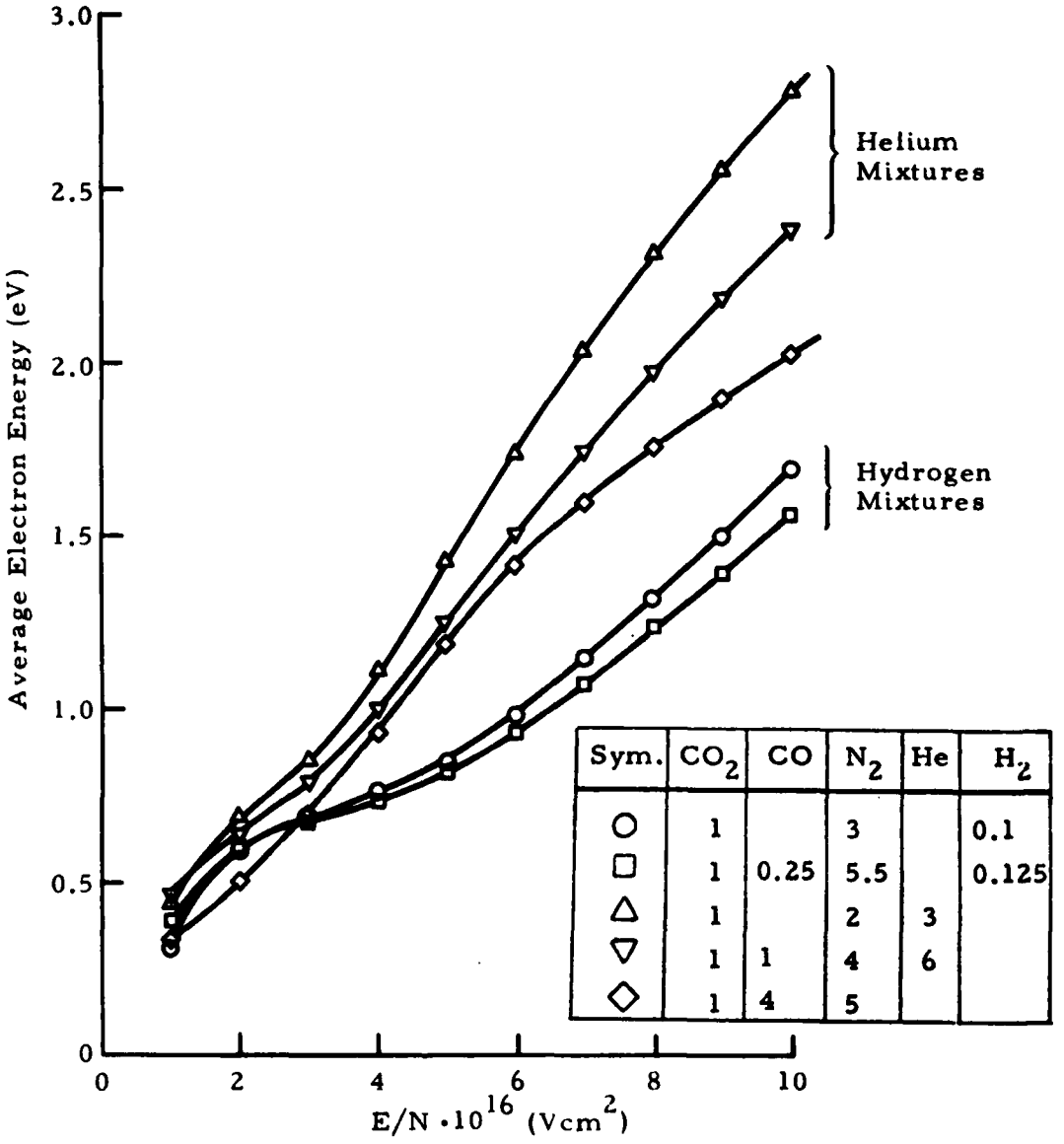

Fig.5 - Average Electron Energy as Function of E/N for Various Gas Mixtures

provides one of the links that couple the Boltzmann code to the plasma chemistry analysis, the other being the impact excitation rates. Drift velocity curve fit coefficients for various gas mixtures are shown in Table 1. These curve fits are very accurate over a wide range of $E/N\,(1 \cdot 10^{-16} \leq E/N\,(Vcm^2) \leq 7 \cdot 10^{-16})$. The relationship between average electron energy and E/N shown in Fig. 5 is not used directly in the analysis but is useful for checking purposes. If all relevant impact excitation mechanisms have been included in determining the average electron energy from Eq. (20), the value obtained will closely agree with the value computed by the Boltzmann code, and shown in Fig. 5 as a function of E/N and gas mixture.

Fractional discharge energy transfer into various excitation levels is shown in Figs. 6 through 9 for a number of different gas mixtures. Although the plasma chemistry analysis makes no direct use of this information, it is illustrative as well as useful in deciding at which value of E/N a given discharge would be most efficient. For this purpose we have shown on each figure that fraction of the discharge energy which is transferred into the upper laser level and into other excitation levels which in turn transfer their energy to the upper laser level. The location of the peak should be a good indication of the optimum E/N value for the discharge. It is interesting to note that the nominal operating value of $E/N = 3.7 \cdot 10^{-16}$ Vcm^2 of the ABEL device (analysis of which is discussed in Section 3) is almost the exact location of the maximum of the respective curve in Fig. 8. It is also observed that mixtures containing H_2 appear to show an optimum value of E/N which is distinctly higher than that for mixtures containing He. Rate constants for the various electron impact excitation mechanisms forming the other link between the Boltzmann code and the plasma chemistry and laser calculations are shown in Figs. 10 through 20. These mechanisms include vibrational excitation, electronic excitation and ionization. Energy transfer into elastic heating is generally very small for the range of E/N of interest here, and is therefore neglected.

For reasons of both simplicity and generality it is desirable to express the various impact excitation rates in terms of a parameter that renders them

Table 1

DRIFT VELOCITY COEFFICIENTS

$$v_D = C_1 + C_2 \left(\frac{E}{N}\right)^n \quad \text{(Eq.16)}$$

Mixture					Coefficients		
CO_2	CO	N_2	He	H_2	C_1	C_2	n
1		2	3		$2.4 \cdot 10^6$	$4.021 \cdot 10^{21}$	0.967
1	1	4	6		$1.6 \cdot 10^6$	$3.858 \cdot 10^{20}$	1.898
1	4		5		$2.0 \cdot 10^6$	$2.620 \cdot 10^{22}$	1.019
1		3		0.1	$3.0 \cdot 10^6$	$3.262 \cdot 00^{23}$	1.102
1	0.25	5.5		0.125	$2.3 \cdot 10^6$	$4.021 \cdot 00^{23}$	1.041

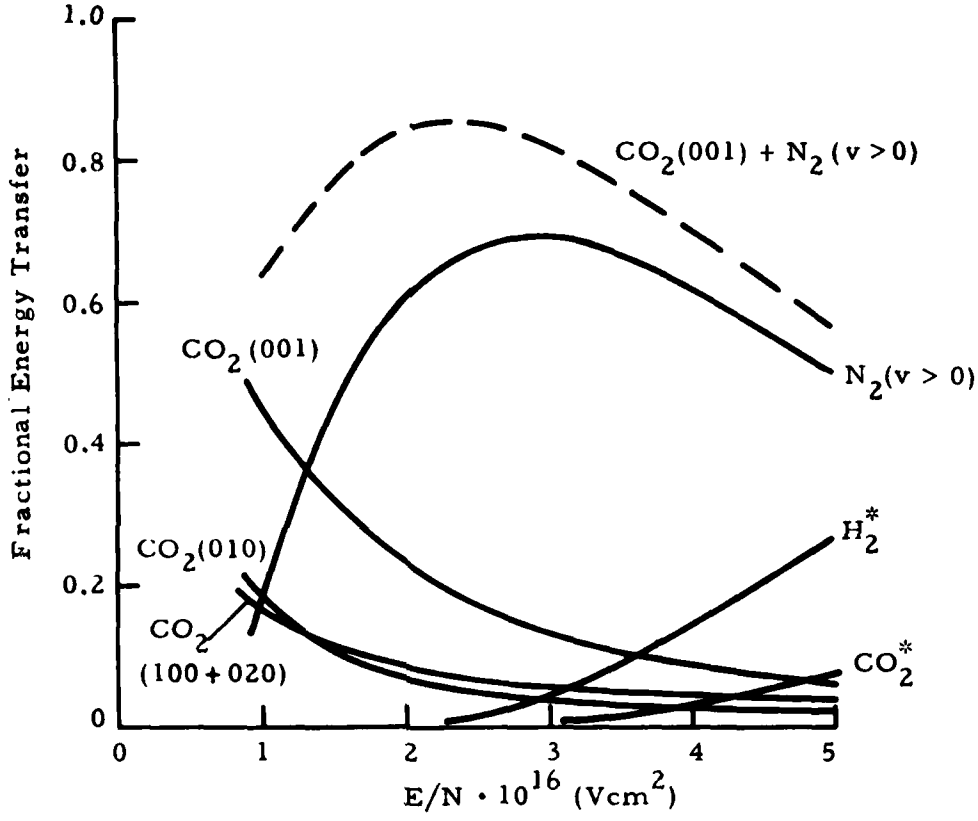

Fig. 6 - Fractional Discharge Energy Transfer into Various Excitation Levels in $CO_2/N_2/He$ = 1/2/3

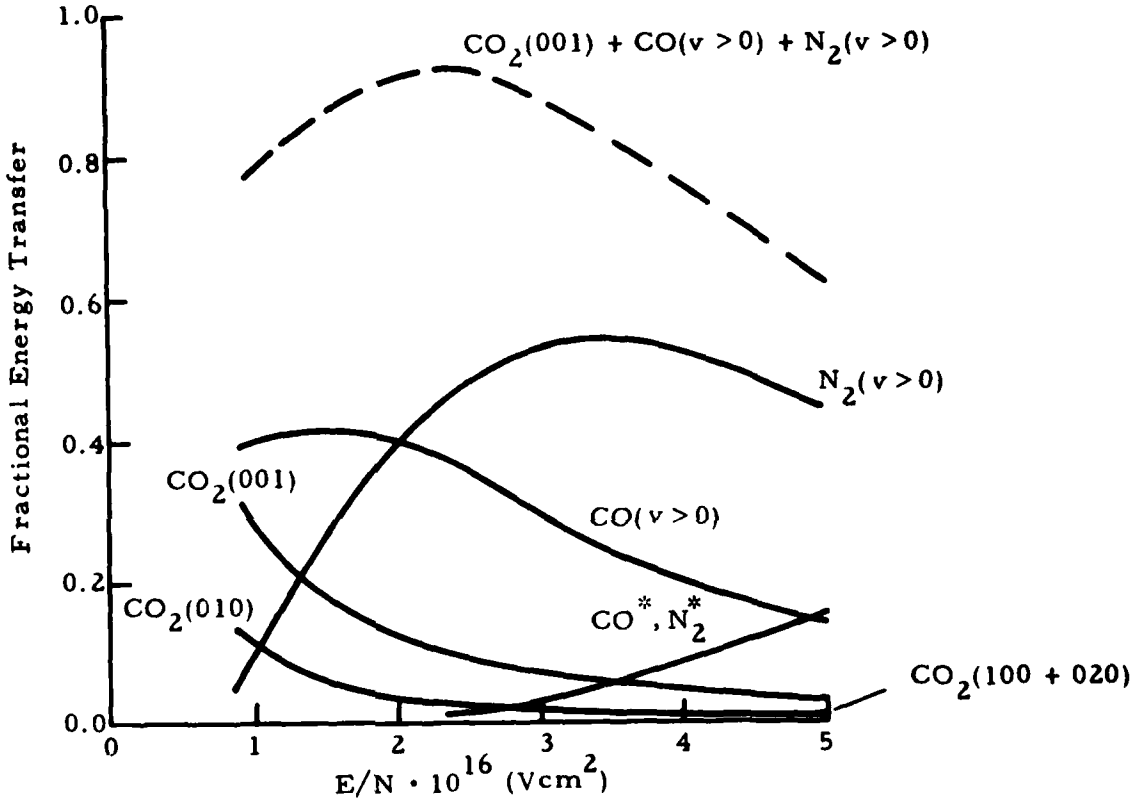

Fig. 7 - Fractional Discharge Energy Transfer into Various Excitation Levels in $CO_2/CO/N_2/He/O_2$ = 1/1/4/6/0.1

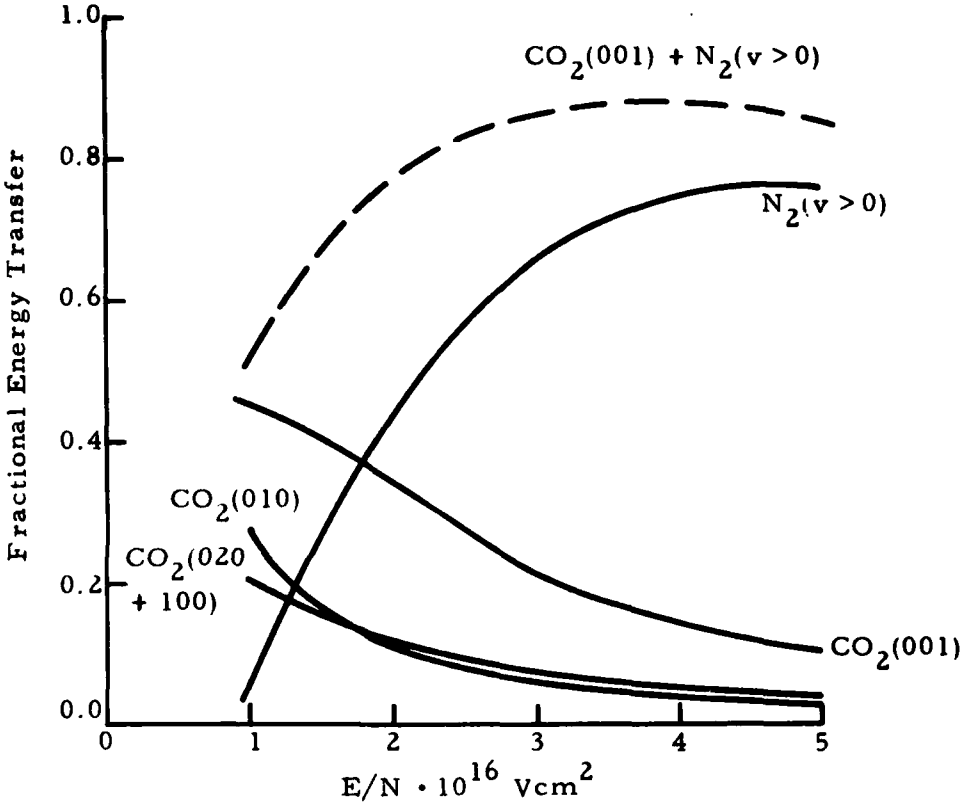

Fig. 8 - Fractional Discharge Energy Transfer into Various Excitation Levels in $CO_2/N_2/H_2$ = 1/3/0.08

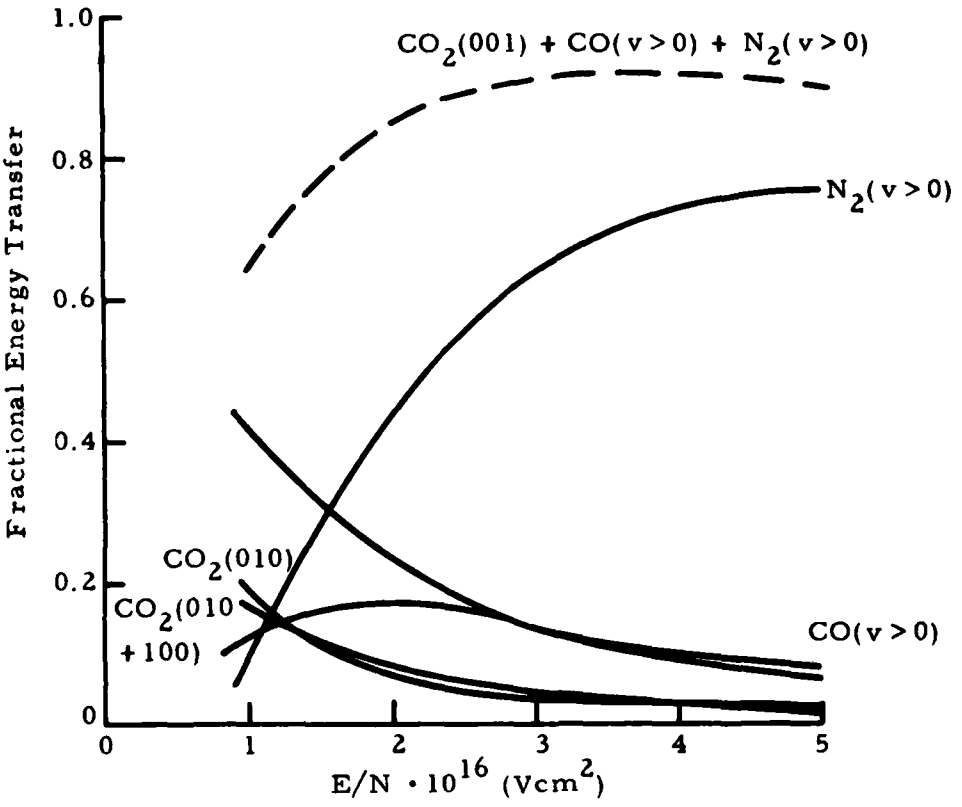

Fig. 9 - Fractional Discharge Energy Transfer into Various Excitation Levels in $CO_2/CO/N_2/H_2$ = 1/0.25/5.5/0.125

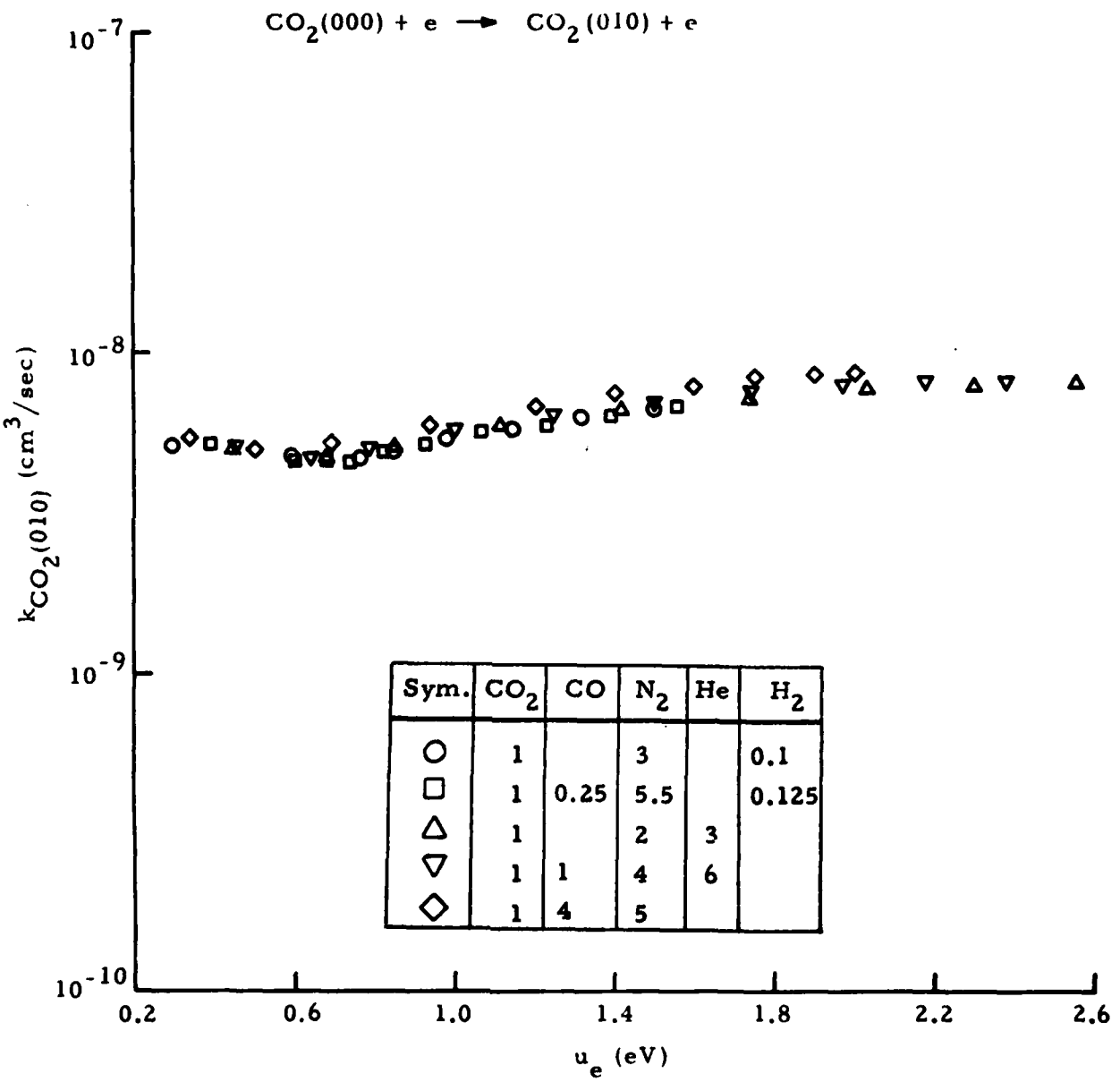

Fig. 10 - Electron Impact Vibrational Excitation Rate of $CO_2(010)$ for Various Gas Mixtures

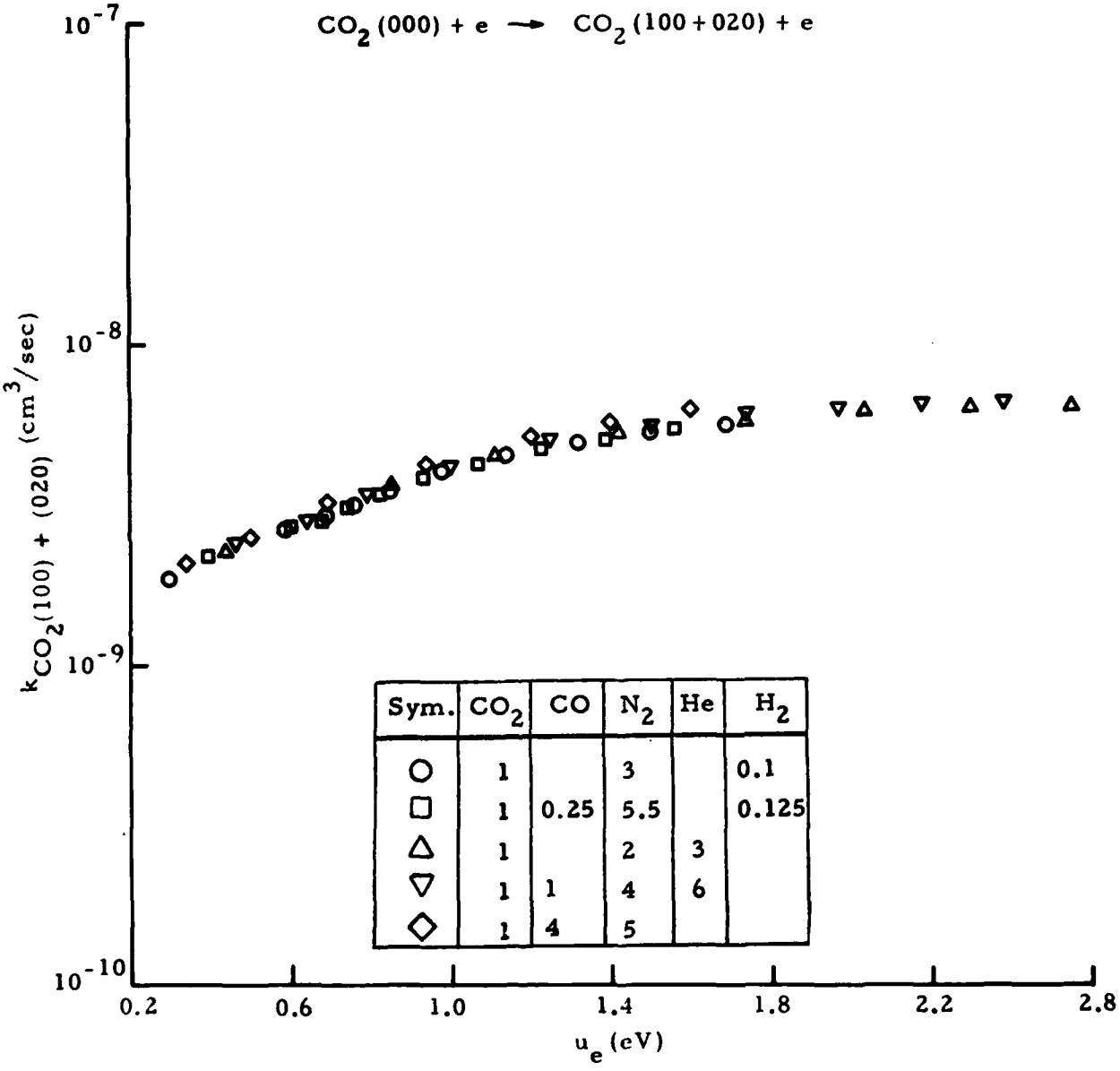

Fig. 11 - Electron Impact Vibrational Excitation Rate of CO_2(100+020) for Various Gas Mixtures

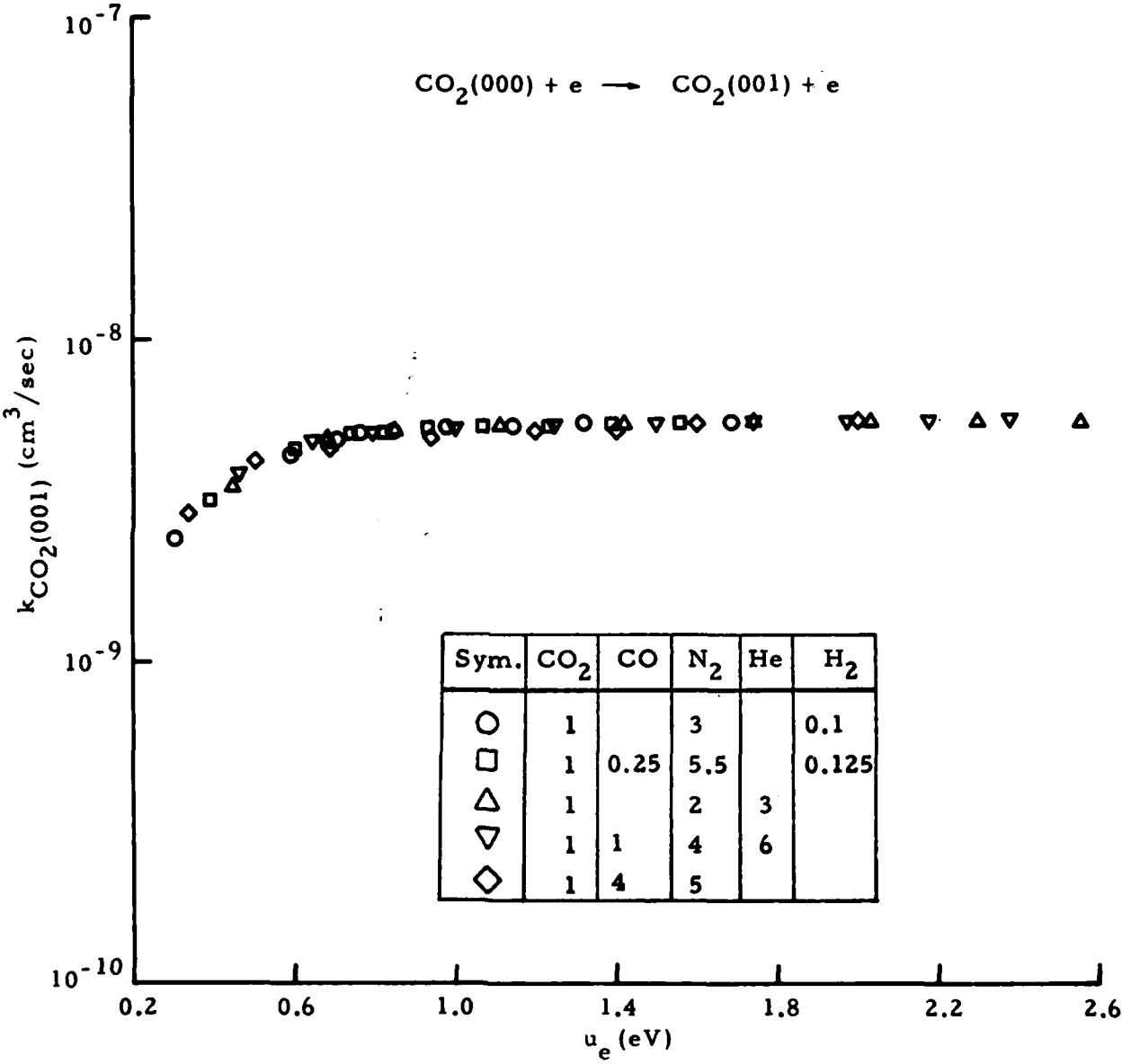

Fig. 12 - Electron Impact Vibrational Excitation Rate of $CO_2(001)$ for Various Gas Mixtures

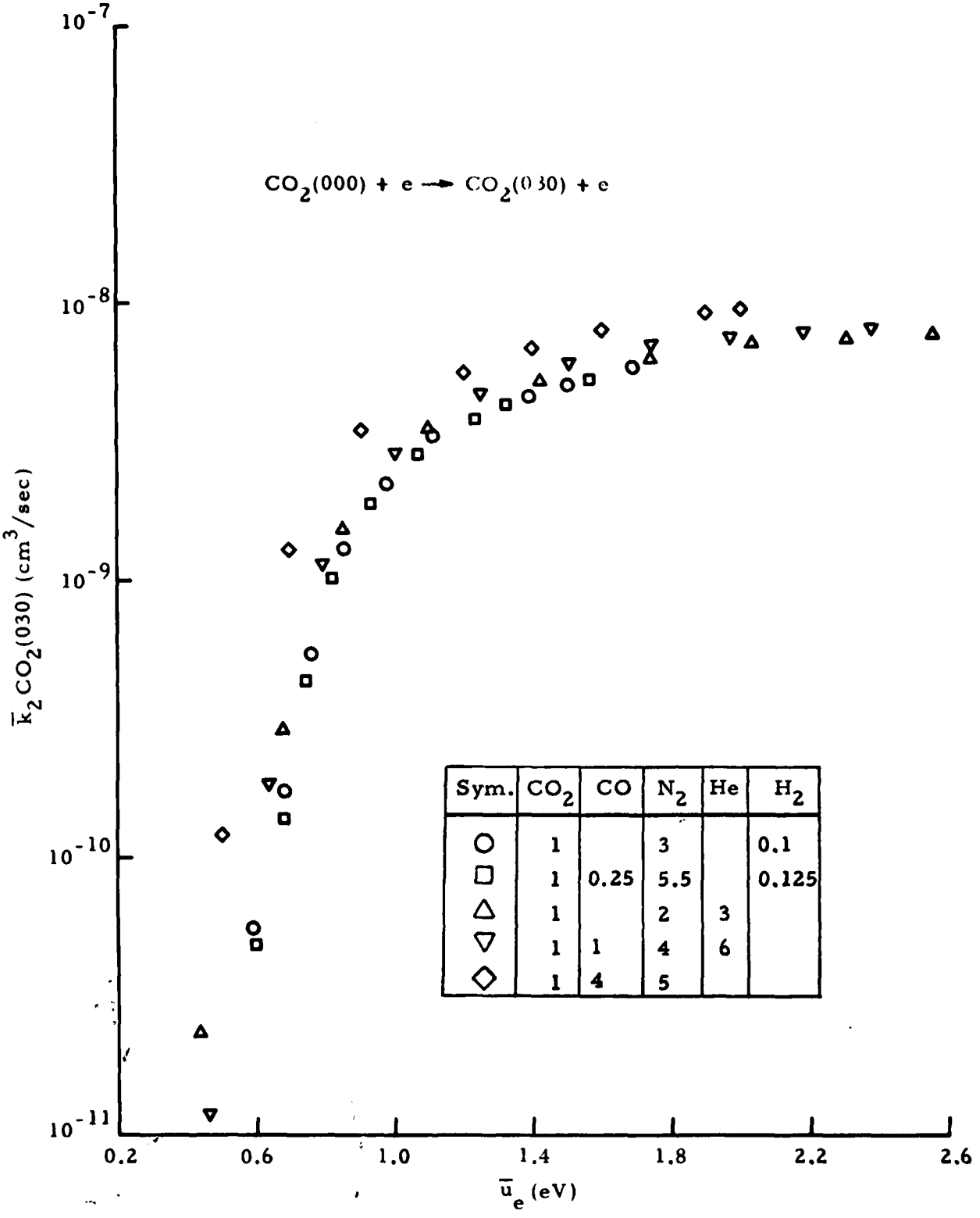

Fig. 13 - Electron Impact Vibrational Excitation Rate of $CO_2(030)$

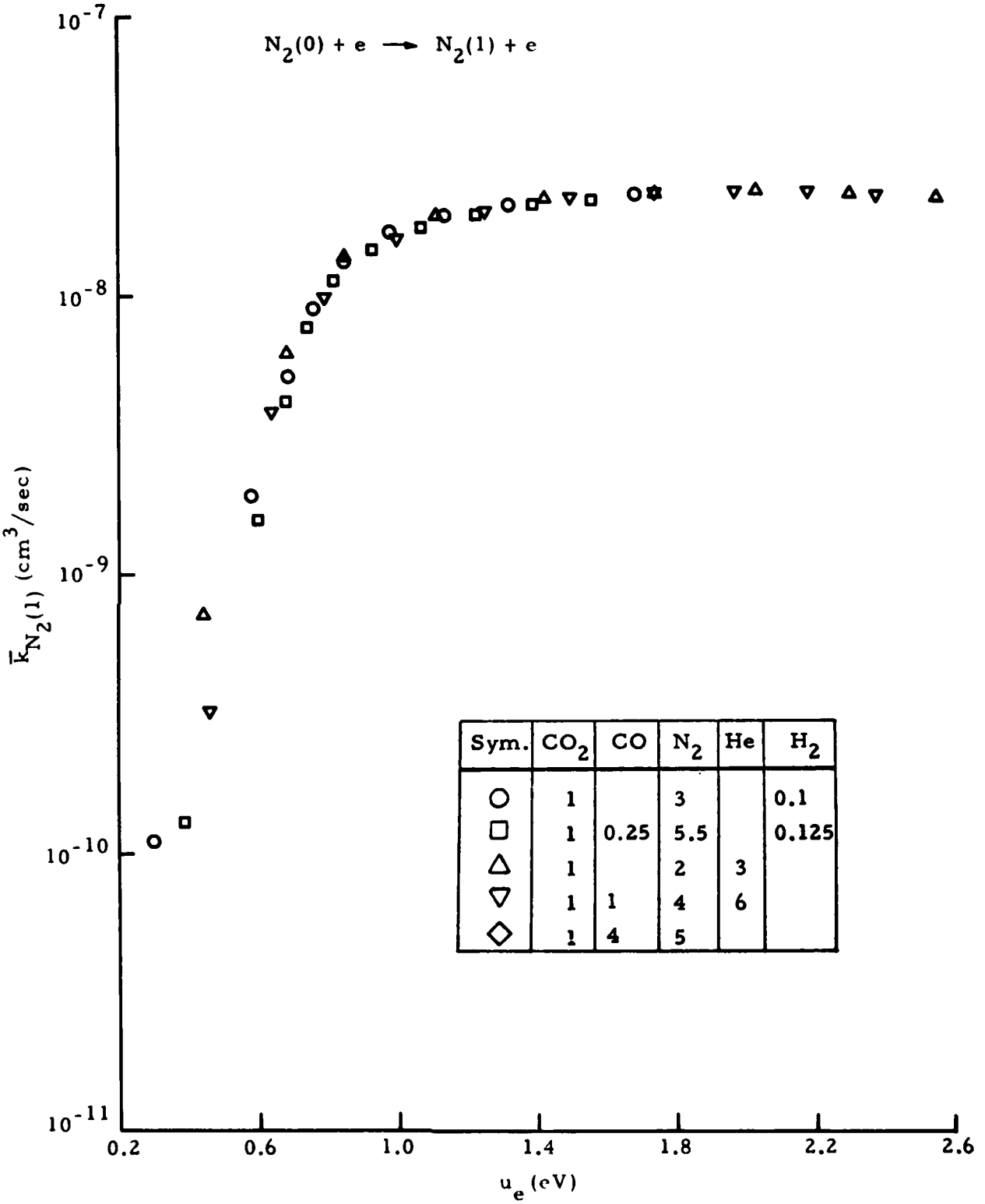

Fig. 14 - Effective Electron Impact Vibrational Excitation Rate of $N_2(1)$ for Various Gas Mixtures (Energy Weighted Average)

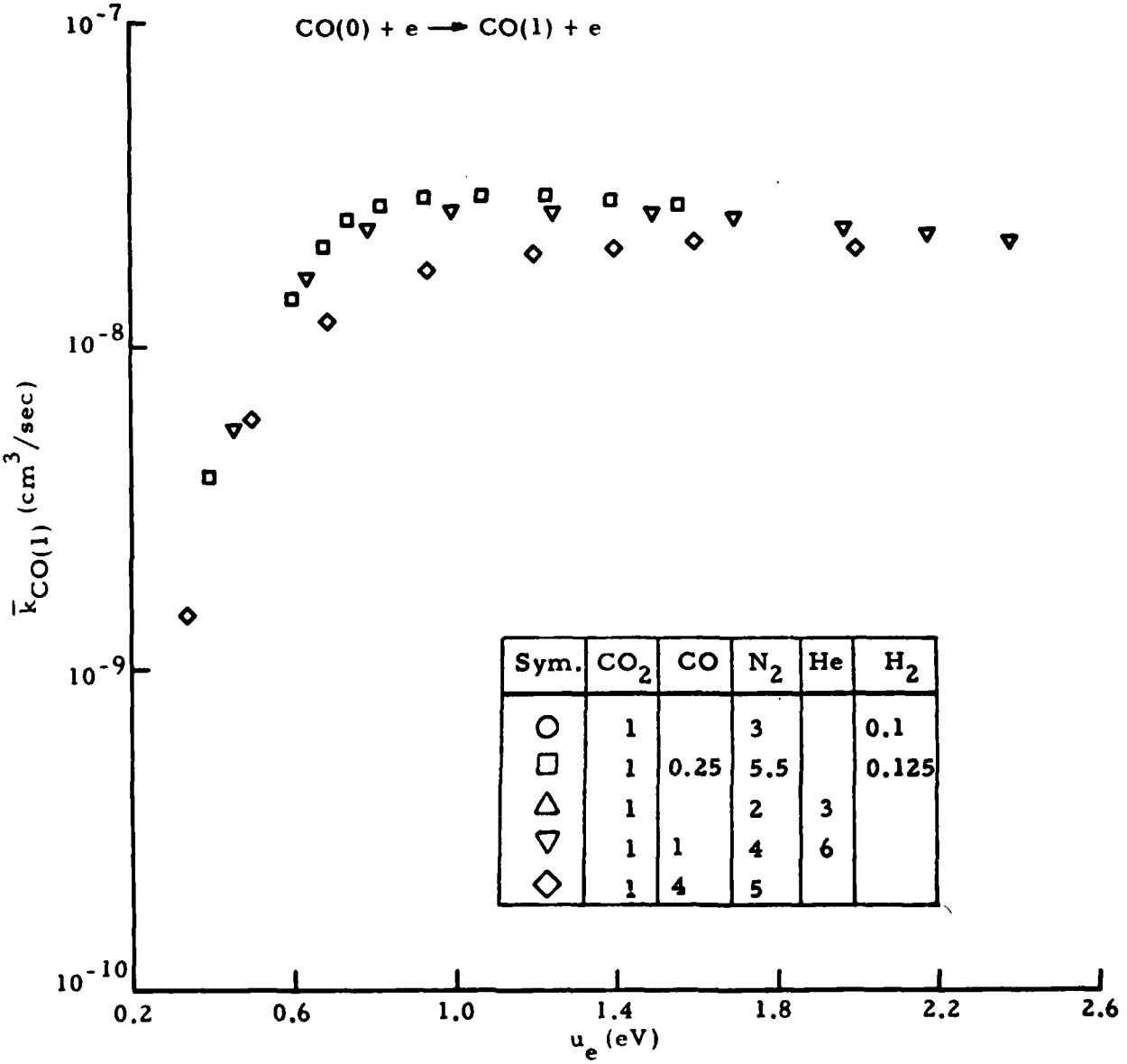

Fig. 15 - Effective Electron Impact Excitation Rate for CO(1)
(Weighted Average CO(1) → CO(8))

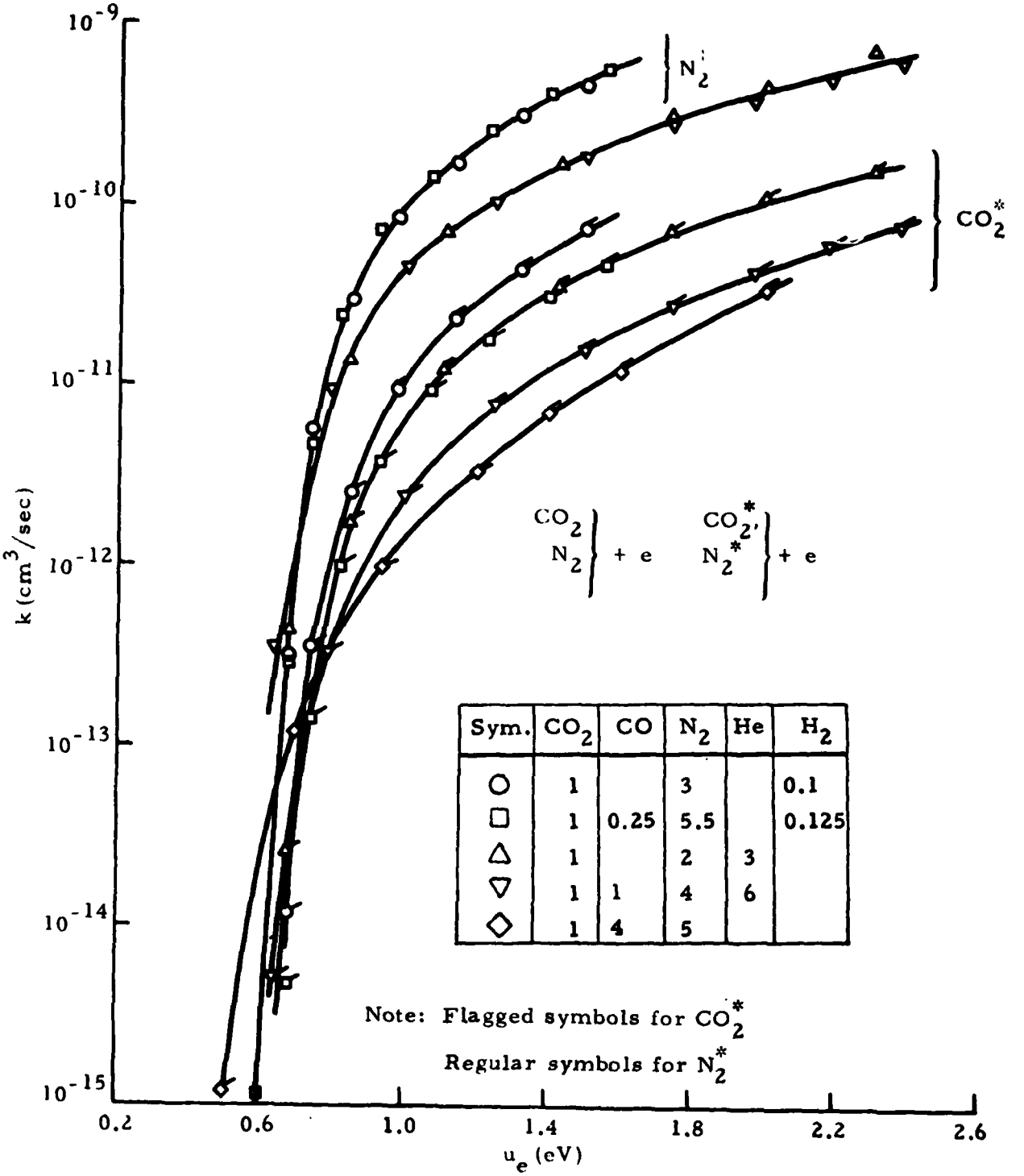

Fig. 16 - Electron Impact Electronic Excitation Rate for CO_2 and N_2 in Various mixtures

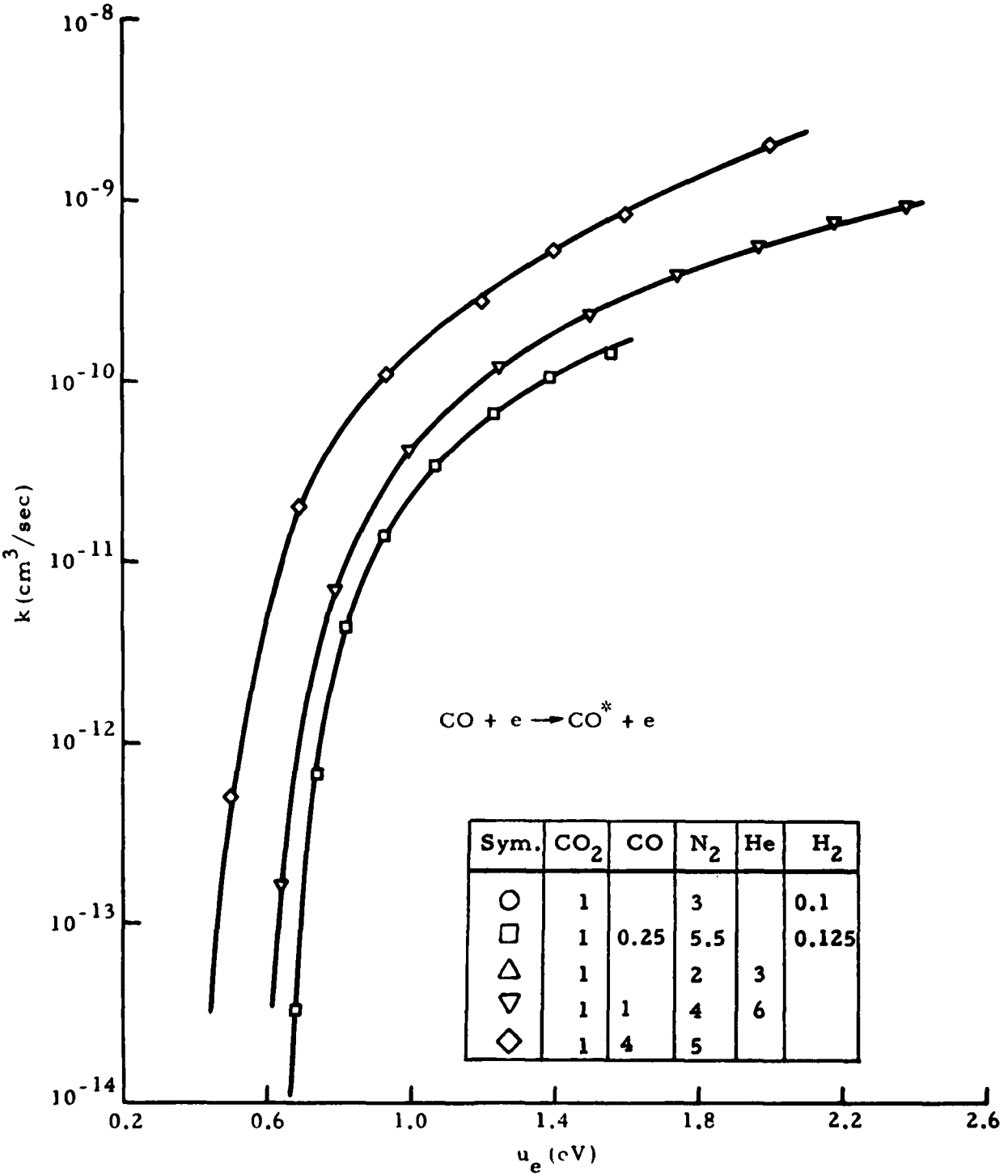

Fig. 17 - Electron Impact Electronic Excitation Rate for CO^*

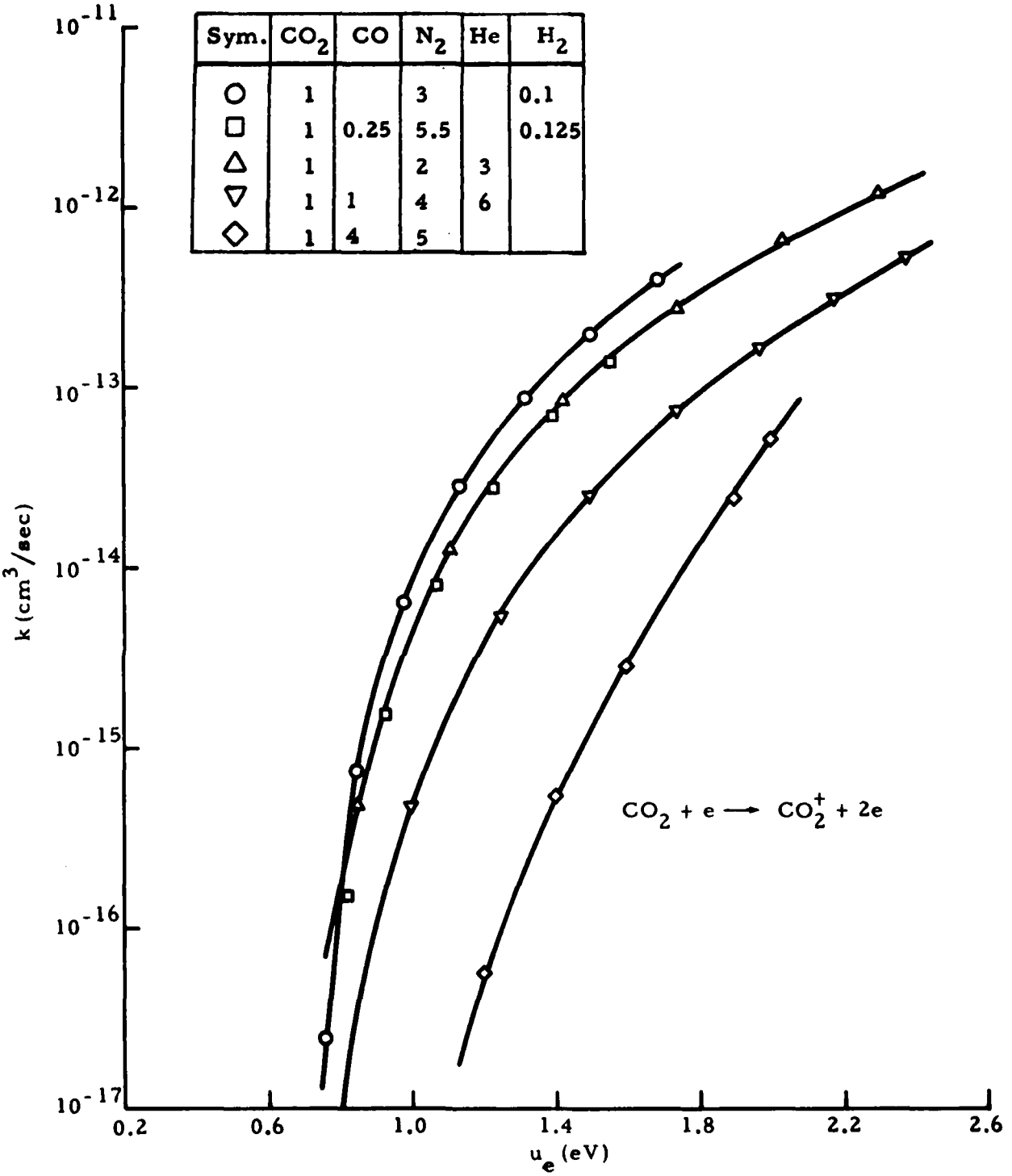

Fig. 18 - Electron Impact Ionization Rate of CO_2 for Various Gas Mixtures

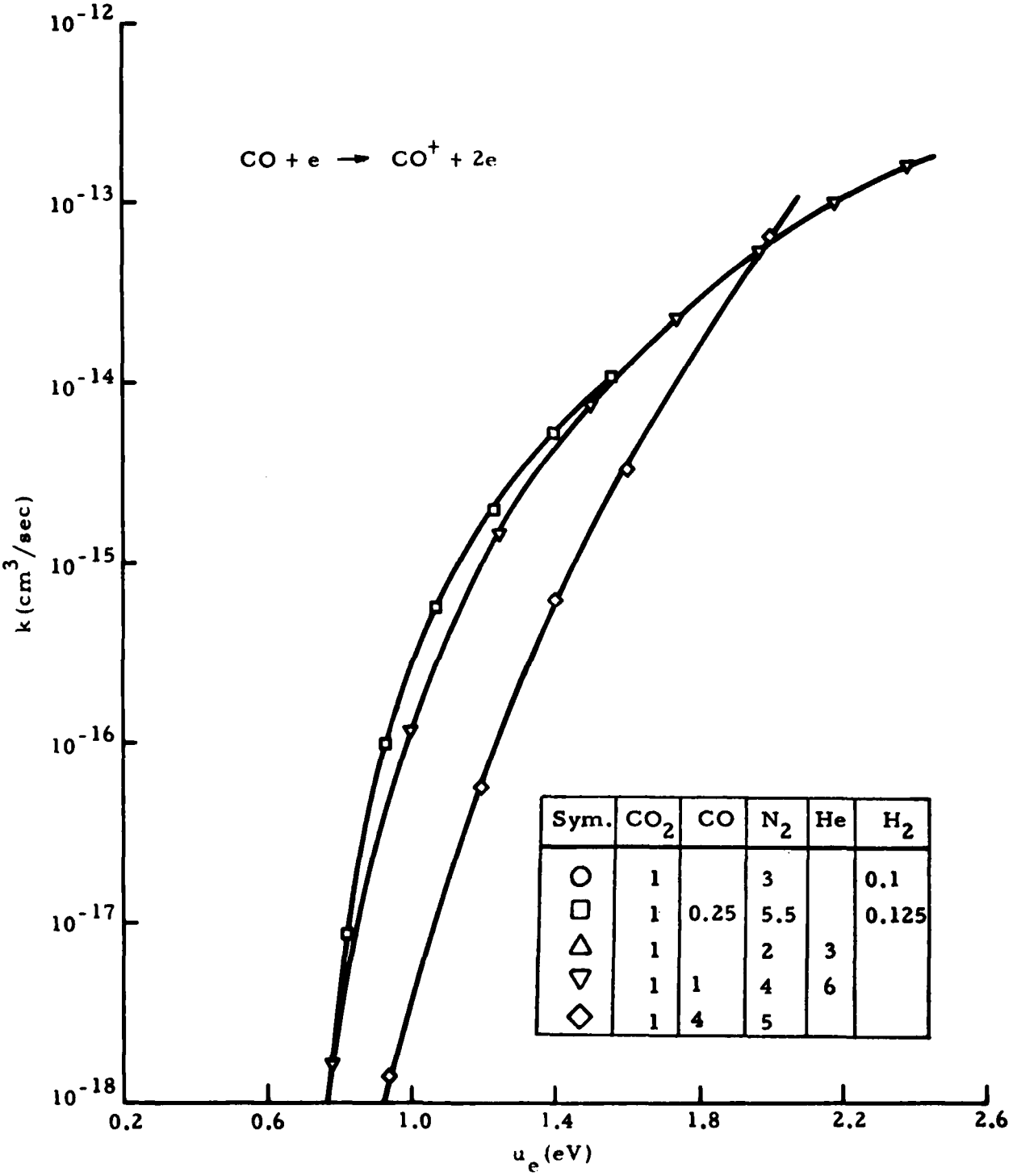

Fig. 19 - Electron Impact Ionization Rate of CO for Various Gas Mixtures

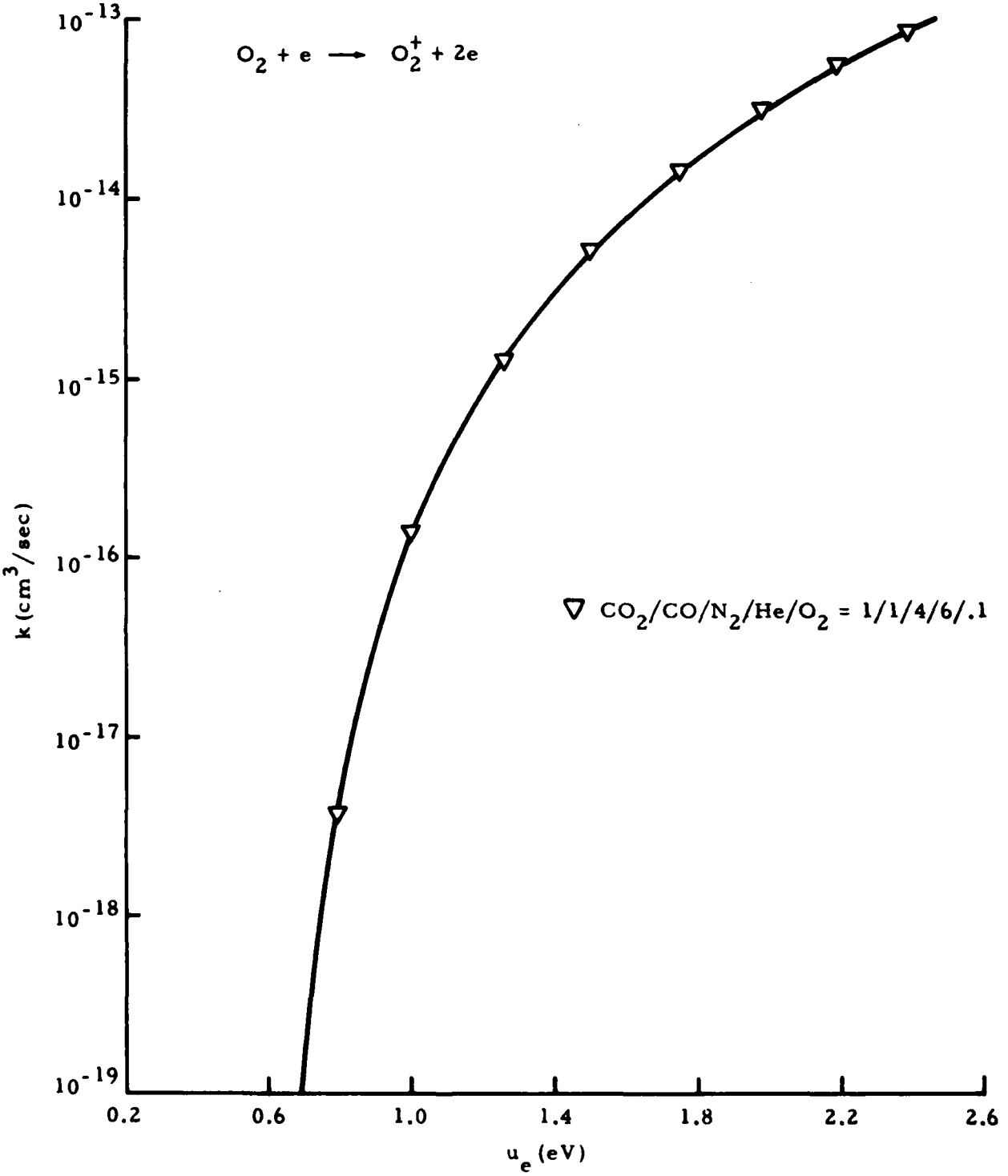

Fig. 20 - Electron Impact Ionization Rate for O_2

independent of the gas mixture. As previously mentioned by Elliott et al. (Ref.12), the average electron energy is such a parameter, at least nearly so. Figures 10 through 12 show that vibrational excitation rates for $CO_2(010)$, $CO_2(100+020)$, and $CO_2(001)$, when plotted as a function of average electron energy, are practically insensitive to mixture variations over a wide range of different mixture compositions. Figure 13 indicates that the $CO_2(030)$ excitation is slightly faster for mixtures with He as compared to those containing H_2. Still, the difference is negligible in view of other uncertainties of the overall plasma chemistry model. The $N_2(1)$ excitation rate shown in Fig.14 shows some scatter only at the very low electron energies. No clear distinction between He and H_2 mixture is discernable here. Figure 15, showing the CO(1) vibrational excitation rate, indicates that the presence of N_2 does have a noticeable effect on this process, the rate being faster for mixtures with N_2 as compared with a mixture without N_2. All in all, with regard to the dominant electron impact vibrational excitation rates of CO_2, N_2 and CO, the use of mixture independent excitation rates as a function of electron energy should be an excellent approximation.

Unfortunately the same cannot be said about the electronic excitation rates for CO_2, N_2 and CO which are shown in Figs.16 and 17. First of all, it should be noticed that these rates are roughly at least an order of magnitude lower than the vibrational excitation rates. For average electron energies below 1.0 eV they may be several orders of magnitude lower. The rate of N_2 excitation appears to be dependent on the presence of He or H_2 while the relative amounts of other gases do not seem to have any noticeable effect. For electronic excitation of CO_2, the rate can vary up to almost an order of magnitude depending on the gas mixture, as seen from Fig. 16. The rate for electronic excitation of CO (Fig. 17) also depends on the gas mixture composition to some degree. Mixtures containing N_2 result in a distinctly lower rate for this process as compared to the mixture without N_2.

From the ionization cross-section data as supplied with the Boltzmann code (Ref. 8) it can be inferred that ionization of He and N_2 does not play any role except at very high electron energies ($u_e \geq 18$ eV). Ionization of CO_2,

CO, and O_2 does occur at rates which are several orders of magnitude lower than those for vibrational and electronic excitation. Ionization rates, unfortunately, are very dependent on the particular gas mixture as shown in Figs. 18 and 19. The oxygen ionization rate in a typical He mixture is shown in Fig. 20.

The discussion of the Boltzmann code results permits the following conclusions. When a new gas mixture is to be analyzed, Boltzmann code calculations have to be made to determine the drift field velocity as a function of E/N. It is very likely that no changes are needed in the electron impact vibrational excitation rates. Rate constants for electronic excitation and ionization will most probably have to be determined for each individual mixture.

There is one additional problem that must be mentioned. In the Boltzmann code, $CO_2(100+020)$ is treated as a compound state resulting in a compound rate constant for impact vibrational excitation of these levels. Since the plasma kinetics calculations consider $CO_2(100)$ and $CO_2(020)$ as separate species, some prescription has to be devised for splitting the compound rate constant. Because of Fermi resonance these two levels are closely coupled; in fact, many CO_2 laser codes explicity assume equilibrium for these levels. Equilibrium calculations* indicate that, in the range of $200\,K \leq T \leq 400\,K$, the population ratio is roughly $CO_2(100)/CO_2(020) = 1/4$. In the absence of more precise information we therefore assume that

$$\begin{aligned} k(CO_2(100)) &= 0.2\, k(CO_2(100+020)) \\ k(CO_2(020)) &= 0.8\, k(CO_2(100+020)) \end{aligned} \tag{31}$$

for use in the plasma chemistry and laser calculations. This argument is supported by comparisons of our analysis with experimental data to be discussed in Section 3.

*$N_{mnp}/N = [\, e^{-m\theta_1/T}\,(n+1)\, e^{-n\theta_2/T}\, e^{-p\theta_3/T}]/Q_{vib}$

2.2.3 General Reaction Mechanisms

Aside from primary ionization reactions and secondary excitation mechanisms described in detail in the preceding subsections, EDL plasma chemistry calculations require a large number of reactions dealing with electron attachment, detachment change transfer, and recombination, electronic de-excitation and vibrational relaxation, and finally, a sizable number of purely chemical reactions. The general reaction set used for this effort is an updated version of a set which was previously documented in detail (Refs. 3 and 13). A listing of the set currently used is provided in the Appendix.

2.3 CLOSED CYCLE SIMULATION

One of the requirements of the present investigation was to further investigate the response of EDL plasmas when subjected to recirculation and repetitive pulsing in a closed cycle system. Several recent investigations, experimental as well as theoretical, have shown that closed cycle electric discharge lasers are subject to the formation of contaminants which, in all cases, tend to degrade laser performance. For example, electron-beam interaction with materials may cause signigicant amounts of attaching contaminants to be released. We assumed ideal non-reacting walls to explore the effects of discharge produced plasma by-products. Discharge-induced contaminant formation is a time dependent process which greatly depends on initial gas composition, pressure level, discharge energy and pulse width, making it extremely difficult to draw any conclusions of general validity.

Kinetics calculations are dependent on density, temperature and gas composition. To predict the formation of contaminants it is therefore necessary to simulate the varying conditions that the gas experiences as it traverses the closed cycle system. This includes the consideration of catalytic devices designed to remove the most important electrophilic reaction products, thereby eliminating the problem of performance degradation. Of equal importance is the consideration of the effect of heat exchangers designed to return the recirculating gas mixture to the initial temperature after each cycle. Condensation effects, however, are not considered.

It is here assumed that the complete cycle can be simulated in terms of three major events, as shown in Fig. 21. The first leg of the triangular cycle in the p-V diagram represents the discharge itself. The discharge is followed by an adiabatic expansion. It is assumed that after the expansion the gas is again at the initial pressure. The temperature at that point is generally considerably higher than the pre-pulse temperature, and even higher than the post-pulse temperature due to collisional relaxation of the energy stored in the vibrational levels during the discharge pulse. While the time frame for the discharge is given by the discharge pulse duration, the duration of the adiabatic expansion is estimated by calculating the time interval which it would take for a pressure pulse to clear the particular cavity being considered. The final leg of the triangular cycle simulates the return of the mixture to the initial conditions (pressure and temperature). This leg represents a relaxation calculation at constant pressure and specified distribution of temperature versus time. Typically, the time frame for this leg represents the major portion of the gas transit time through one complete cycle. The result of the relaxation calculations through this triangular path is that the gas is now at the initial (pre-pulse) pressure and temperature, but has a composition which is generally different from that at the beginning of the cycle.

Removal of contaminants via catalyst action is currently considered at this point. The effect of a drying bed included to remove water vapor being generated in certain gas mixtures can be modeled in the same fashion. Knowing the gas composition at the end of the cycle, the effect of the catalytic reactor and/or drying bed is computed by adjusting all concentrations according to

$$F_i' = (1 - \eta_i) F_i \qquad (32)$$

where η_i represents the catalyst/drying bed removal efficiency for the ith species, and F_i its mole/mass ratio upstream of the catalyst/drying bed. The cycle is then repeated starting with the adjusted composition F_i' at the initial temperature and pressure.

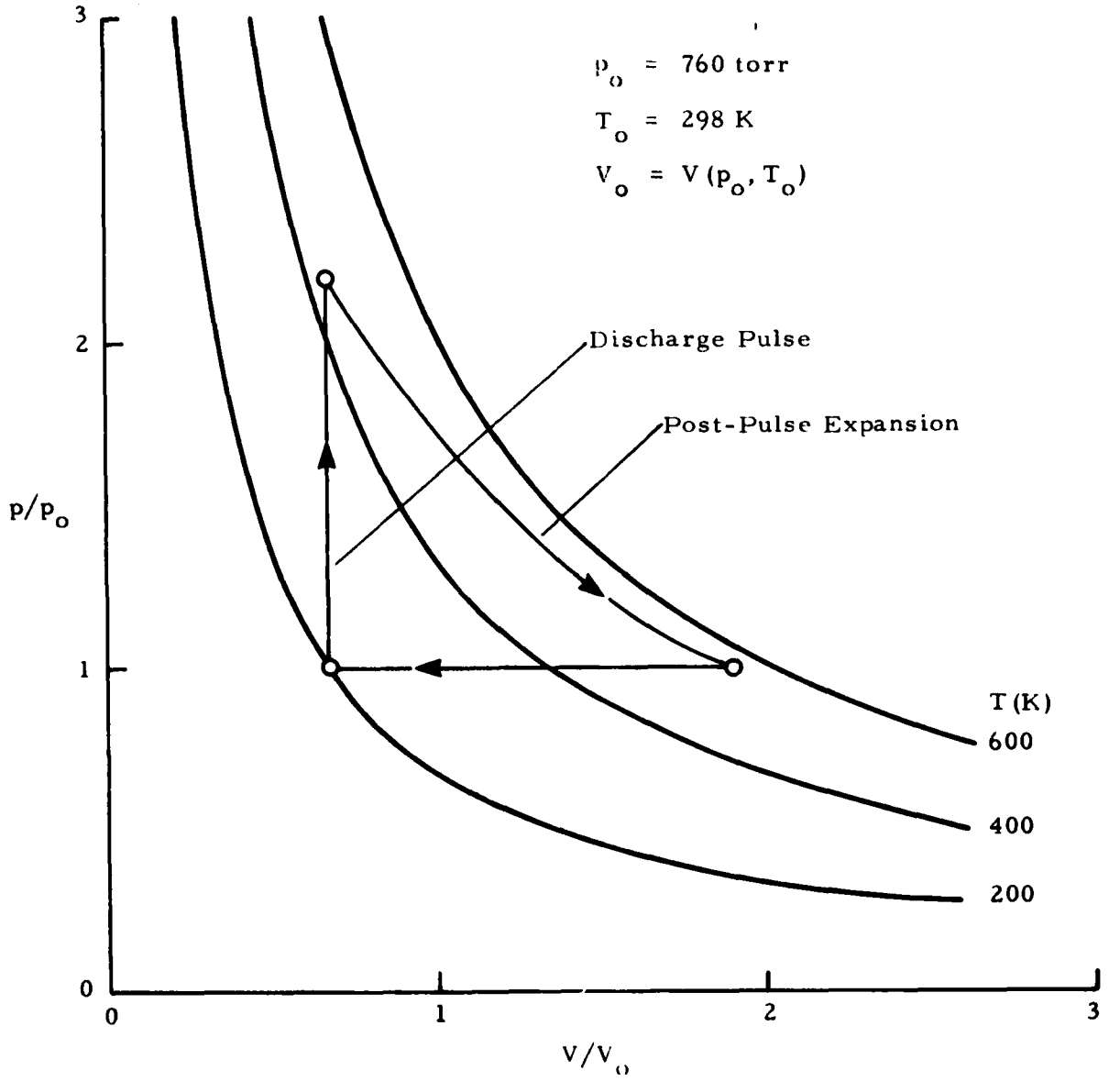

Fig. 21 - Closed Cycle Simulation – Typical Cycle

3. CODE VALIDATION

3.1 INTRODUCTION

It is obviously very important to gain some confidence in the validity of the analysis described in Section 2. Comparison of the analytical model with experimental data will give a direct assessment of the model as a predictive tool for designing closed cycle EDL systems for optimum performance. Although earlier versions of the analytical model (Ref. 14) have shown good overall agreement with experimental data (small signal gain, discharge power loading, laser efficiency), numerous changes and refinements that have been incorporated into the model in the course of the present effort make it necessary that further comparisons between theory and experiment be made. While the present effort was originally undertaken with the goal of defining optimum operating conditions for two closed cycle EDL systems presently under development, delays in the completion of these devices have made it impossible to obtain any experimental data from these devices.

Fortunately some other data have been made available to us. The first case to be discussed in this section concerns a small scale closed system operated at the MIT Lincoln Laboratories with the purpose of investigating the effects of discharge generated contamination on performance as a function of time (Ref. 15).

The second case concerns a large open cycle device (ABEL). Even though discharge generated contamination is of lesser importance in an open cycle device, it afforded us the opportunity to compare model results with projected performance data (Ref. 16).

3.2 SMALL SCALE E-BEAM DEVICE

Reportedly, the closed system small scale E-beam device tested at the Lincoln Laboratories was designed with the aim to minimize contamination of the laser gas from the device hardware (outgassing, etc.). The nominal operating conditions are summarized in Table 2, and Fig. 22 shows a cross section of the hardware used. Experimental results were provided in the form of oscilloscope traces for the sustainer current and the small signal gain of the P(20) transition. As no heat exchanger was used, heat conduction

Table 2

CLOSED SYSTEM, SMALL SCALE E-BEAM DEVICE DATA
(Lincoln Laboratory, Ref. 15)

Gas Composition	$CO_2/CO/N_2/He/O_2$ = 1/1/4/6/0.1
P (Initial)	605 torr
T (Initial)	298 K
E-Beam Current	1.6 mA (Effective)
E-Beam Energy	165 keV (Nominal
Sustainer Voltage	8.1 kV
Electrode Gap	3 cm
Cross Section	See Fig. 22
Gain Length	15 cm
Pulse Duration	300 μsec
Pulse Frequency	1 Hz
Post-Pulse Expansion	300 μsec
Cycle Time	1.0 sec

to the water-cooled cavity walls was relied upon to reduce the post-pulse temperature to room temperature between pulses. Simplified heat conduction calculations indicated that this method should indeed suffice.

In any attempt to model an experiment which is not tailored to the analysis certain assumptions will have to be made before actual calculations can be

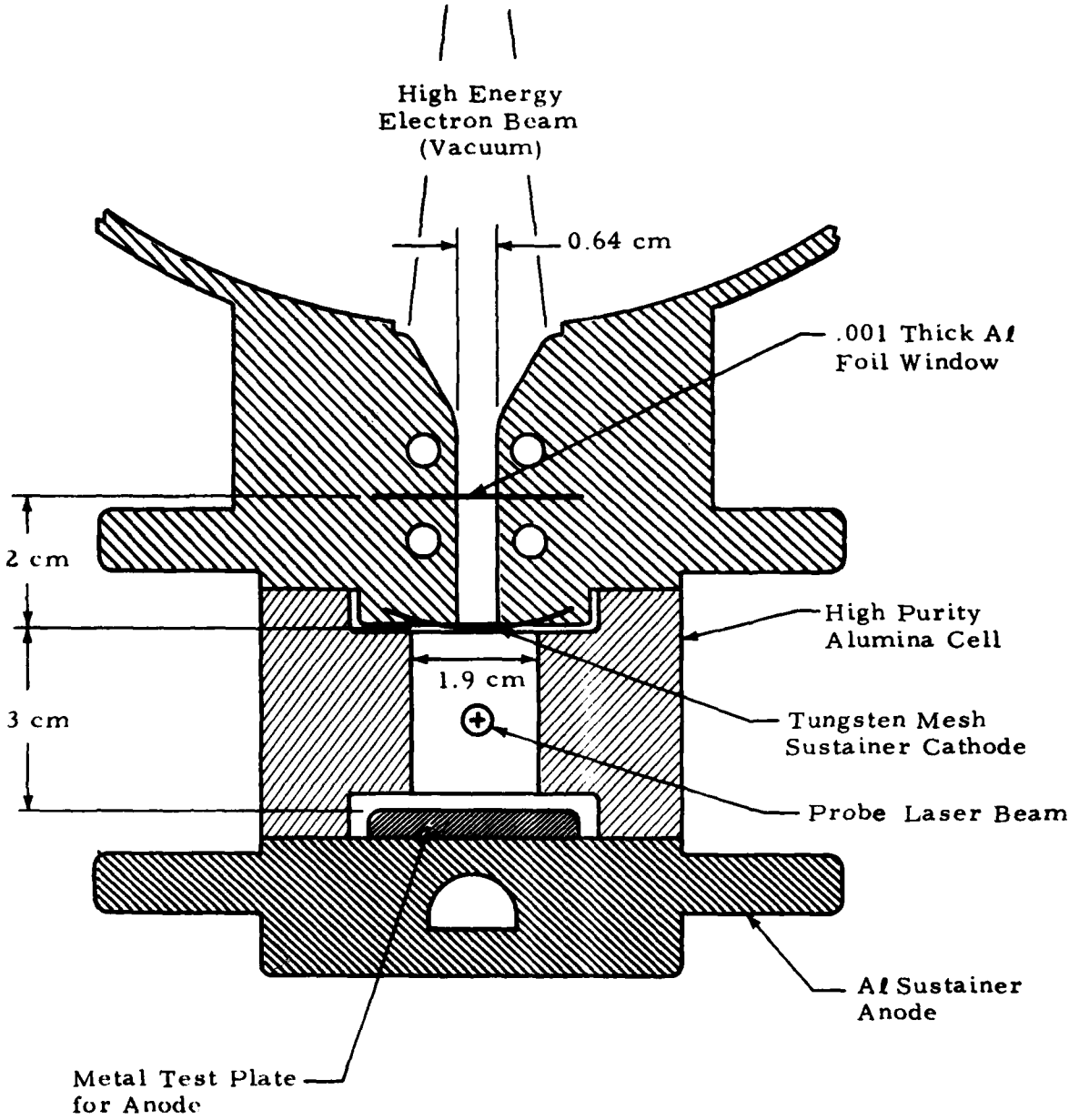

Fig. 22 - Small Scale E-Beam Device

performed. For example, examination of the cavity cross section (Fig. 22) shows that discharge conditions in the cavity are not likely to be spatially uniform as assumed by the theoretical model. In this case we have chosen to model the center section of the cavity, i.e., a region which has the same width as the foil window, and which includes the location of the probe laser beam. This is equivalent to assuming a collimated electron beam, or neglecting electron beam spreading in the cavity due to whatever reason.

A quantity that requires further examination is the electron beam energy. Beam electrons experience losses due to interaction with the foil and due to collisions in the cavity. Some of these losses are compensated for by acceleration in the electric field of the discharge. Using the data by Berger and Seltzer (Ref. 7) the energy loss in the foil under the given conditions is estimated to be about 17 keV. The average collisional loss in the cavity amounts to another 2 keV, while the discharge will provide an average gain of about 4 keV. This results in a net loss of about 15 keV, and therefore yields an effective electron beam energy of 165 - 15 = 150 keV.

Finally, in order to perform the plasma chemistry calculations, the electron impact excitation rates have to be established using the Boltzmann code. These calculations and their results have already been discussed in Section 2.

All in all, only relatively minor corrections were needed in the model to arrive at the comparison between experimental and theoretical results shown in Figs. 23 and 24. The major problem encountered was the uncertainty in the dominant rate of electron attachment to O_2. While this rate was unimportant in previously computed cases, it turned out to be of great importance in this particular gas mixture (see Table 2). Reducing the magnitude of the rate constant by a factor of two (which was well within the range of uncertainty) and giving it an inverse temperature dependence (as suggested by theoretical considerations) the temporal distributions of small signal gain and sustainer current as calculated are in satisfactory agreement with the experimental data as shown in Figs. 23 and 24, respectively. The reason for the discrepancy in the

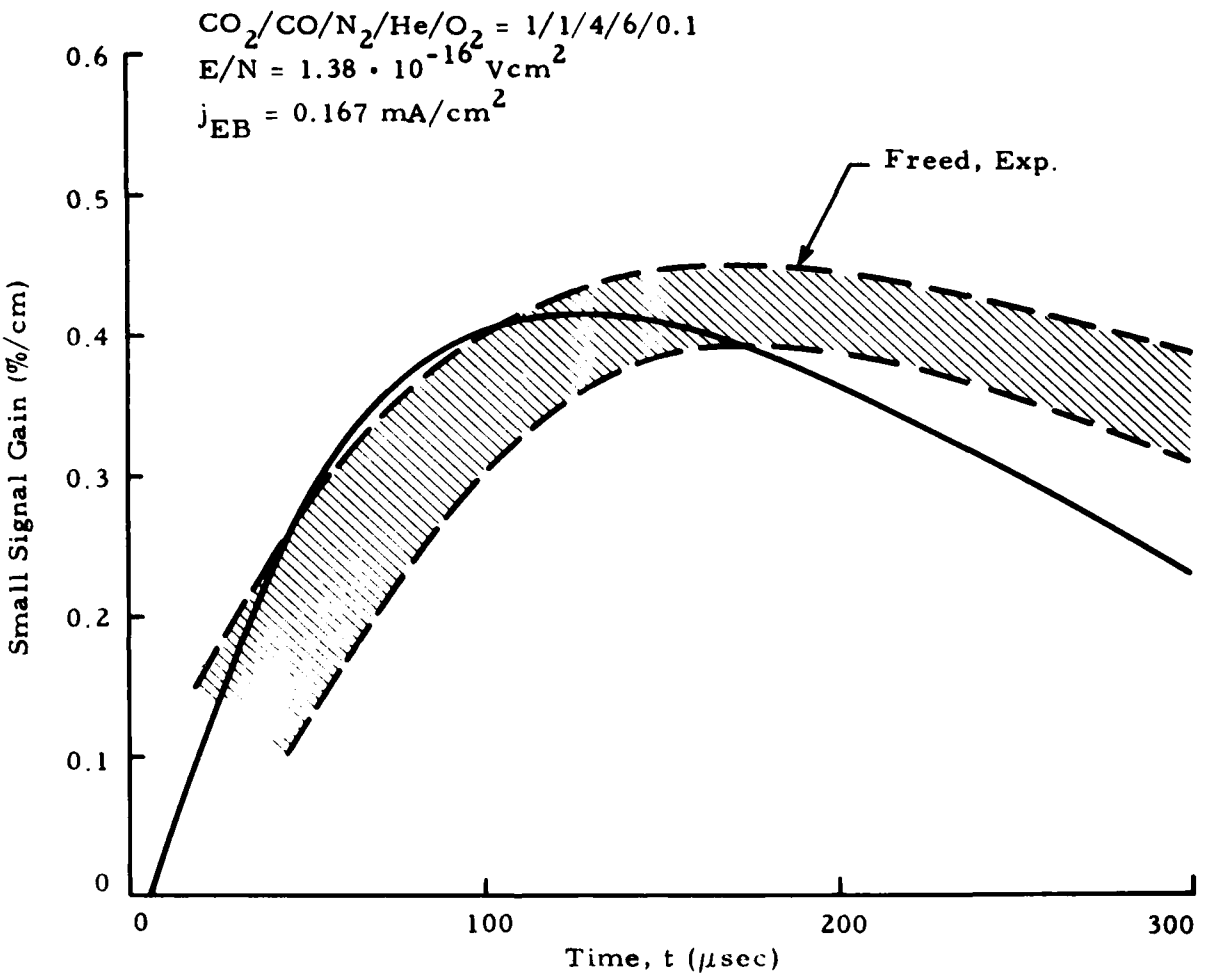

Fig. 23 - Calculated Temporal Distribution of Small Signal Gain (P20, 5th Pulse)

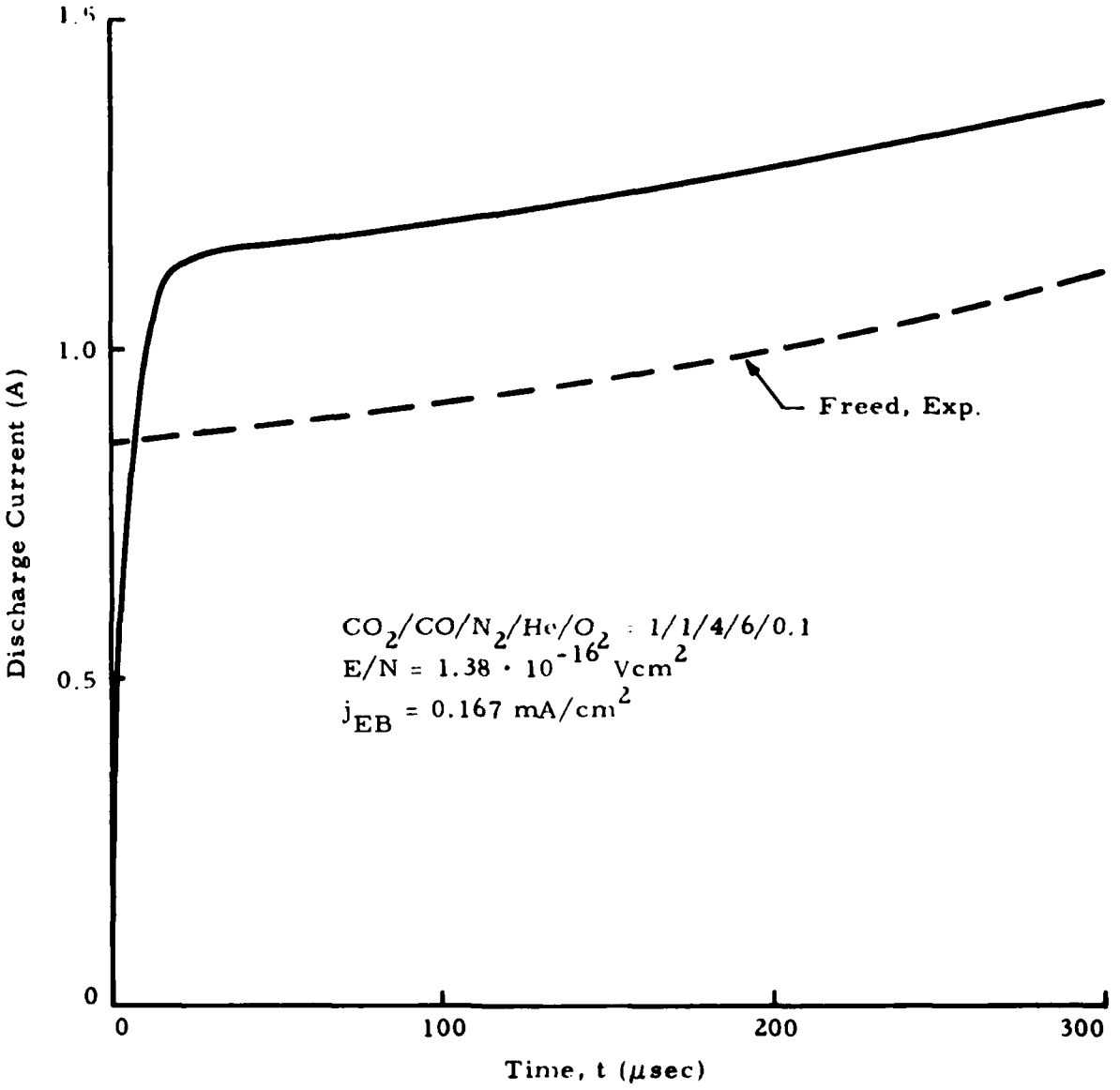

Fig. 24 - Calculated Temporal Distribution of Discharge Current (5th Pulse)

tail of the gain distribution is not known at this time. Calculations with slightly increased electron beam current have shown that this could be remedied but only at the expense of a higher peak gain and a lesser agreement between theoretical and measured discharge current distribution.

As mentioned above, the purpose of this experiment was to investigate discharge generated contamination and its effect on discharge power loading. The analysis predicts the major by-products to be various nitrogen oxides as shown in Fig. 25. For the dry gas mixture the effect of these nitrogen oxides on the discharge energy loading is minimal as can be inferred from Fig. 26.

Computer run time for the dry gas case with ten cycles was roughly 6 minutes on the CDC Cyber 176. This shows clearly that it would be prohibitive to continue these calculations for something like 2000 cycles. It is therefore of interest to develop an estimate of the performance decay rate as a function of time, and to compare the results with experimental observations. As will be seen, it is then also of importance to know that the "gas utilization factor" in this experiment was about 1/15 (plasma volume to total system gas volume). Assuming an exponential decay for the discharge power loading of the form

$$E_{in} = A \cdot e^{-an} \tag{33}$$

where n denotes the number of cycles (or pulses in this case), the time constant or decay rate, a can be determined from the results shown in Fig. 26. This yields a value of $a = 1.31 \cdot 10^{-3}$. Considering the gas utilization factor of $g = 1/15$, the actual decay rate would be approximately $a \cdot g = 8.7 \cdot 10^{-5}$. With this value, we find from Eq. (33) for $n = 2000$

$$\frac{E_{in}}{A} = e^{-a \cdot g \cdot 2000} = 0.84 \tag{34}$$

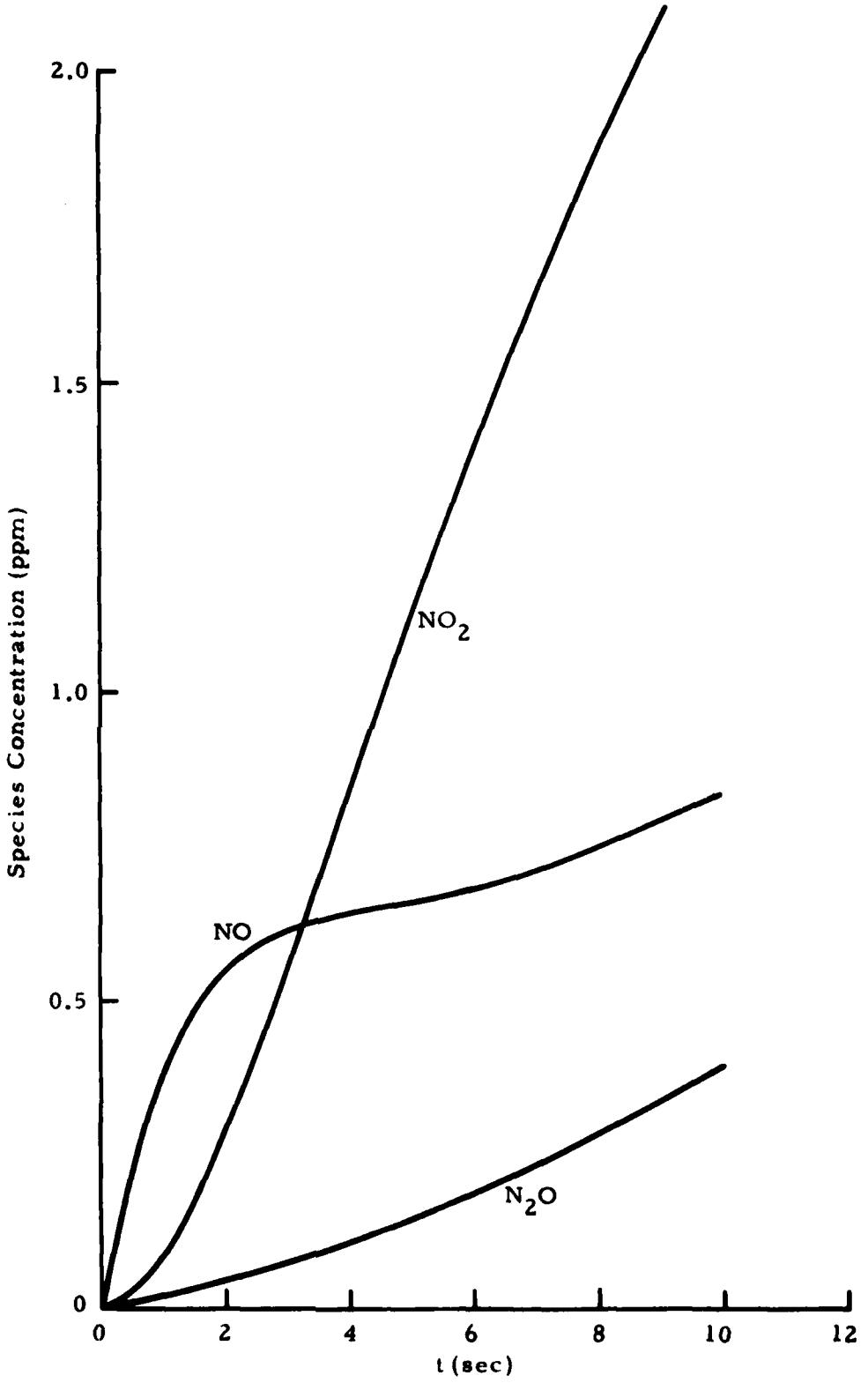

Fig. 25 - NO_x Contaminant Formation in Dry Gas
($CO_2/CO/N_2/H_e/O_2$ = 1/1/4/6/0.1)

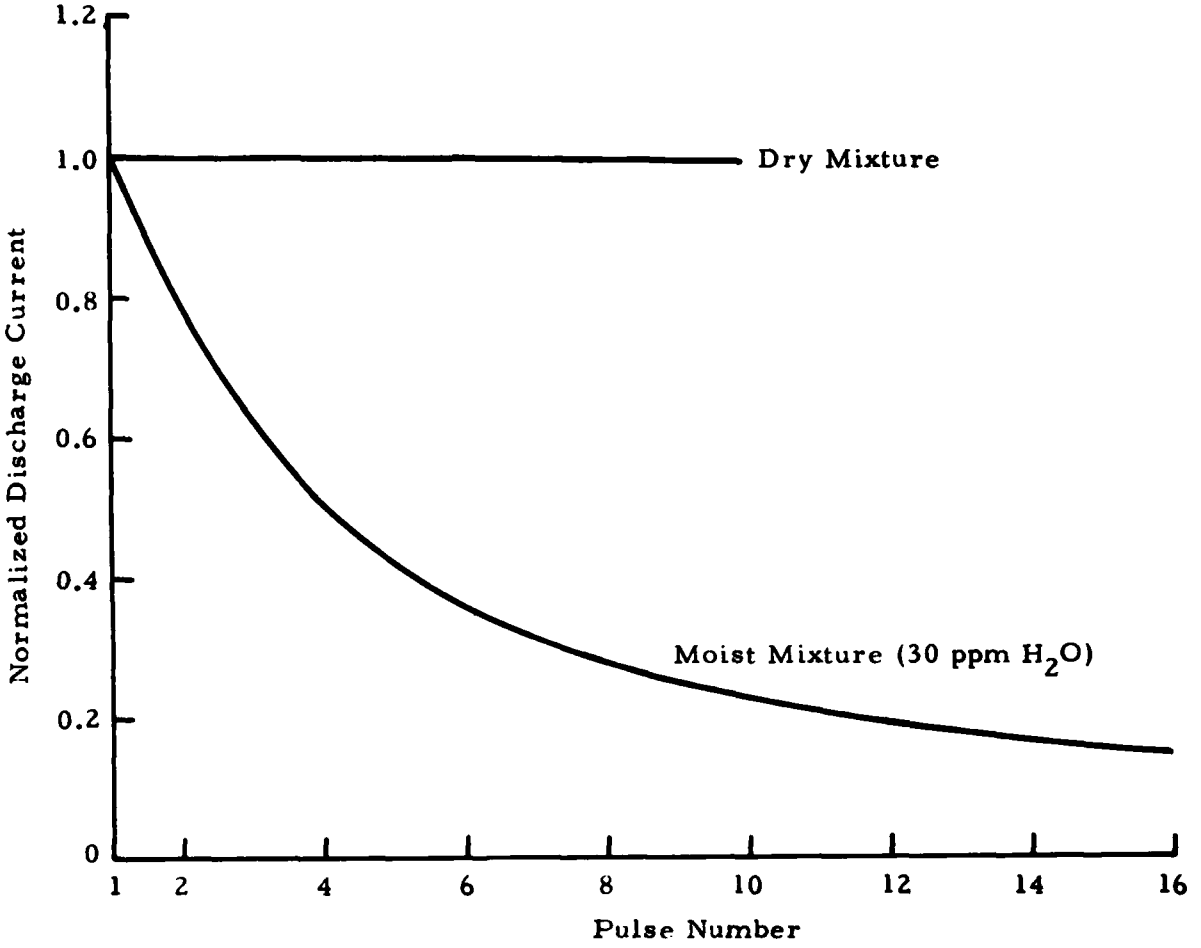

Fig. 26 - Normalized Discharge Power Loading as a Function of Pulse Number ($CO_2/CO/N_2/He/O_2$ = 1/1/4/6/0.1)

which indicates an overall decay of 16% after 2000 pulses. This is in excellent agreement with the experiment which showed a decay of 10 to 20% in the gain after 2000 pulses (Ref. 15).

Performance deteriorates drastically when water vapor is added to the mixture. The effect of 30 ppm H_2O on the discharge energy loading is also shown in Fig. 26. The simultaneous presence of H_2O (or H_2) and certain nitrogen oxides (see Fig. 27) generally leads to the formation of HNO_2, NHO_3 and HO_2NO_2 (see Fig. 28) all of which have large cross sections for electron attachment. Although the HNO_x concentrations shown in Fig. 28 are of the same magnitude as the NO_x concentrations shown in Fig. 27, electron attachment cross sections for the HNO_x are several orders of magnitude larger than those for NO_x, thereby accounting for the decay in discharge current and small signal gain (Fig. 29) when moisture is present in the discharge gas mixture.

3.3 LARGE OPEN CYCLE DEVICE (ABEL)

ABEL is a cold flow, open cycle, pulsed electron beam sustained electric discharge laser. Its principal purpose is to develop and prove high pulse rate, high power electric discharge laser technology. A schematic of the cavity configuration is shown in Fig. 30. Cavity characteristics and typical operating conditions as well as projected performance data are listed in Table 3. As usual, the flow direction, the direction of the electric field and the optical axis are mutually perpendicular.

Electron impact excitation rates for this case were discussed in Section 2. The only additional assumption used in the calculations for this device concerns the electric field distribution which is assumed to have a linear rise from one tenth of nominal value to full nominal value over the first two microseconds of the discharge pulse.

Some illustrative results are presented in Figs. 31 through 33, showing the small signal gain for the P(18) transition, temperature distributions with and without lasing, and the secondary electron density, respectively.

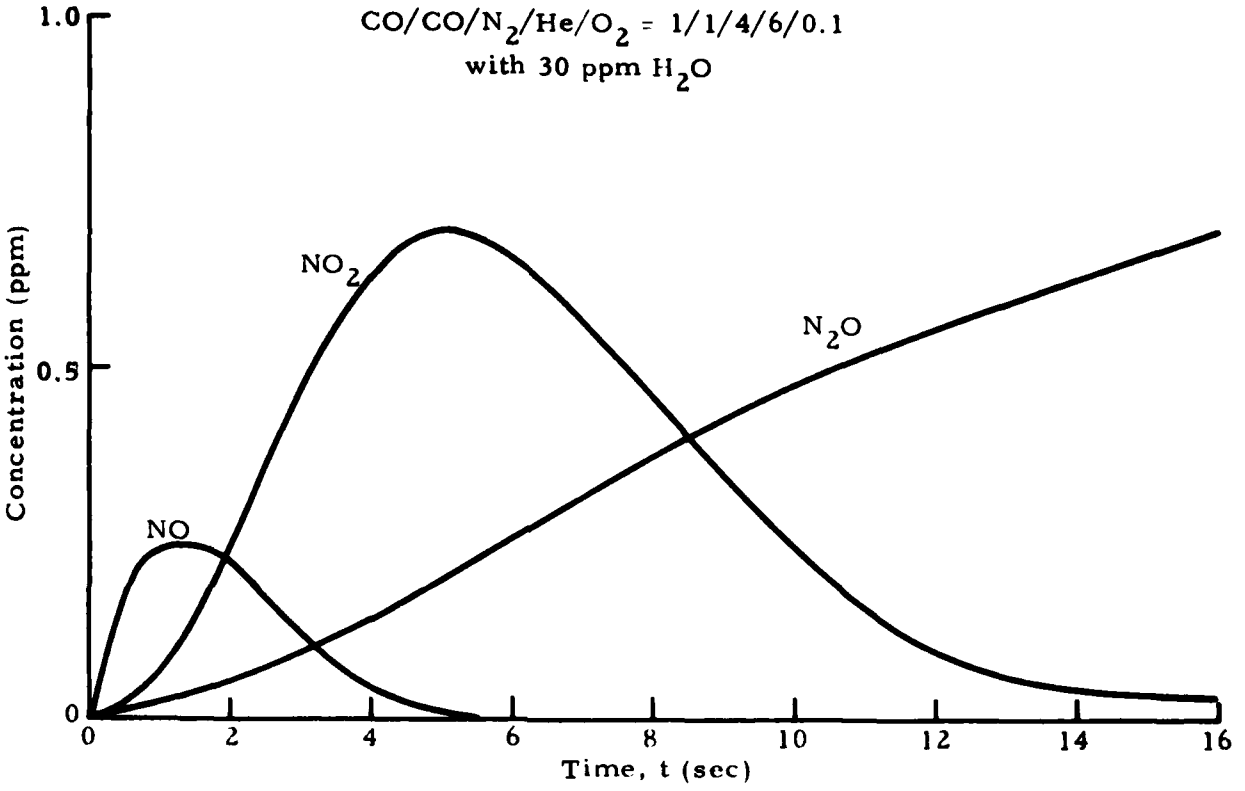

Fig. 27 - NO_x Formation with 30 ppm H_2O (NO_3 is negligible) Concentration Shown at End of Cycle

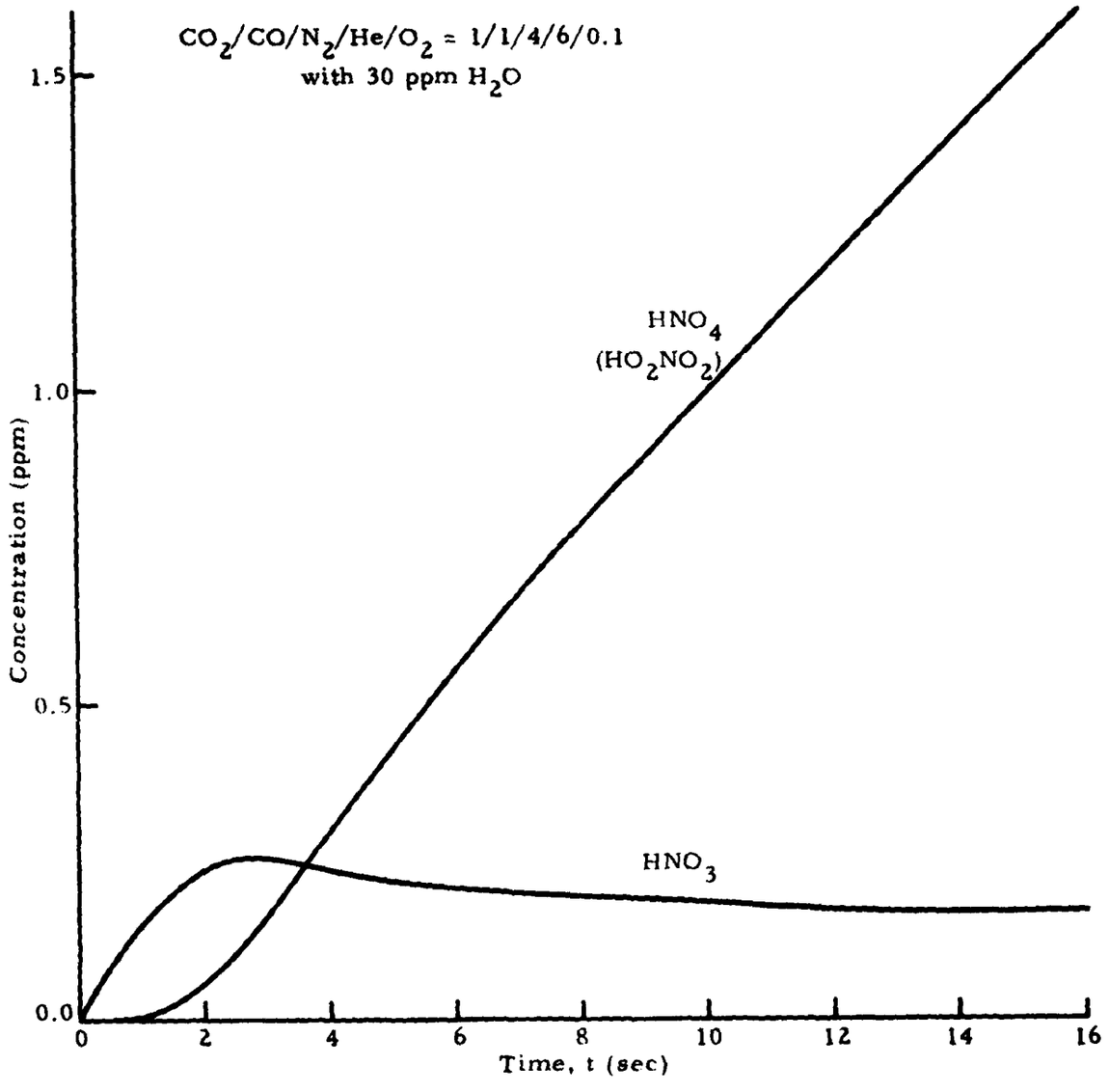

Fig. 28 - HNO_x Formation with 30 ppm H_2O – HNO_2 is Negligible
(Concentrations as shown at end of cycle.)

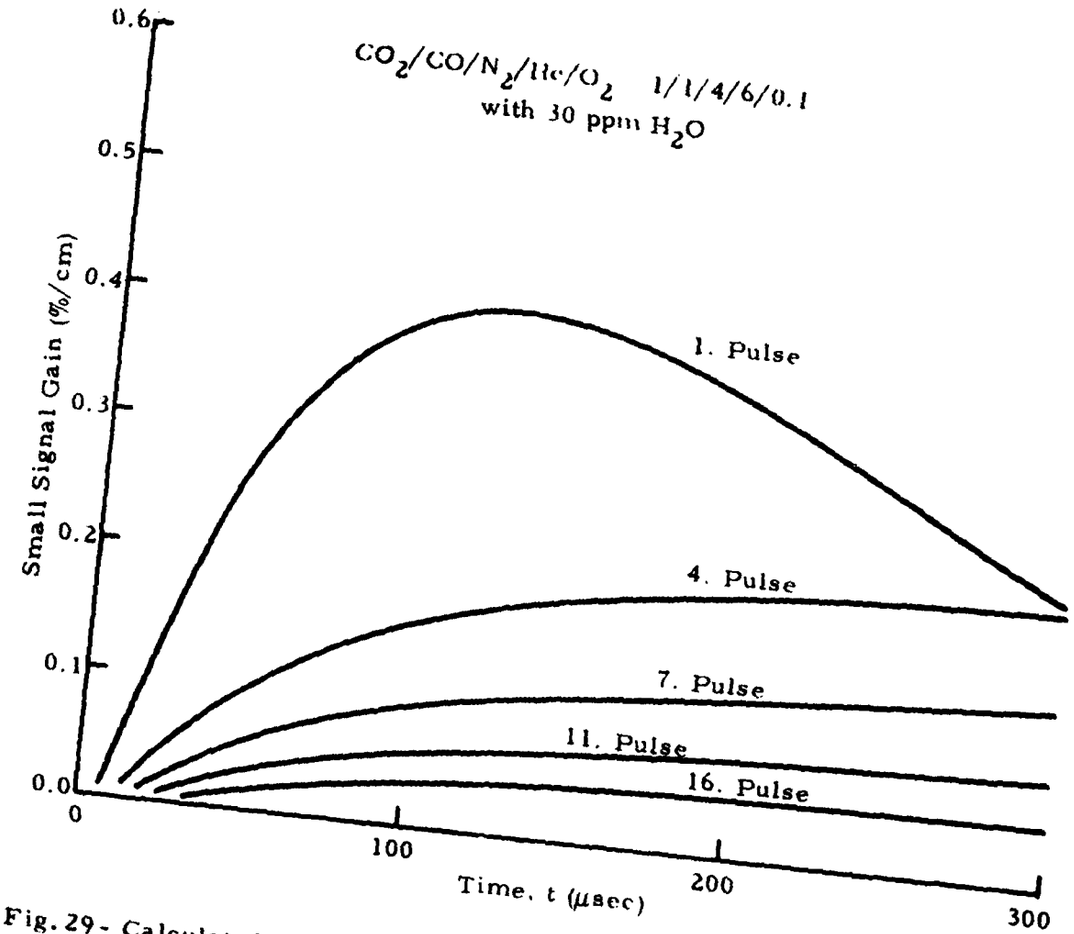

Fig. 29 - Calculated Temporal Distribution of Small Signal Gain for Moist Gas ($CO_2/CO/N_2/He/O_2$ - 1/1/4/6/0.1 with 30 ppm H_2), (1 pulse/sec)

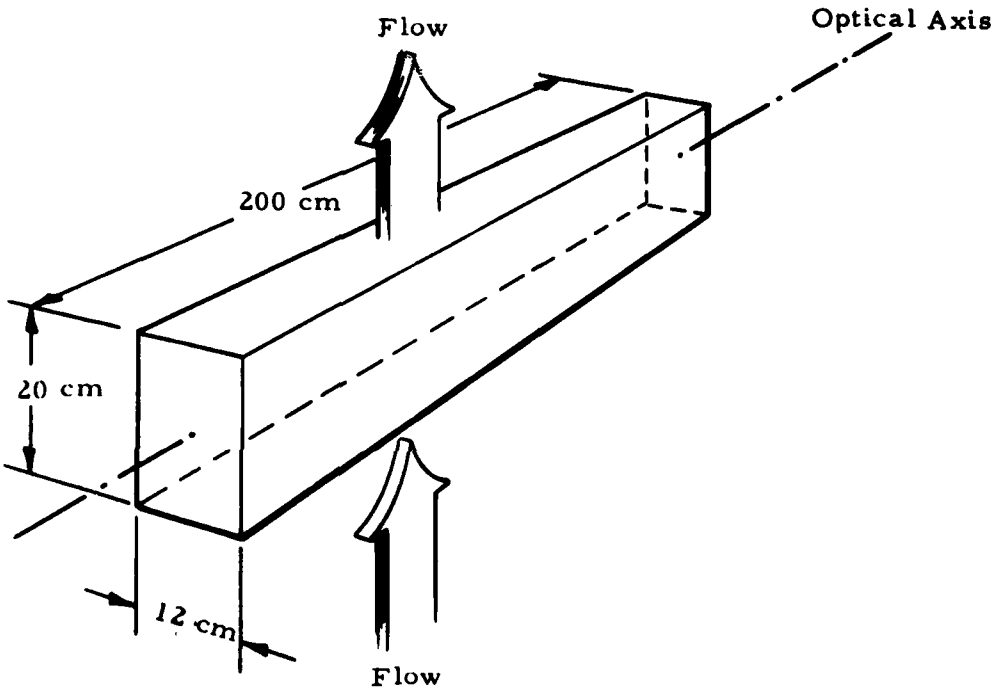

Fig. 30 - ABEL Cavity Configuration (Schematic)

Table 3

SAMPLE DEVICE CHARACTERISTICS (ABEL)

Gas Composition	$CO_2/N_2/H_2$ = 1/3/0.1
P (Initial)	1.0 atm
T (Initial)	200 K
E-Beam Current (Nominal)	107 A
(Effective)	60 A
E-Beam Energy (Effective)	225 keV
Discharge Voltage	162 kV
Cathode Fall	500 V
Electrode Separation	12 cm
Electrode Area	20 x 200 cm^2
Discharge Volume	48 lit
Gain Length	200 cm
Output Coupling	0.86
E-Beam Pulse Width	$0 \leq t \leq 24$ μsec
Discharge Pulse Width	$2 \leq t \leq 22$ μsec

Projected Performance	
Energy into Gas	0.75 - 0.85 kJ/lit
Output	0.13 - 0.20 kJ/lit

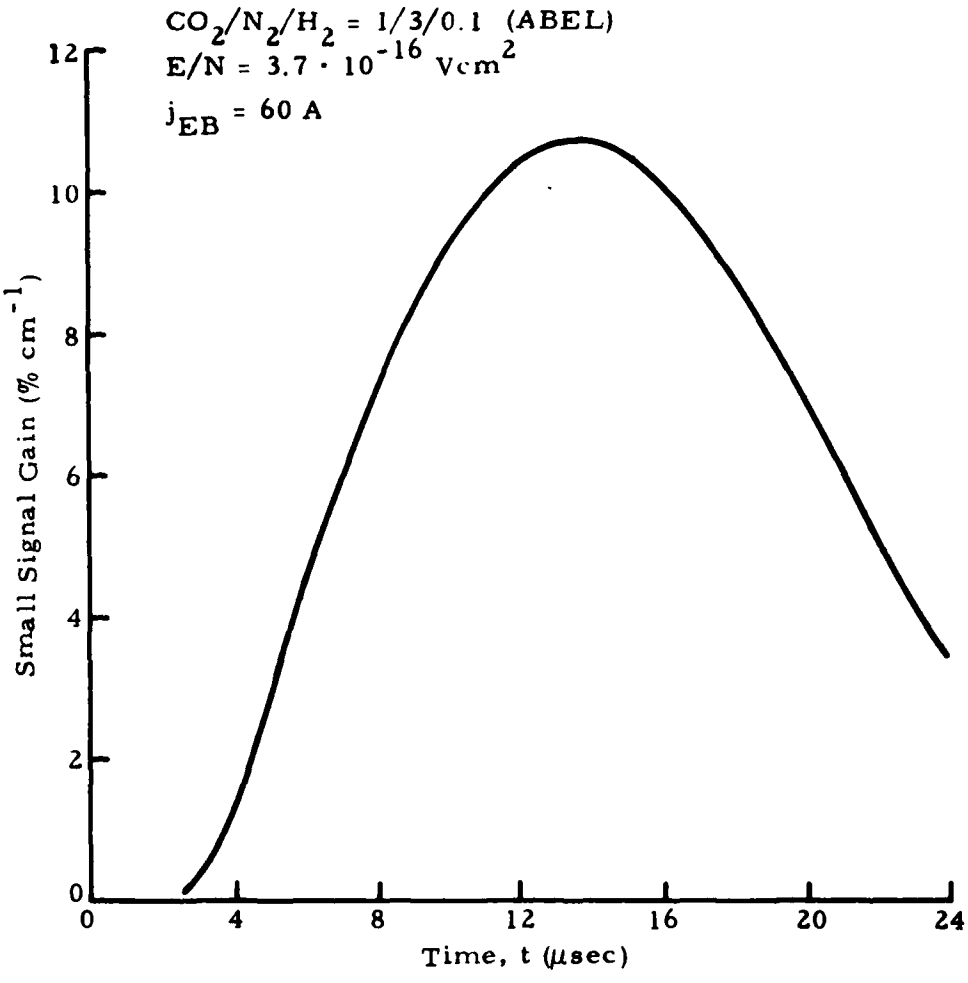

Fig. 31 - P(18) Small Signal Gain Temporal Distribution

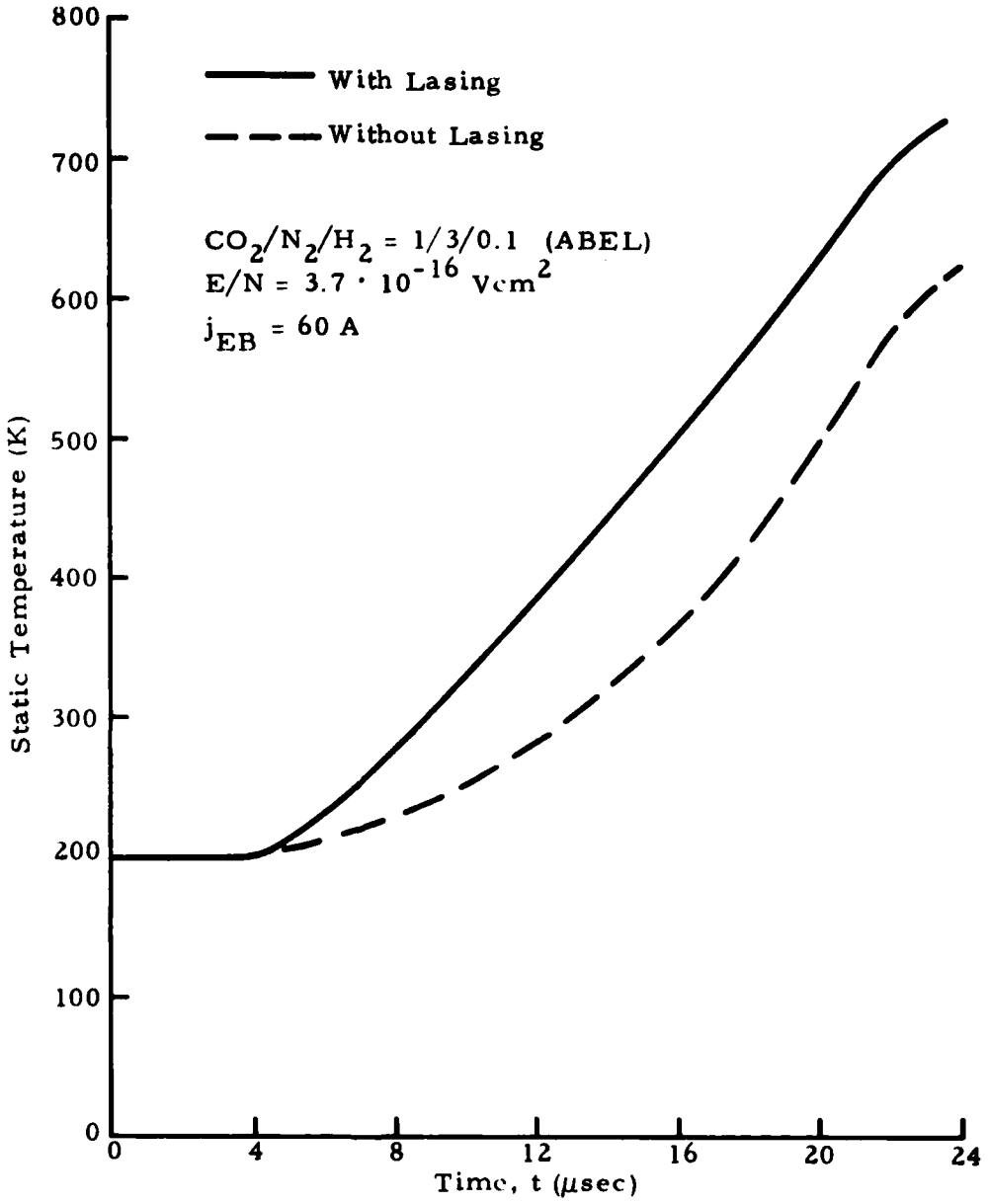

Fig. 32 - Translational Temperature Temporal Distribution

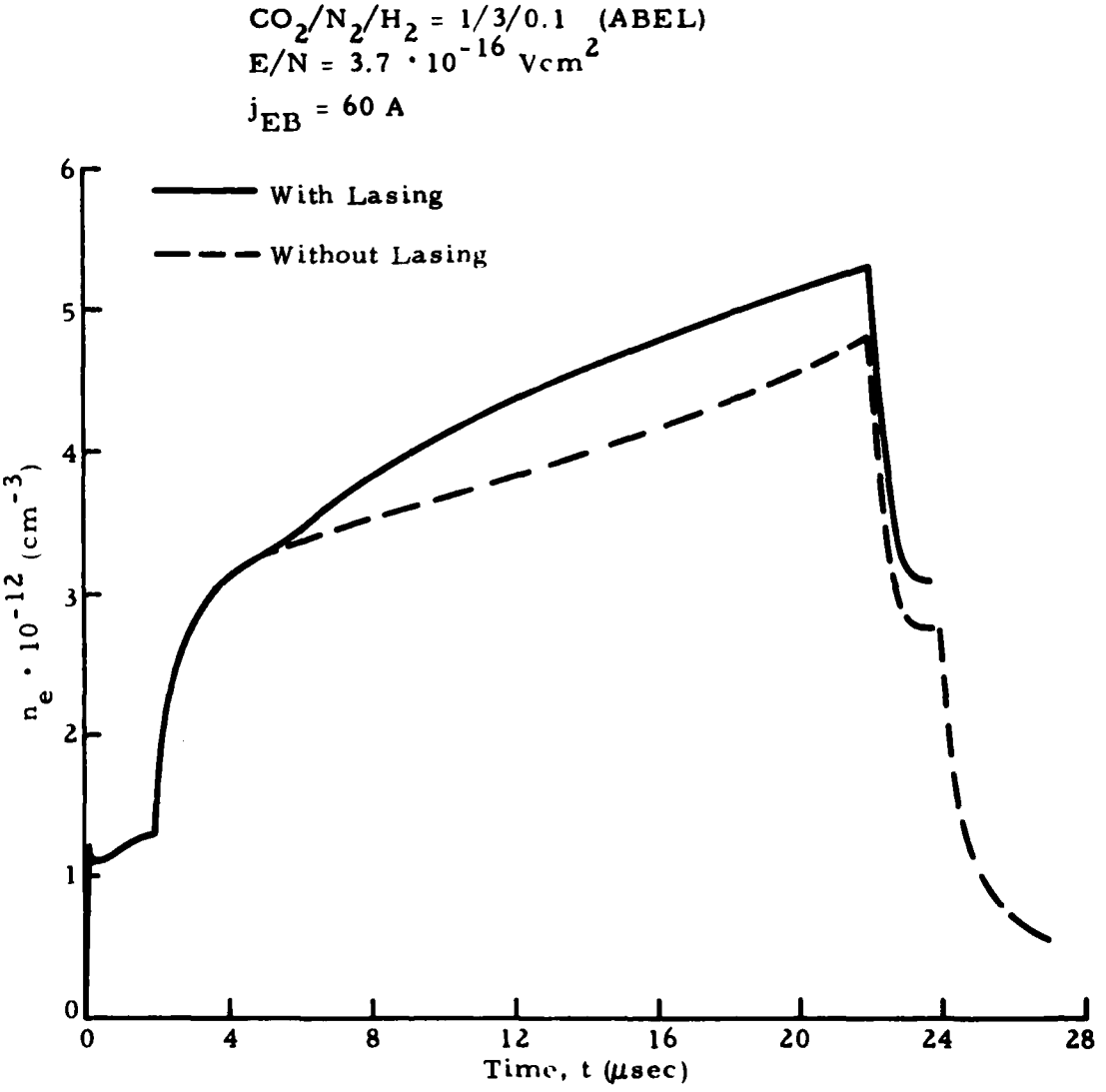

Fig. 33 - Secondary Electron Density Temporal Distribution

The most important predictions are, however, those of output flux intensity and discharge power loading and their temporal distribution during pulsed laser operation. The P(18) output flux distribution shown in Fig. 34 represents an output power of 0.15 kJ/lit. The corresponding discharge power loading distribution shown in Fig. 35 represents a discharge energy input of 1.09 kJ/lit with lasing, and 0.98 kJ/lit without lasing. The resulting efficiency therefore is about 14%. While the output power is in excellent agreement with the projected performance, the discharge power loading appears to be about 20 to 25% high, resulting in an efficiency which is probably on the low side. The dependence of all three quantities on the effective electron beam current is shown in Fig. 36. It can be seen that at a current of 40 Amp the discharge power loading becomes about 0.85 kJ/lit and the output pulse energy decreases slightly to about 0.14 kJ/lit with a resulting efficiency of 16%. Therefore, making allowance for the uncertainty in the given effective electron beam current it appears that the present analysis is in excellent agreement with the projected performance of the device under study.

Finally, it should be remembered that these calculations were performed for given pulse durations (see Table 3). It is clear from Fig. 34 that the pulse stretches as the electron beam current (and the secondary electron density as a consequence) is decreased. Figure 34 shows that for E-beam currents of less than 100A the output pulse is terminated by the E-beam cutoff. Conclusions drawn from Fig. 36 must keep this in mind. In future calculations the pulse duration should be considered a variable to be determined as a result of the analysis rather than specified a priori.

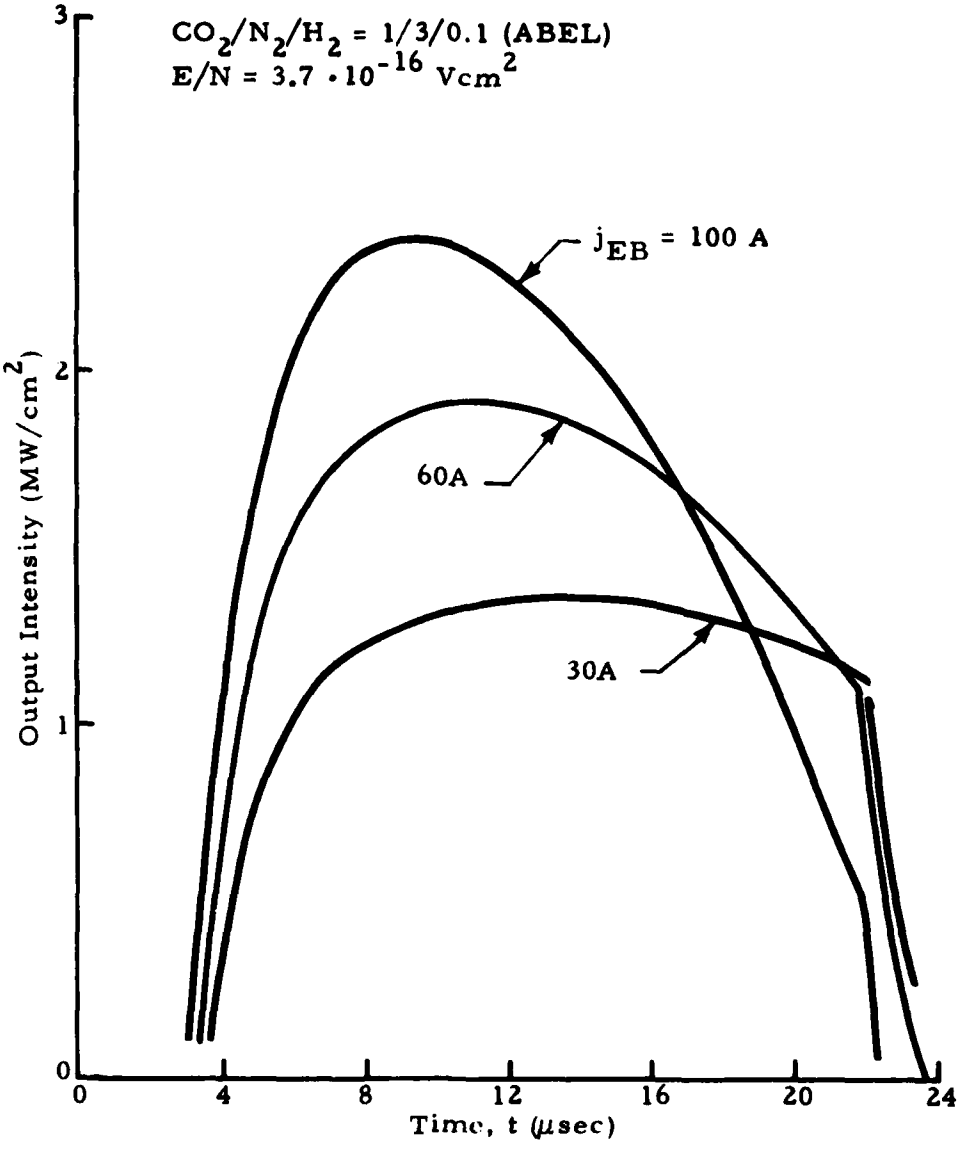

Fig. 34 - P(18) Output Intensity Temporal Distribution

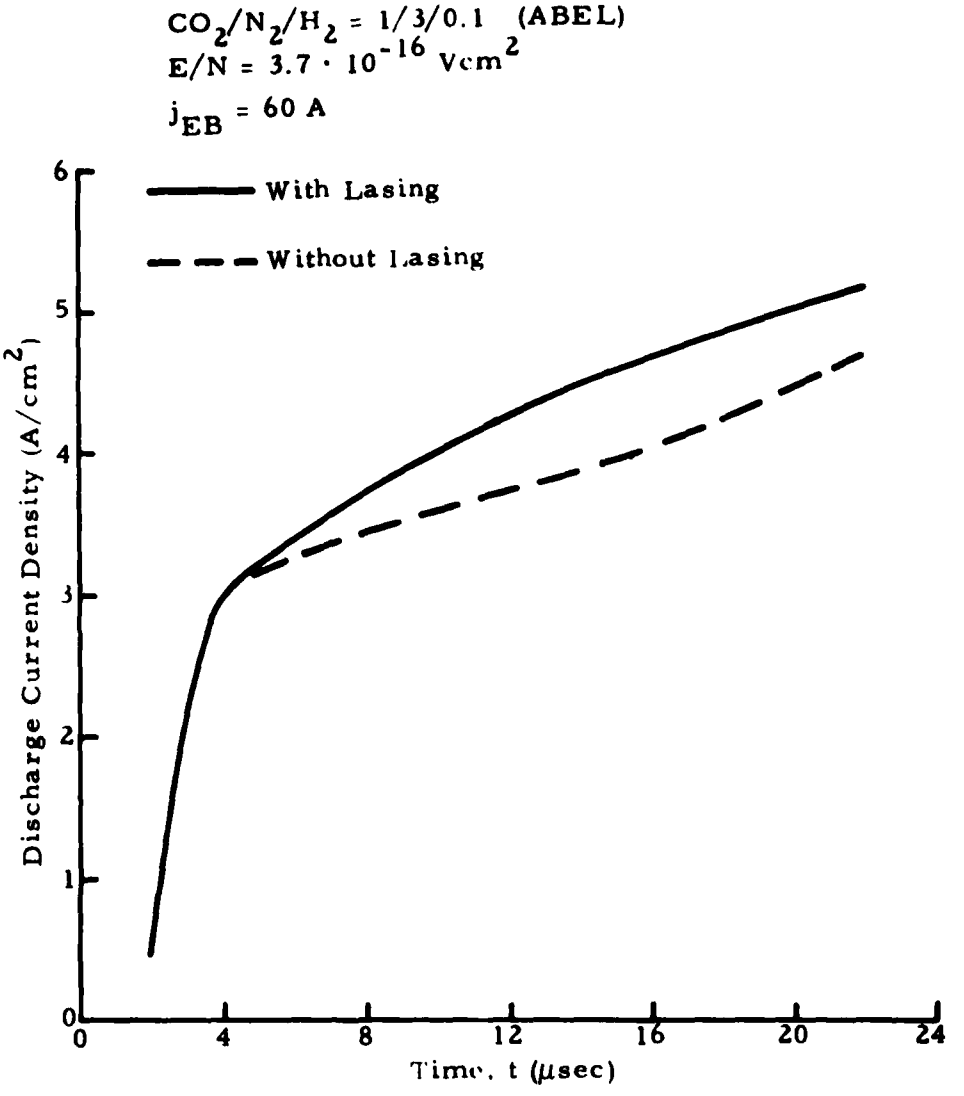

Fig. 35 - Discharge Current Density Temporal Distribution

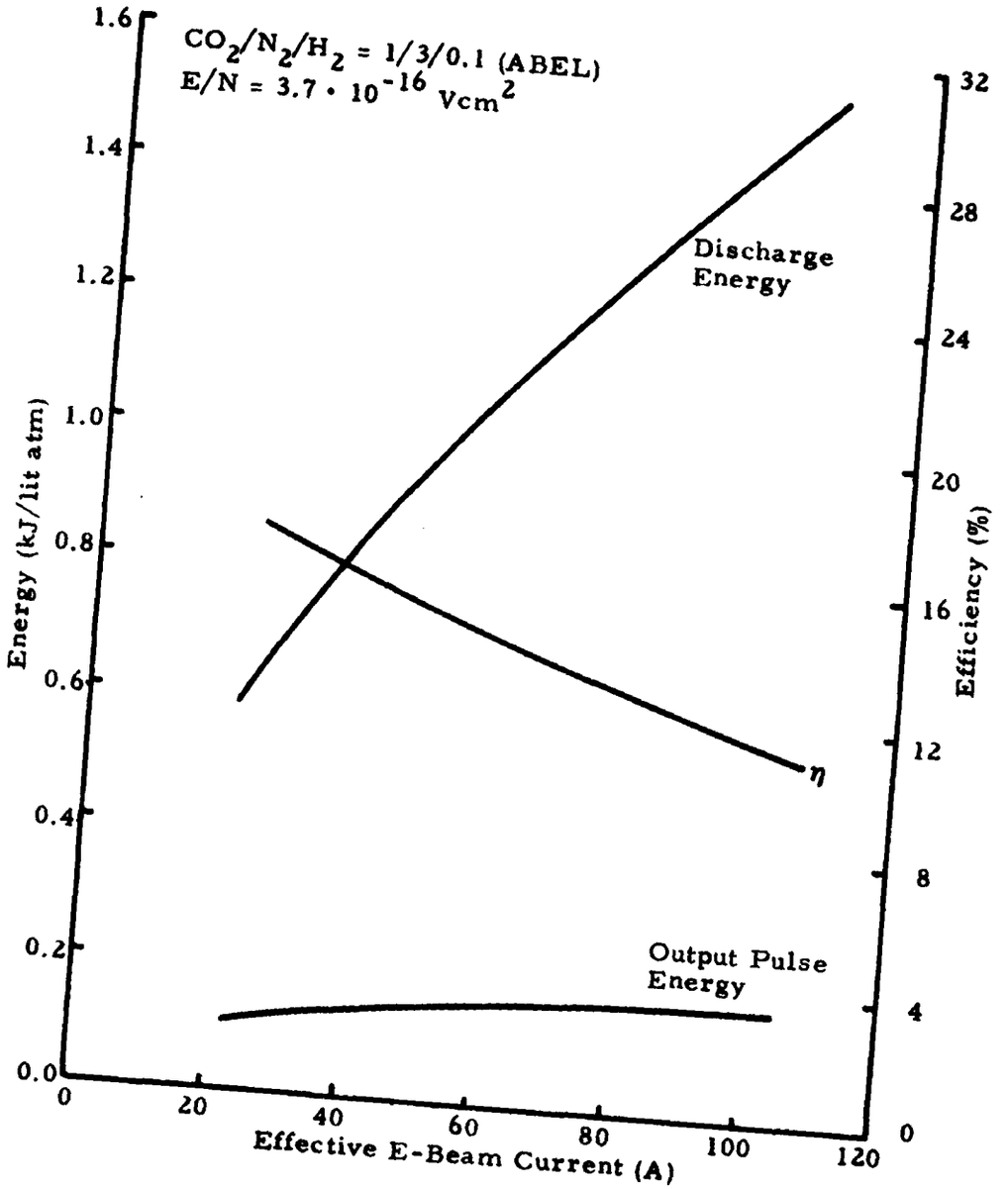

Fig. 36 - Discharge Energy Loading, P(18) Laser Pulse Energy, and Efficiency as Function of Effective E-Beam Current

4. ANALYSIS OF TEST CASES

4.1 AFWL PULSAR MODELING

The PULSAR device is a closed cycle, electron-beam sustained electric discharge laser presently under development at AFWL for the purpose of studying discharge stability, medium homogeneity, acoustics, energy loading and general discharge physics under closed cycle operation. Also planned is the investigation of fast startup transients. The purpose of this section is to describe a modeling effort specifically aimed at investigating the effects of discharge generated contamination of PULSAR closed cycle operation.

4.1.1 Open Cycle Performance

Before directing our attention to closed cycle operation it is of interest to establish a reference frame in terms of open cycle operation. Table 4 lists some basic given characteristics for this device, such as nominal gas mixture, initial pressure and temperature, maximum discharge energy loading and basic cavity geometric data. The pulse duration times were assumed based on given data for the Army Small Circulator to be discussed later. Initial calculations also assumed a discharge potential of 25 kV and an effective electron beam current density of 100 mA/cm^2, values which were specified for the Army Small Circulator. The indicated data yield an electric field to density ratio of $E/N = 1.36 \cdot 10^{-16}$ Vcm^2, a value which according to Fig. 8 is much too low to achieve efficient fractional energy transfer into the relevant vibrational levels. In fact, Fig. 8 indicates an optimum value of $E/N \approx 3.5 \cdot 10^{-16} \rightarrow 4.0 \cdot 10^{-16}$ Vcm^2. To stay below a value at which measurable discharge energy is consumed in the processes of electronic excitation and ionization we chose a discharge potential of 65 kV which yields a value of $E/N = 3.54 \cdot 10^{-16}$ Vcm^2, very close to the optimum as indicated by the Boltzmann code results. In reality, of course, the requirement to avoid arcing will impose the upper limit to this value. Results of discharge laser performance calculations (arbitrarily assuming a 50% Fabry-Perot resonator output coupling) as a

Table 4

AFWL PULSAR DEVICE DATA

(Ref. 17)

Gas Composition (Nominal)	$CO_2/N_2/H_2$ = 1/3/0.08
p (Initial)	760 torr
T (Initial)	200 K
Discharge Energy Loading	800 J/lit (max)
Electrode Gap	5 cm
Cavity Volume	5 x 5 x 25 cm
Gain Length	25 cm
Pulse Duration	
E-Beam	8 μsec
Discharge	10 μsec

function of E/N are shown in Fig. 37. It becomes clear then, that operation at optimum E/N with an effective electron beam current of 100 mA/cm^2 for the assumed pulse duration given in Table 4 far exceeds the energy loading limit of the PULSAR hardware. Since discharge energy loading, for recombination dominated plasmas, is roughly proportional to the square root of the effective electron beam current, decreasing the effective electron beam current while maintaining the optimum electric field should lower the discharge energy loading to an acceptable value. The results of these calculations are shown in Fig. 38, indicating an upper limit of around 30 mA/cm^2 for the effective electron beam current density. The output energy and the efficiency vary quite strongly as a function of the effective electron beam current, as indicated in Fig. 39. It should be noted that lowering the effective E-beam current density from 100 mA/cm^2 to 30 mA/cm^2 also lowered the output energy by approximately 25%, but increased the efficiency by roughly 75%. To illustrate further the effect of E-beam current density on the discharge, secondary electron densities and gas temperatures are shown as a function of time during the pulse in Figs. 40 and 41, respectively. Summarizing the discussion up to this point, we have, for the conditions given in Table 4, determined the optimum electric field strength from the results of the Boltzmann code. For this value, variations in the effective electron beam current density have shown that a current density of 30 mA/cm^2 is consistent with the discharge energy loading capability of the PULSAR discharge hardware. We are now in a position to investigate the response of the system to variations in gas mixture composition.

It is of particular interest to study variations in the H_2 concentration of the nominal $CO_2/N_2/H_2$ = 1/3/0.08 mixture. Since H_2 is needed to provide V-T relaxation of the CO_2 bending mode, thus providing a drain for the lower laser level population, the presence of H_2 also is responsible in this system for the formation of electrophilic by-products such as HNO_2, HNO_3 and HO_2NO_2. The question arises: can a reduction in H_2 concentration minimize the contaminant formation without adversely effecting output power and lasing efficiency?

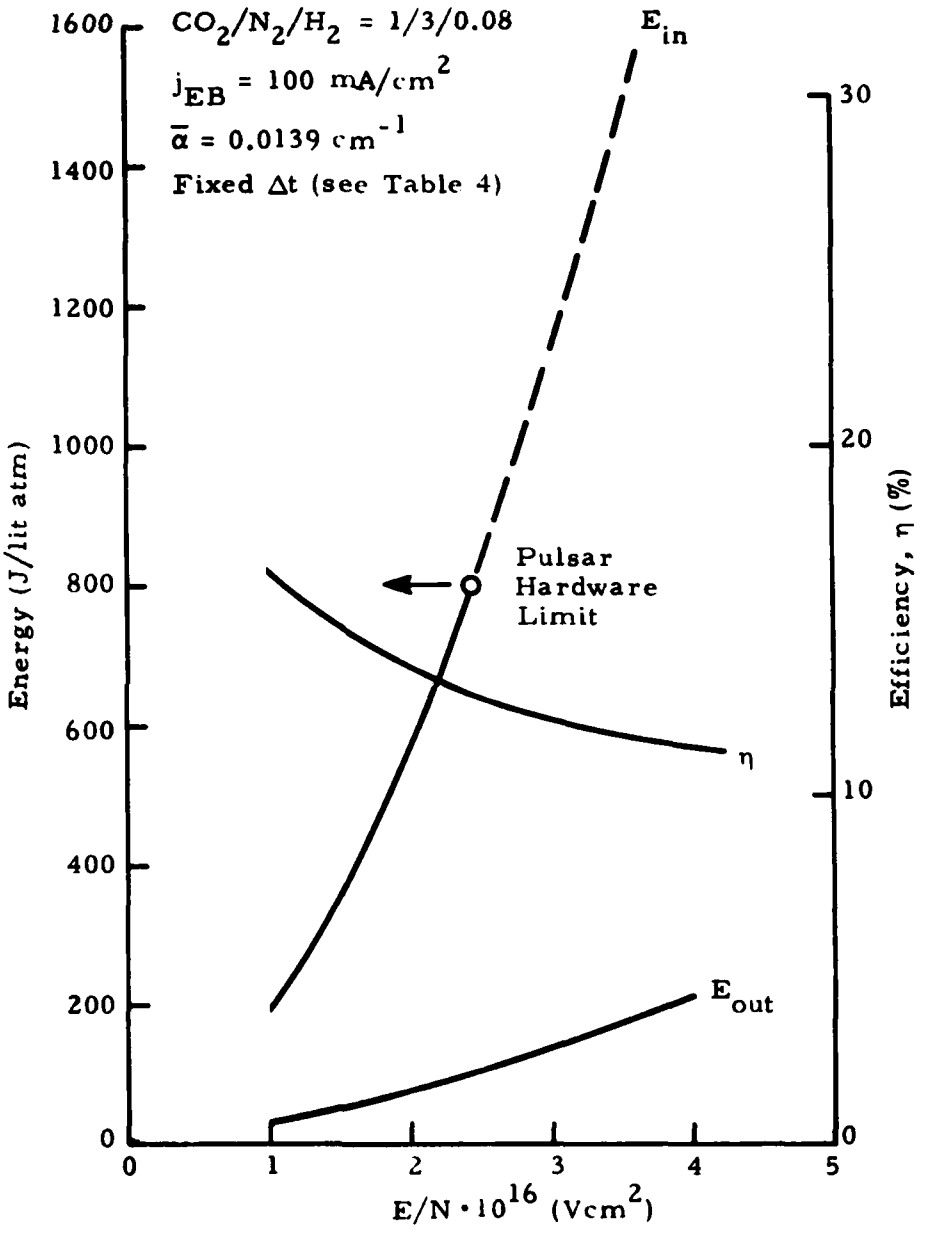

Fig. 37 - Discharge Energy Loading, Output and Efficiency as Function of E/N

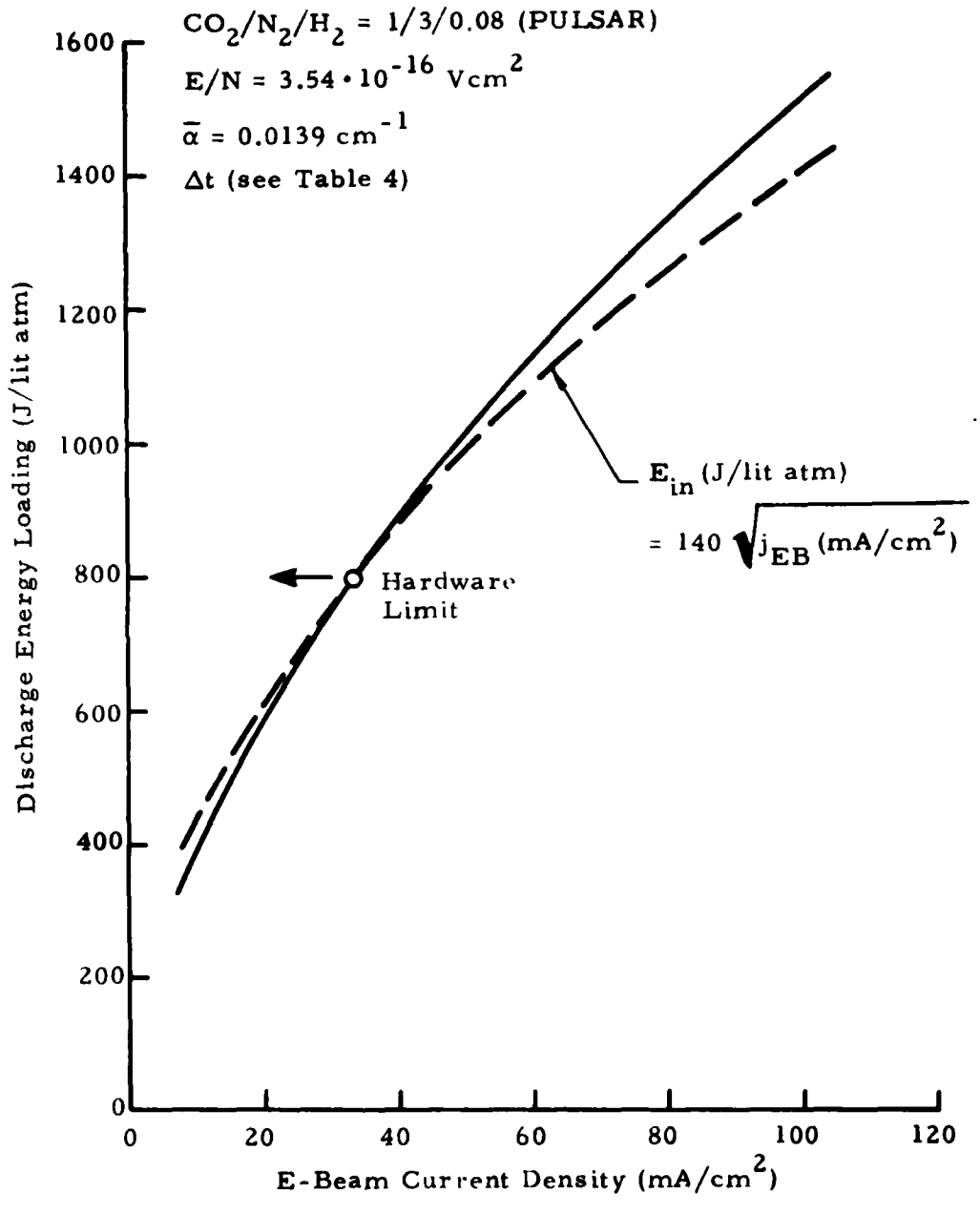

Fig. 38 - Discharge Energy Loading as Function of E-Beam Current Density (Open Cycle)

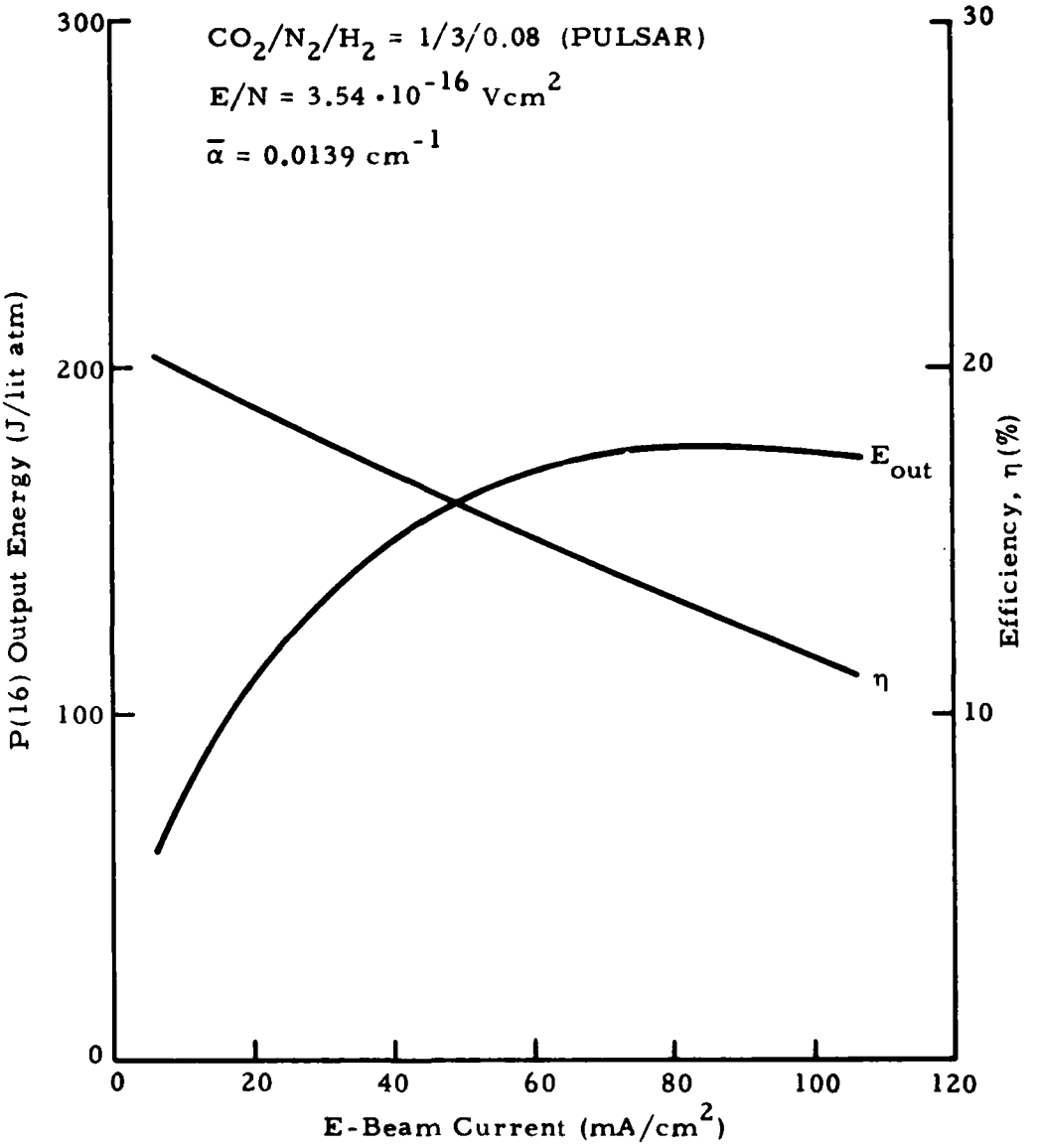

Fig. 39 - Output Pulse Energy and Efficiency as Function of E-Beam Current Density (P(16), Open Cycle)

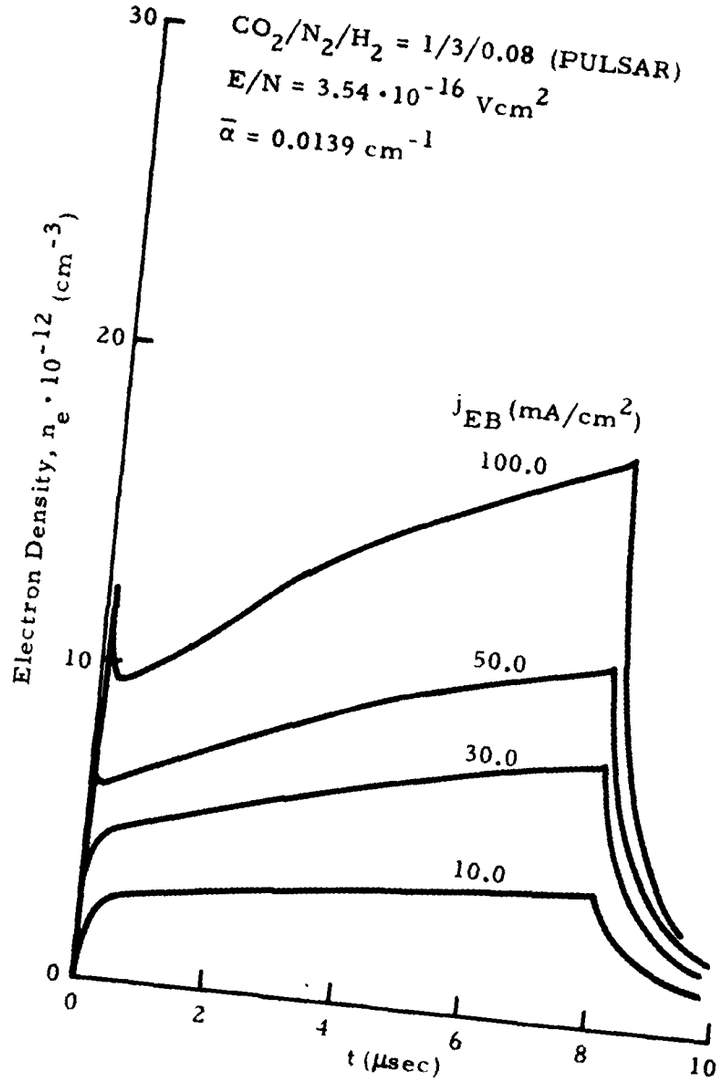

Fig. 40 - Secondary Electron Density as Function of E-Beam Current Density (Open Cycle, with Lasing)

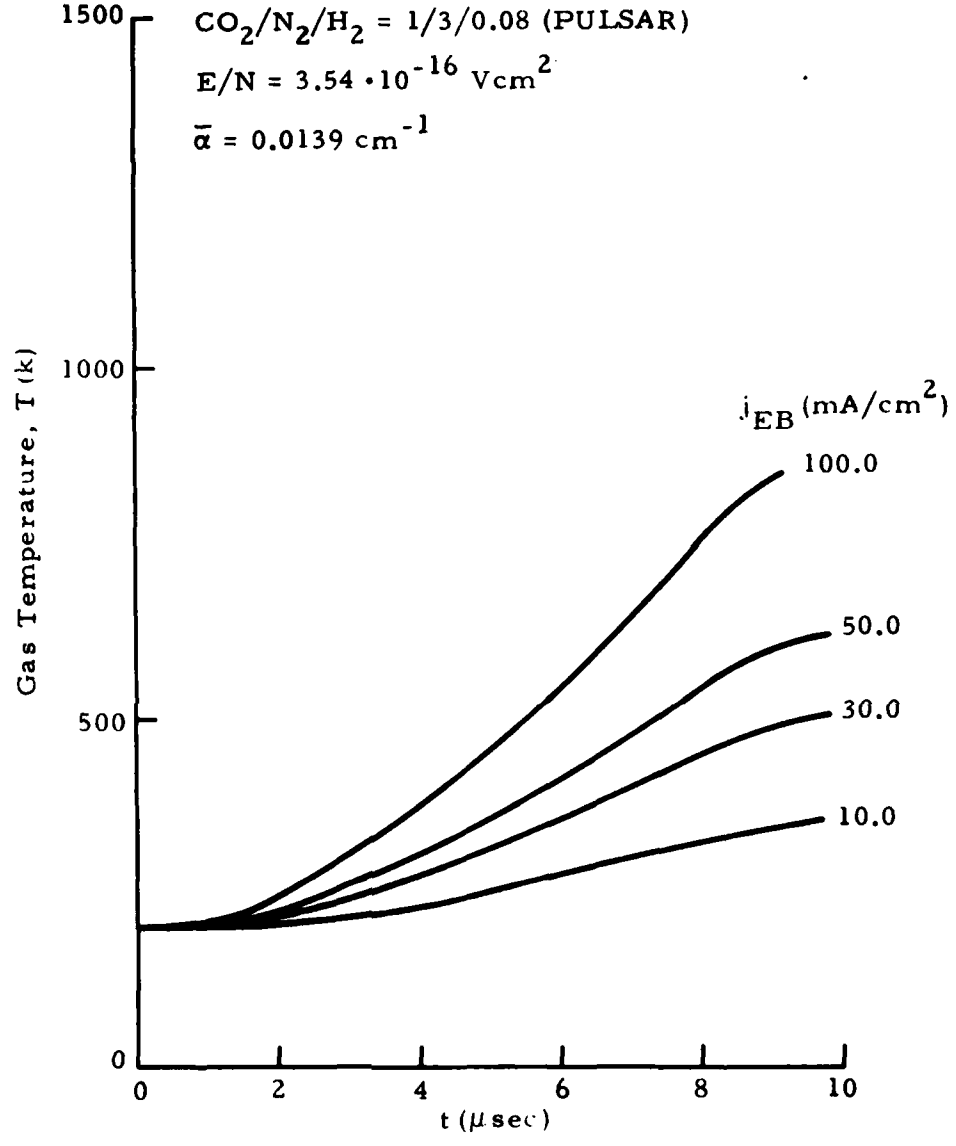

Fig. 41 - Gas Temperature as Function of Time for Varying E-Beam Current Density (Open Cycle, with Lasing)

Again, it is illustrative to study this effect for open cycle (or single pulse) operation. It is found that the gas mixture indeed shows optimum performance for 0.08 parts H_2 as shown in Fig. 42. Both output energy and efficiency show a broad, flat optimum with relatively little change between 0.05 and 0.16 parts H_2. Lowering the H_2 content below 0.05 will cause a strong decrease in both output energy and efficiency. From Fig. 43, which shows the corresponding discharge current density distributions as a function of time and H_2 content, it is concluded that discharge energy loading is not much affected by changes in the H_2 concentration for H_2 content varying between 0.02 and 0.16. For 0.005 the energy input is about 6.8% higher than for 0.08. Output intensity distributions of the P(16) transition as a function of H_2 content are shown in Fig. 44. Figure 45 shows some typical discharge current densities without the effect of lasing. It is noted that a slight increase in current density is obtained as the H_2 content is lowered from 0.08 to 0.02. It should be noted that it is difficult to change any single parameter without affecting others and this may provide the explanation here. As the H_2 content is reduced from 0.08 to 0.02 at constant pressure, the density increases by 1.4% while the discharge power input increases by 2.64%. Since, to a first approximation, the electron density is proportional to ρ^2, squaring the density yields $\Delta\rho^2 \approx 2.8\%$, hence the correspondingly higher current density. Concluding the open cycle analysis, Fig. 46 shows small signal gain distributions for varying H_2 concentrations. While the amount of H_2 does not greatly affect the small signal gain, it does noticeably affect the open cycle lasing performance as already shown in Figs. 42 and 44.

While we conclude from Fig. 43 that discharge energy loading is nearly independent of H_2 concentration (for the range from 0.02 to 0.16 parts H_2), it is noted that over the same range lasing causes the discharge energy loading to be between 4 and 6% higher than without lasing as shown in Fig. 47. For open cycle operation the formation of contaminants in the discharge should be important only if it affects the electron density during the actual pulse. Figure 48 shows that lasing has a negligible effect on open cycle plasma by-product formation except for NO_2. The likely principal cause for the increase is discharge energy loading with lasing is the observed faster deactivation of high vibrationally excited levels (particularly $N_2(1)$, see Fig. 49). This leads to a higher gas temperature which effects the rates such that the electron concentration is increased as compared to the non-lasing case.

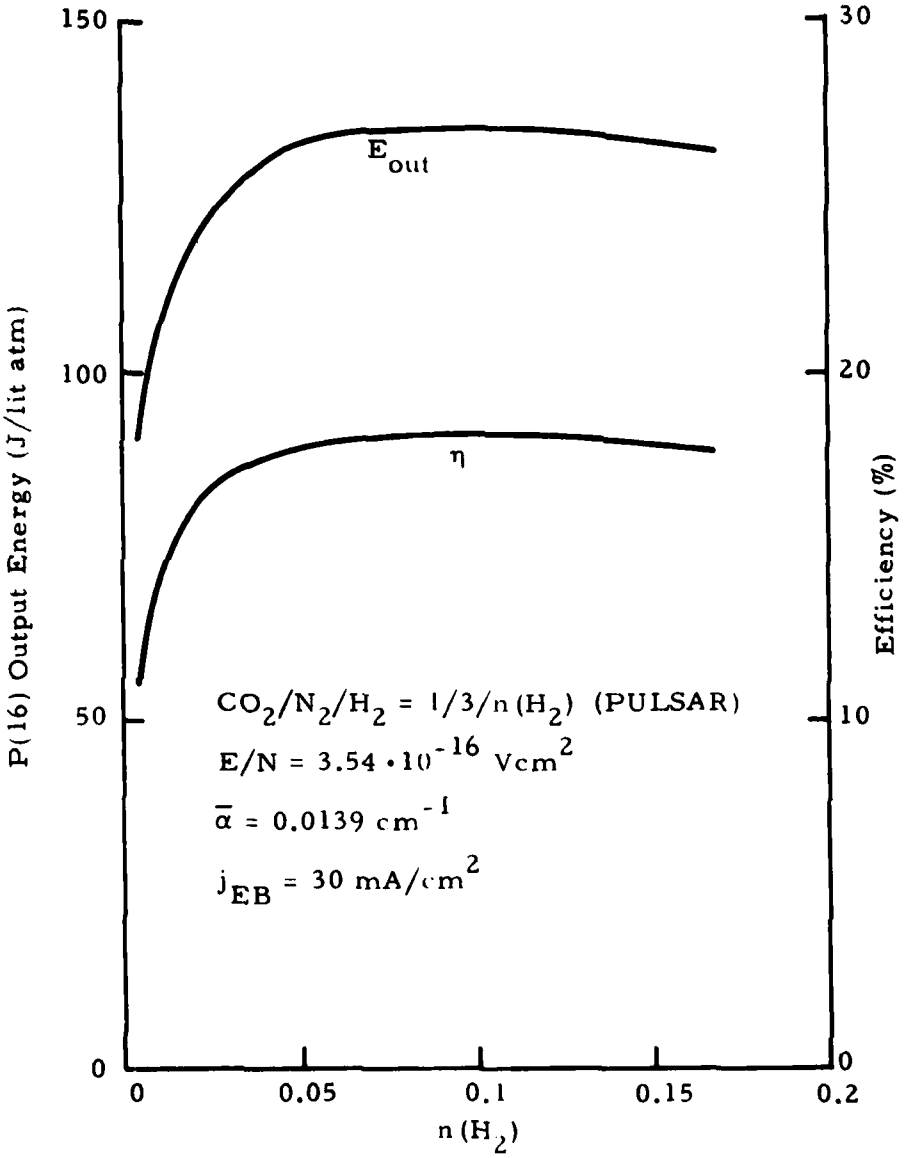

Fig. 42 - P(16) Output Energy and Efficiency as Function of H_2 Content (P(16), Open Cycle)

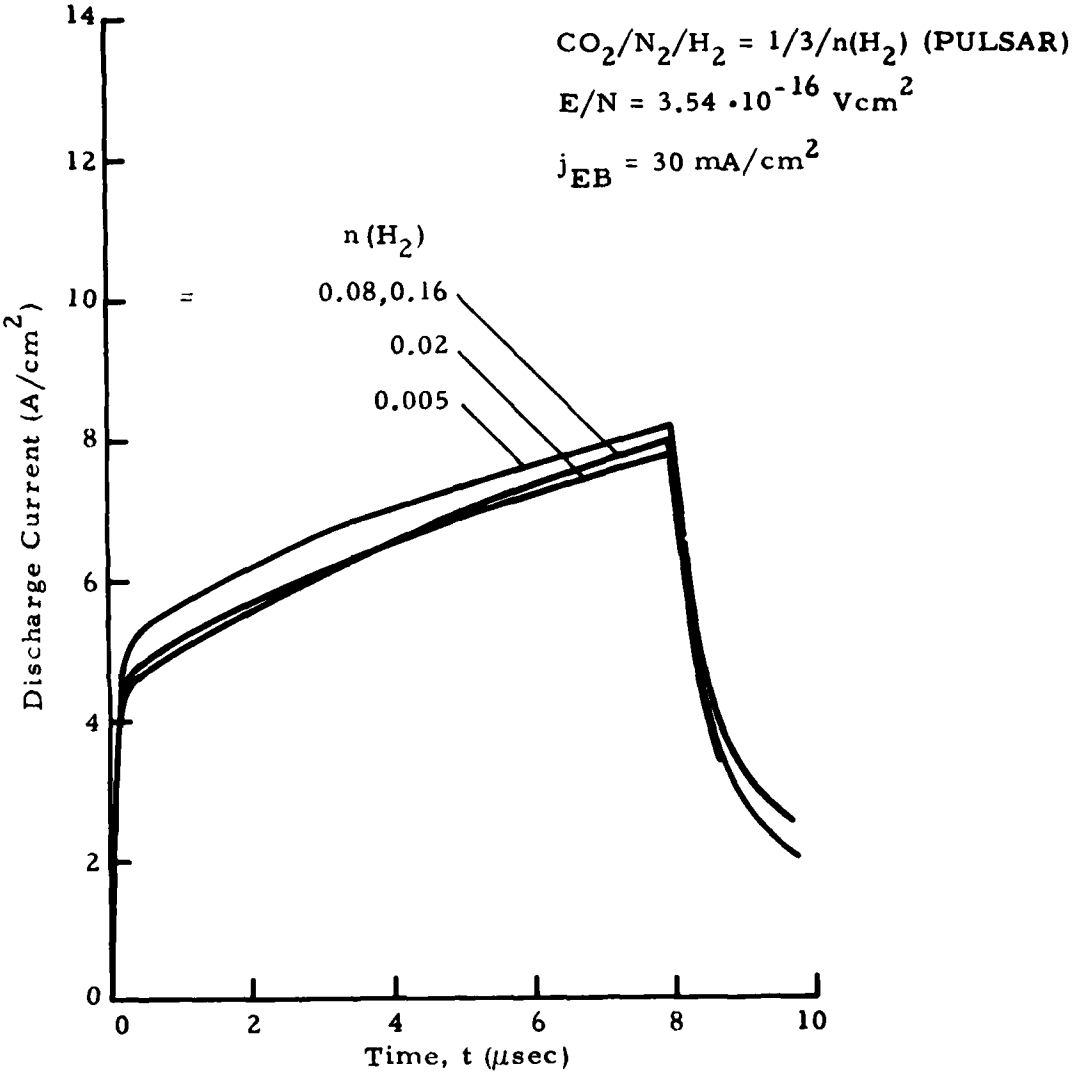

Fig. 43 - Discharge Current as Function of Time and H_2 Concentration (Open Cycle, with Lasing)

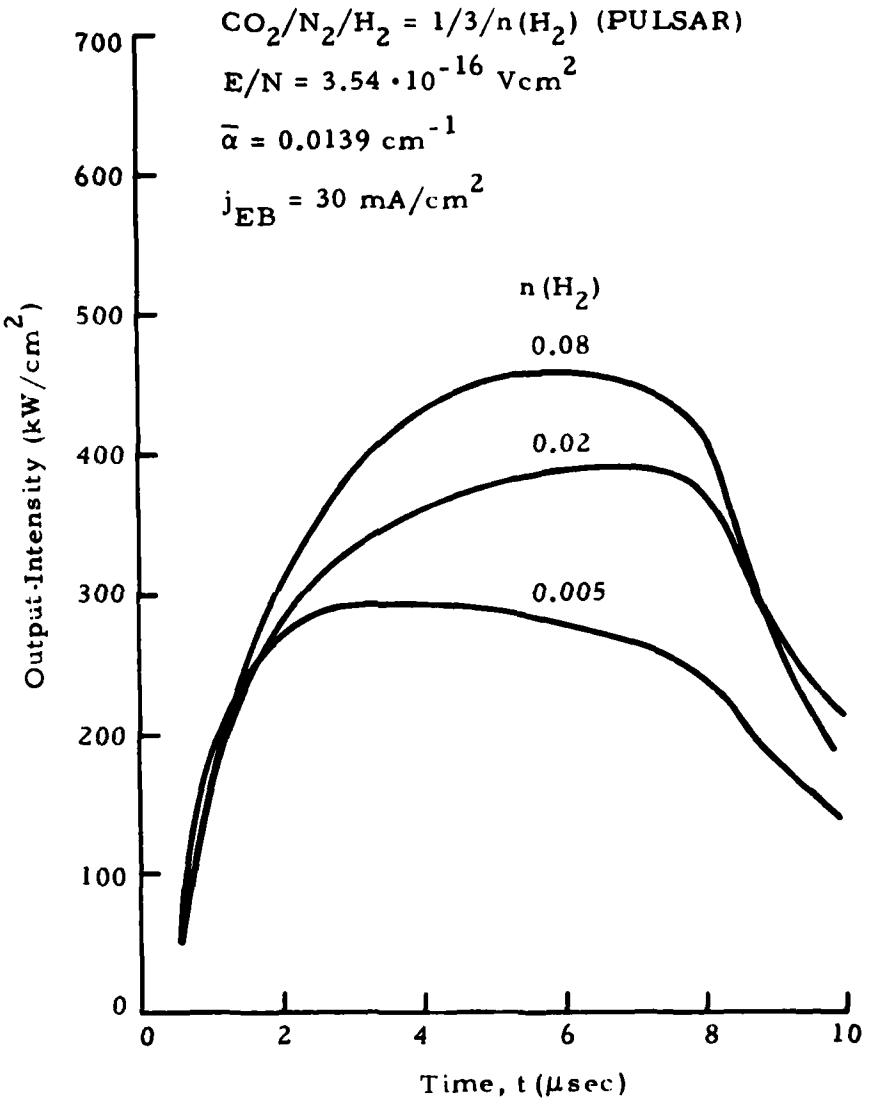

Fig. 44 - Output Intensity as Function of Time and H_2 Concentration (P(16), Open Cycle)

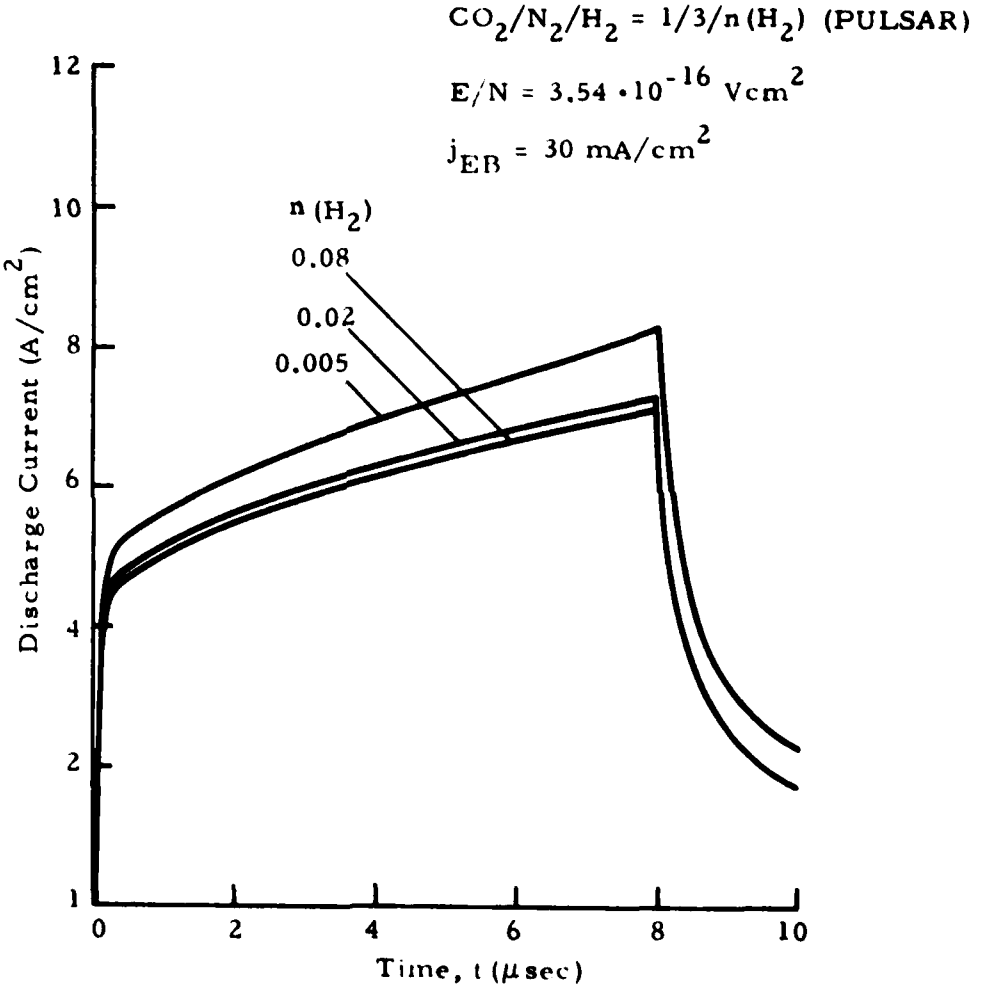

Fig. 45 - Discharge Current Density as Function of Time and H_2 Content (Open Cycle, No Lasing)

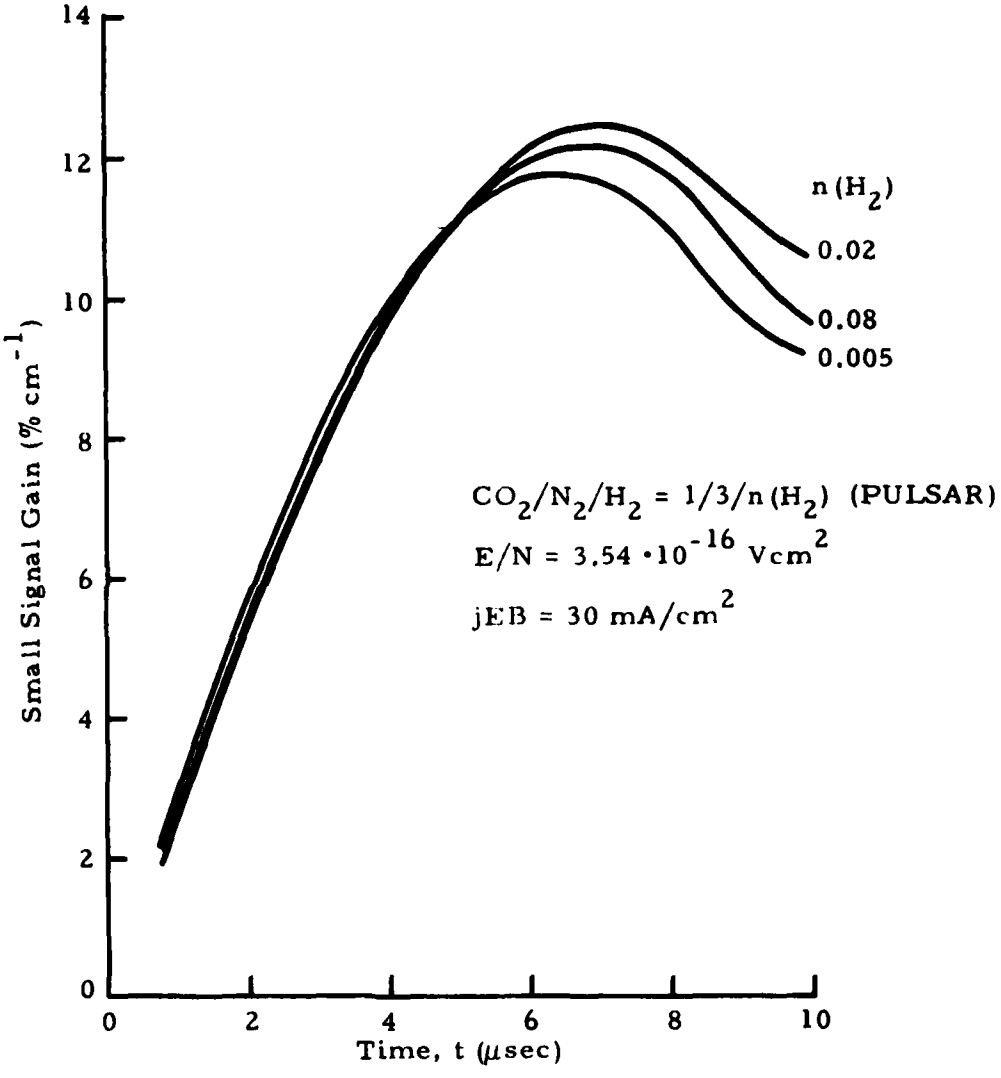

Fig. 46 - Small Signal Gain, P(16) as Function of Time and H_2 Concentration (Open Cycle)

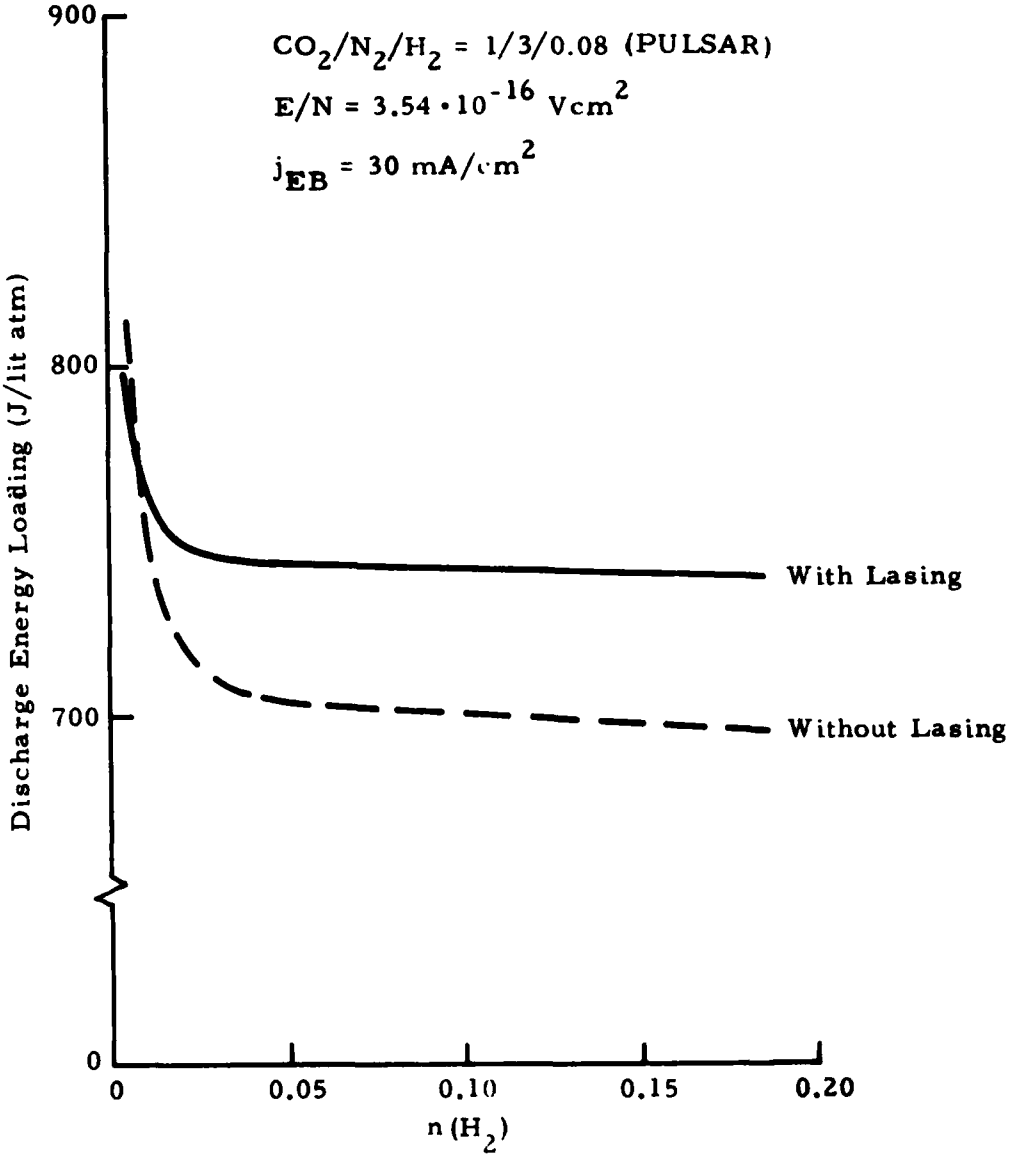

Fig. 47 - Effect of Lasing on Discharge Energy Loading (Open Cycle)

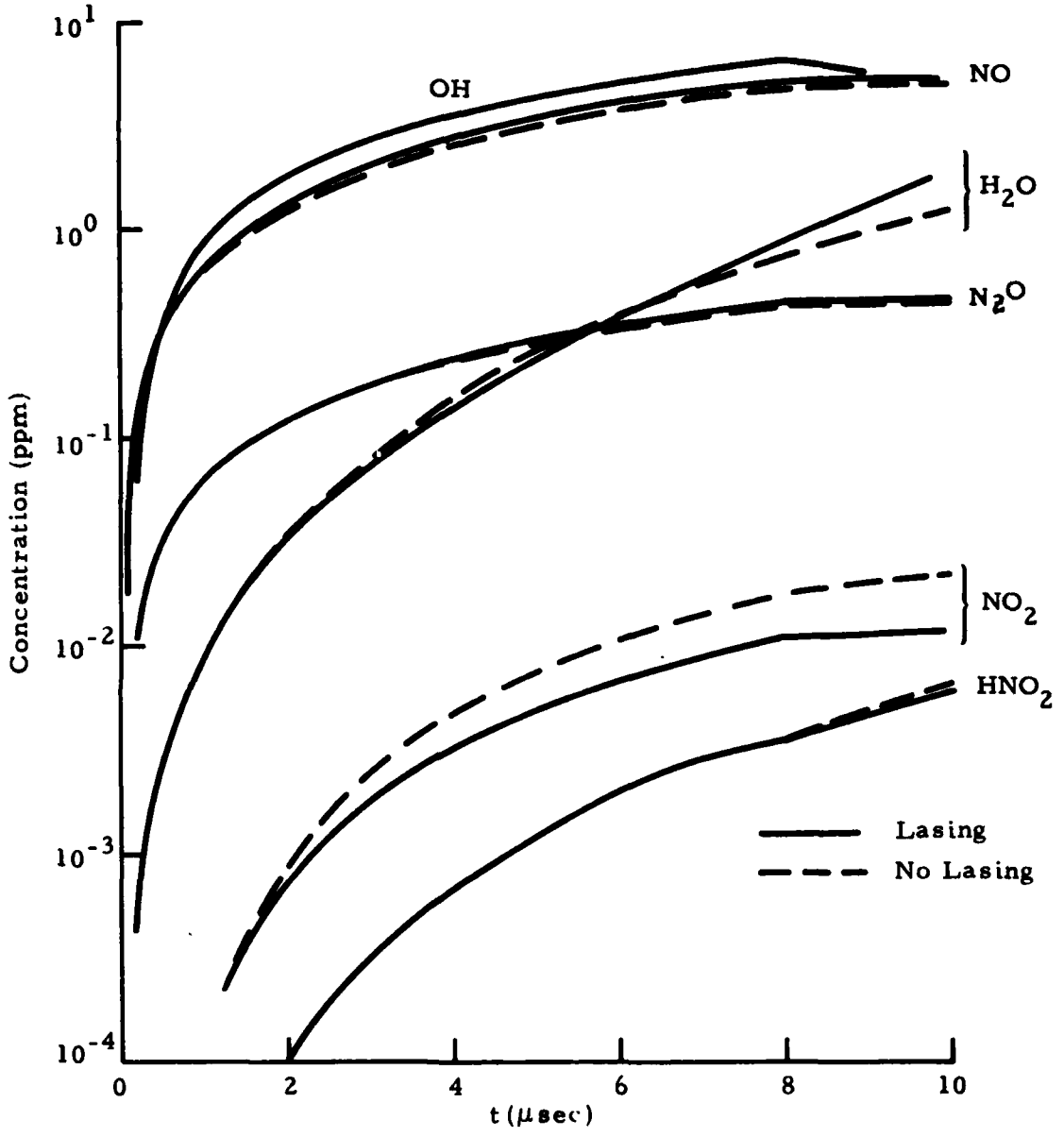

Fig. 48 - Effect of Lasing on Contaminant Generation During Discharge Pulse (Open Cycle) for $CO_2/N_2/H_2$ = 1/3/0.08 (PULSAR)

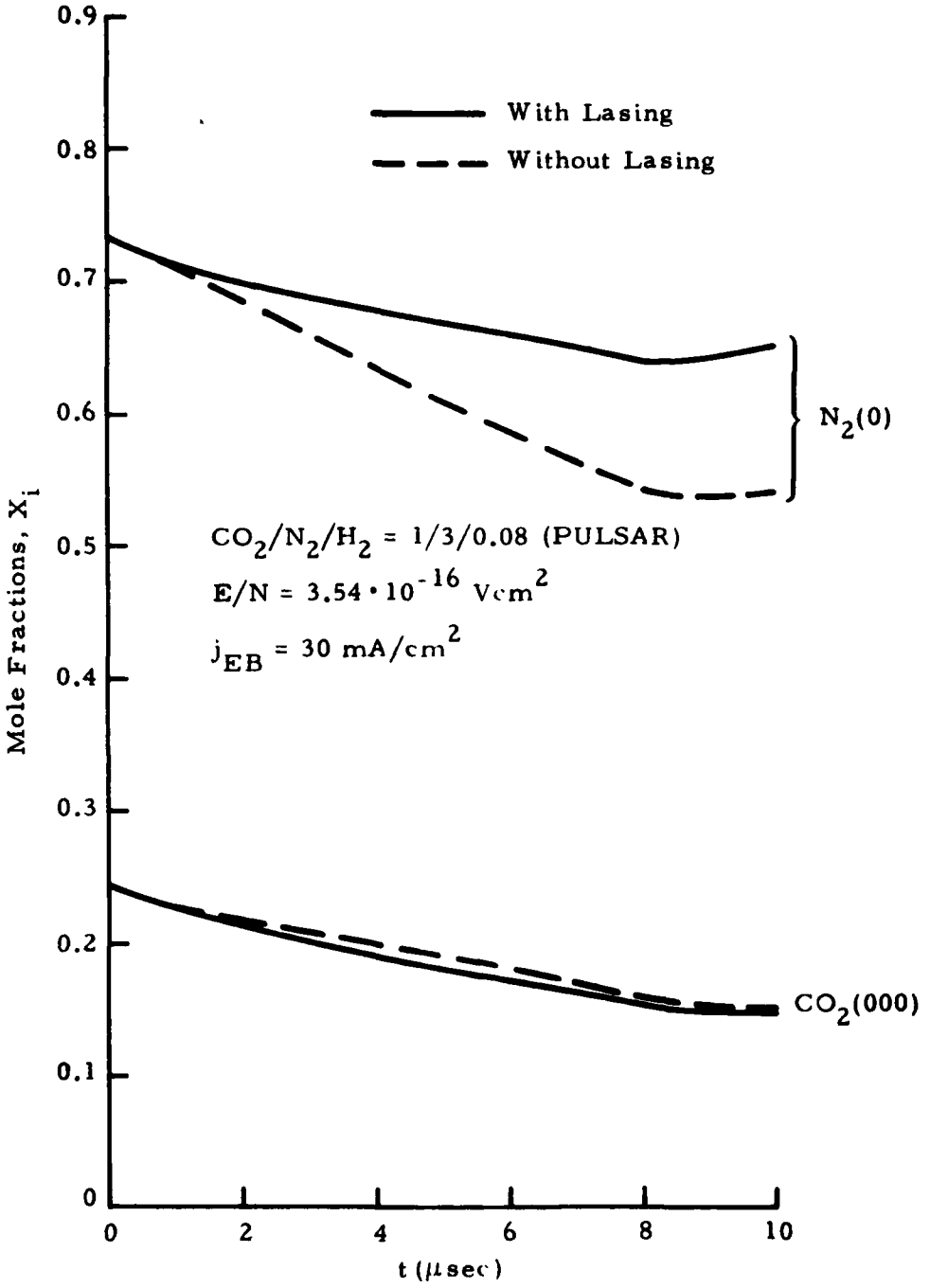

Fig.49 - Effect of Lasing on Dominant Species (Open Cycle)

4.1.2 Closed Cycle Performance

The simulation of closed cycle operation is performed by continuing the plasma chemistry calculations beyond the discharge pulse around the recirculation cycle as described in Section 2.3. Based on typical post-pulse gas temperatures and the given cavity geometry the time for the adiabatic expansion was estimated to be about 100 μsec, and this value was used throughout the closed cycle performance modeling of this case.

Initial calculations used a time frame of Δt = 5 msec with a linear decrease of the temperature to simulate the effect of a heat exchanger in the remainder of the cycle. Since the results showed still very strong species gradients at the end of this assumed cycle, the time frame was arbitrarily extended to Δt = 1.0 sec. The effect of different cycle times on normalized discharge energy loading for five cycles is shown in Fig. 50. Not only had all species gradients become vanishingly small for Δt = 1.0 sec, the power loading decay was substantially less than for the shorter time frame. These results show that it is rather important to employ a realistic history of temperature versus time in the simulation of the recirculation loop.

Realistic gasdynamic conditions around the PULSAR recirculation loop were obtained from AFWL (Ref. 17). Table 5 lists their estimates for velocity and temperature as a function of distance around the tunnel. Static pressure values were found to show only small variations and were therefore ignored. The main interest here is the temperature, and its effect on density. Logarithmic differentiation of the equation of state shows that temperature variations have a far more pronounced effect on density than small pressure variations. To obtain a better picture of the recirculation loop, velocity and temperature from Table 5 are plotted versus distance in Figs. 51 and 52, respectively. To establish the temperature versus time history, the reciprocal velocity is integrated versus flow distance assuming a linear variation between given data points. The results are tabulated in Table 6 and displayed in Fig. 53, along with a typical temperature distribution during the discharge, adiabatic expansion and early part of the cycle up to the first heat exchanger. From this

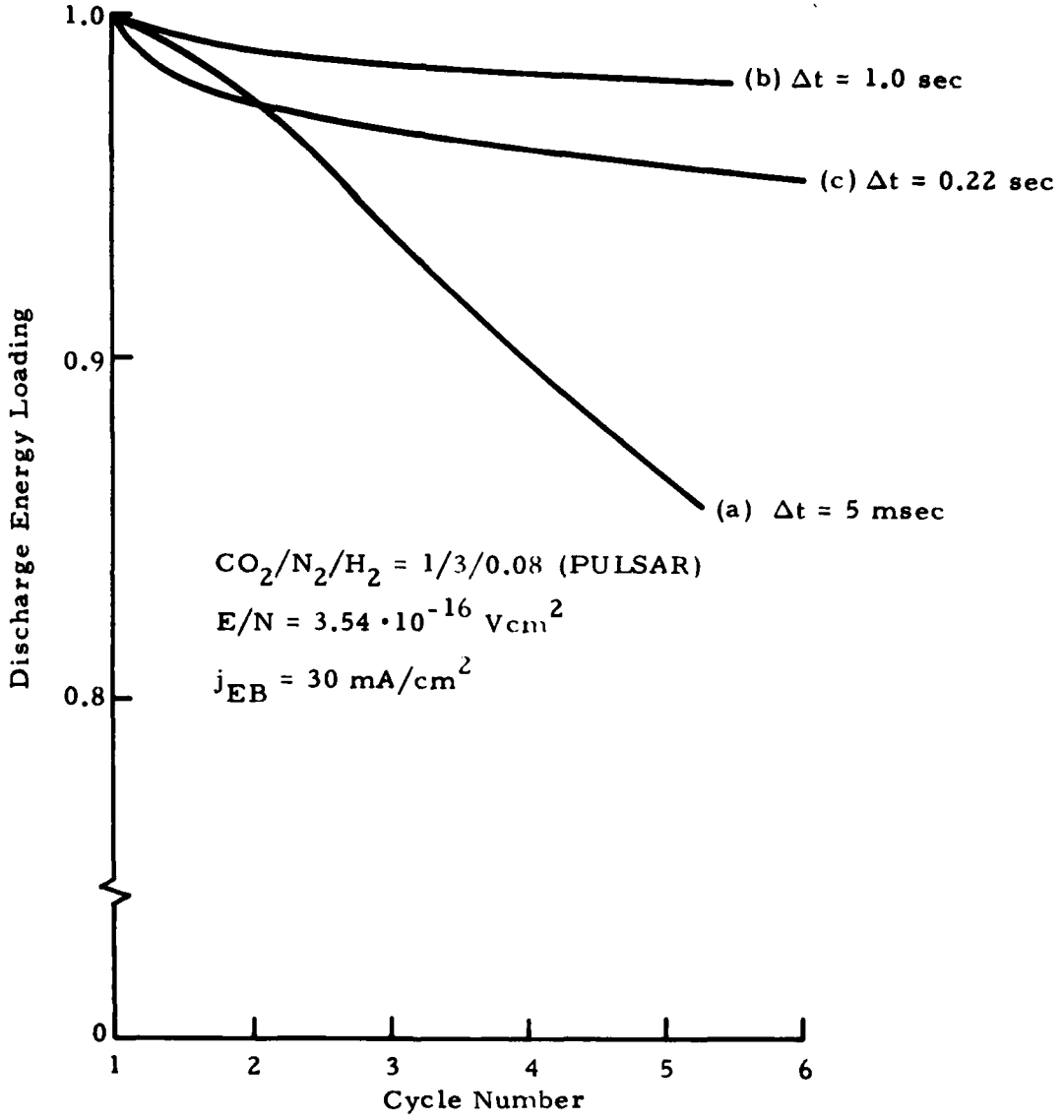

Fig. 50 - Effect of Cooling Cycle Modeling on Recirculation Results (Without Lasing)

Table 5

AFWL PULSAR DEVICE
RECIRCULATION LOOP DATA

Station	x (cm)	u (m/s)	T (K)	Remarks
0	0.0	24.4	208	Cavity Entrance
1	5.0	64.5	541	Cavity Exit
2	35.5	64.5	541	End, Hot Duct
3	85.5	25.0*	541	End, Diffuser
4	100.0	25.0	541	Heat Exchanger 1
5	130.5	25.0	284	End, Heat Exch. 1
6	145.0	24.0	284	End, Duct
7	178.0	65.0	284	End, Nozzle
8	197.0	65.0	284	End, Duct
9	260.0	74.5	350	End, Blower
10	276.0	74.5	350	End, Duct
11	337.0	15.0	350	End, Diffuser
12	437.0	18.0	350	End, Duct
13	472.0	15.0	208	End, Heat Exch. 2
14	487.0	15.0	208	End, Duct
15	521.0	24.4	208	End, Nozzle
16	560.0	24.4	208	End, Duct

*Value estimated based on diffuser area ratio.

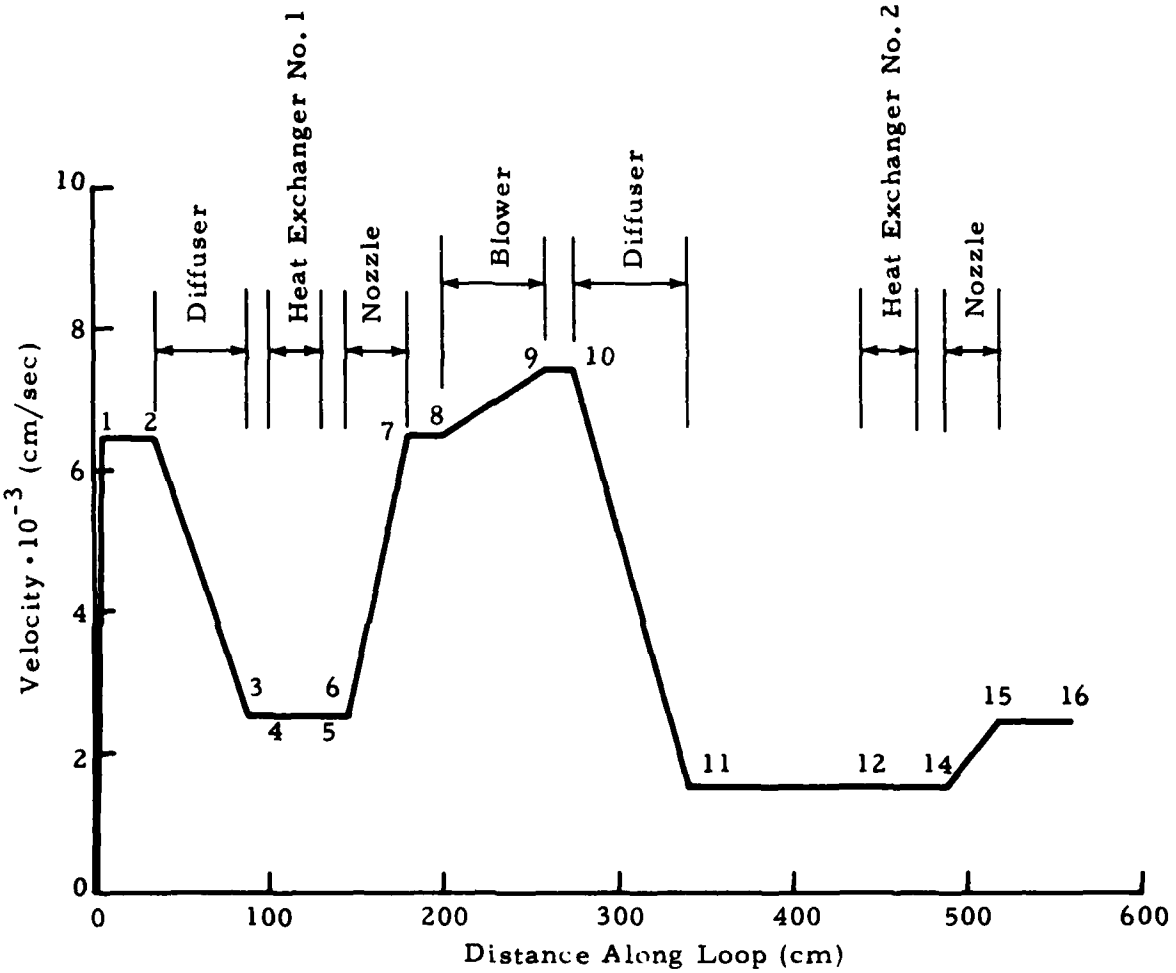

Fig. 51 - Predicted Velocity Distribution Around AFWL PULSAR Cycle (Ref. 17)

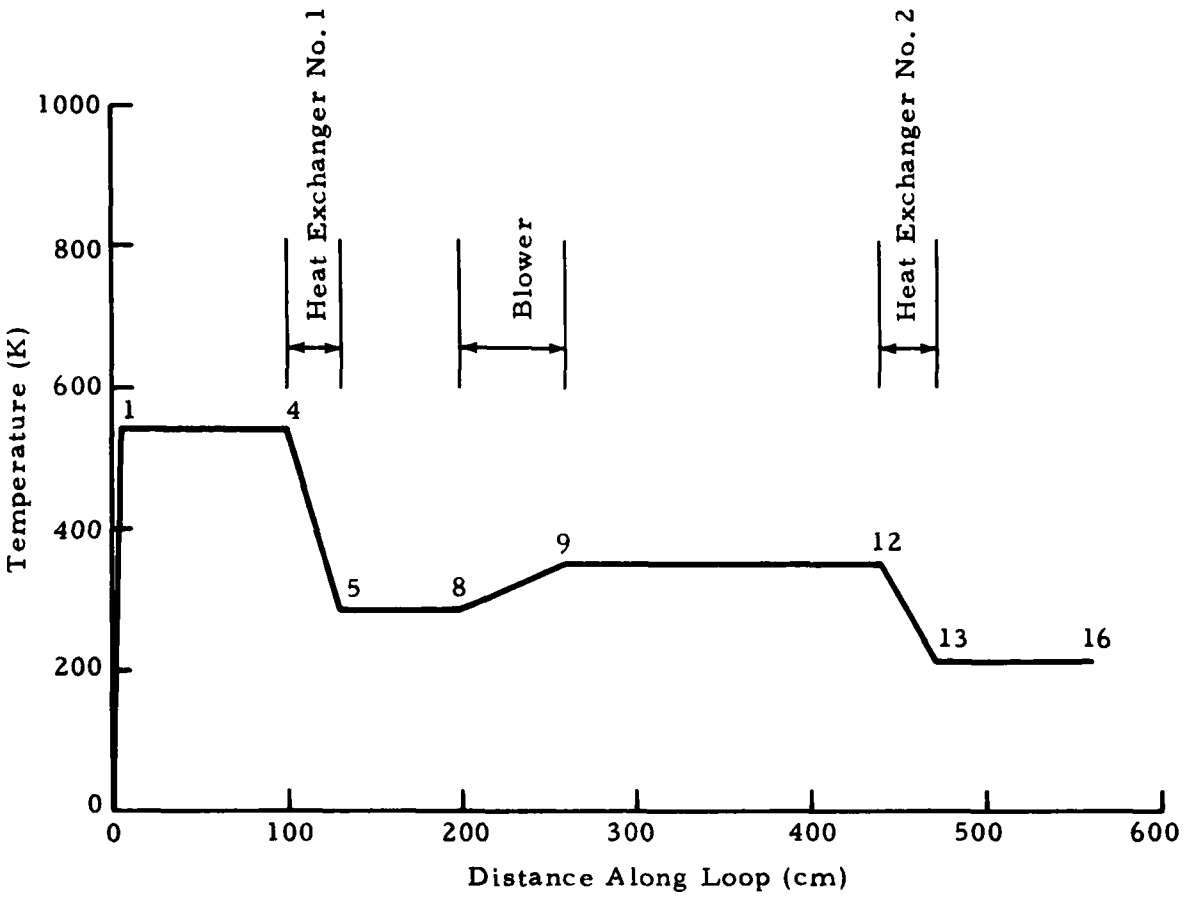

Fig. 52 - Predicted Temperature Distribution Around AFWL PULSAR Cycle (Ref. 17)

AD-A083 222 LOCKHEED MISSILES AND SPACE CO INC HUNTSVILLE AL HUN--ETC F/G 20/5
PLASMA CHEMISTRY PROCESSES IN THE CLOSED CYCLE EDL.(U)
JUL 79 J THOENES, S C KURZIUS DAAH40-78-C-0196
UNCLASSIFIED LMSC-HREC-TR-D568999 DRCPM-HEL-CR-79-11-VOL-1 NL

2 · 2

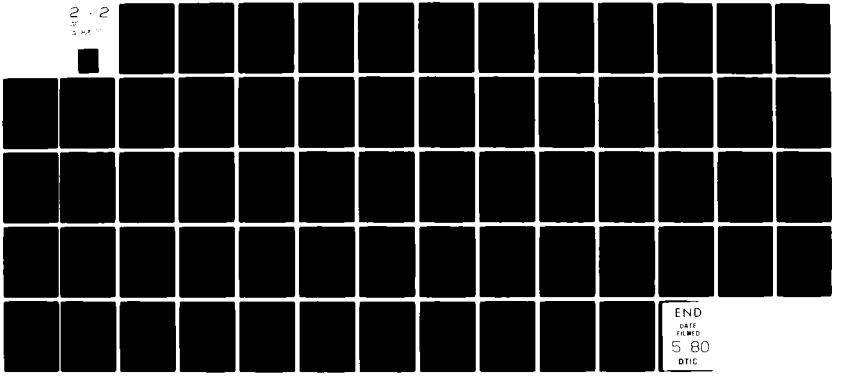

END
DATE FILMED
5 80
DTIC

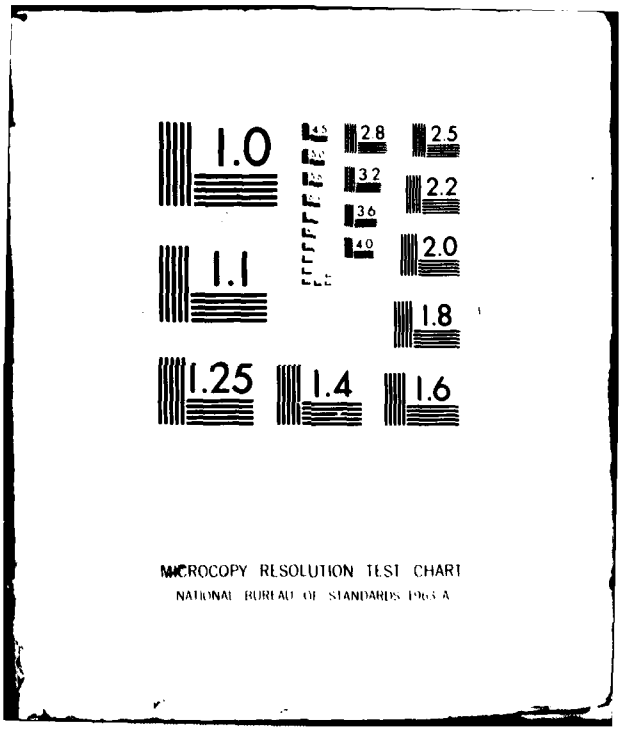
1.0
1.1
1.25
1.4
1.6
1.8
2.0
2.2
2.5
2.8
3.2
3.6
4.0
MICROCOPY RESOLUTION TEST CHART
NATIONAL BUREAU OF STANDARDS 1963 A

Table 6

RESULTS OF $\Delta t = \int_{x_{n-1}}^{x_n} \frac{dx}{u(x)}$

Station	Δt_{n-1}^{n} (sec)	$t = \sum \Delta t_{n-1}^{n}$ (sec)	T (K)
0	0.0	0.0	208
1	$1.21\ 10^{-3}$	$1.21\ 10^{-3}$	
2	$4.73\ 10^{-3}$	$5.94\ 10^{-3}$	
3	$1.20\ 10^{-2}$	$1.79\ 10^{-2}$	
4	$6.00\ 10^{-3}$	$2.39\ 10^{-2}$	( )*
5	$1.20\ 10^{-2}$	$3.59\ 10^{-2}$	284
6	$6.00\ 10^{-3}$	$4.19\ 10^{-2}$	284
7	$7.88\ 10^{-3}$	$4.98\ 10^{-2}$	284
8	$3.39\ 10^{-3}$	$5.32\ 10^{-2}$	284
9	$8.62\ 10^{-3}$	$6.18\ 10^{-2}$	350
10	$2.15\ 10^{-3}$	$6.39\ 10^{-2}$	350
11	$1.64\ 10^{-2}$	$8.03\ 10^{-2}$	350
12	$6.67\ 10^{-2}$	$1.47\ 10^{-1}$	350
13	$2.33\ 10^{-2}$	$1.70\ 10^{-1}$	208
14	$1.00\ 10^{-2}$	$1.80\ 10^{-1}$	208
15	$1.76\ 10^{-2}$	$1.98\ 10^{-1}$	208
16	$1.60\ 10^{-2}$	$2.14\ 10^{-1}$	208

*Temperature to be computed by code.

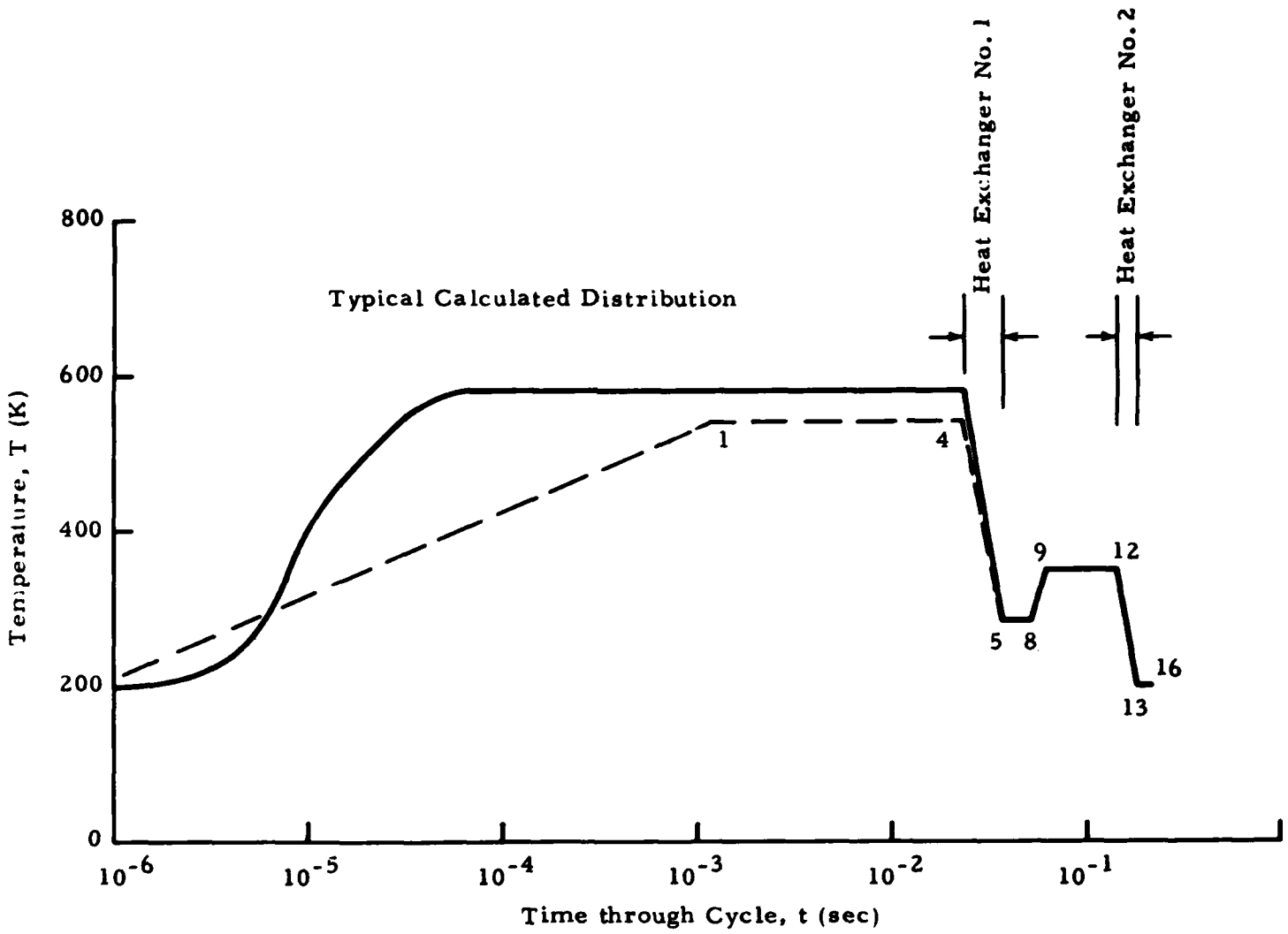

Fig. 53 - Temperature Distribution Around Cycle as a Function of Time

point onward the kinetics calculations simulate diabatic flow with the temperature prescribed as shown in Fig. 53. It is also recognized that the gas temperature in the hot duct and at the entrance of the first heat exchanger as calculated here is in close agreement with that resulting from the AFWL gasdynamic cycle analysis. Table 6 indicates a total cycle time of about 0.22 sec. The discharge energy loading as a function of recirculation using the computed cycle time of $\Delta t \approx 0.22$ sec is also shown in Fig. 50, falling in between the results for the previously assumed cycle times.

Having constructed a reasonably accurate model for closed cycle plasma chemistry analysis we can now attempt to determine the effect of variations in H_2 content of the basic $CO_2/N_2/H_2 = 1/3/0.08$ mixture on closed cycle laser performance. Calculations have been carried out for up to 15 cycles, with and without lasing. A typical run time on the AFWL/CDC Cyber 176 for one case is about 11 minutes with lasing, and slightly less without lasing. Results for the discharge energy loading as a function of recirculation and H_2 content are shown in Fig. 54. These results show that discharge energy loading is obviously higher with lasing as compared to the case without lasing, just as for open cycle operation. Note that the rate of decay increases as the H_2 content of the mixture is decreased.

The effect of reduced hydrogen content and recirculation on the laser power output is shown in Figs. 55 and 56. As can be seen, reducing the hydrogen content causes a decrease in power output, and this response is the same as for open cycle operation. Figure 56 also indicates that, with recirculation it is even more important than for open cycle operation to keep the hydrogen concentration close to the optimum, since the rate of decay is increased as the hydrogen concentration is reduced.

Figure 57 illustrates the build up of the major by-products during recirculation with lasing both for the nominal mixture and for one with reduced hydrogen content. The principal result is that reducing the hydrogen content will apparently lead to increased concentrations of NO, HNO_2 and HNO_3 thereby increasing the rate of electron attachment, which then results in

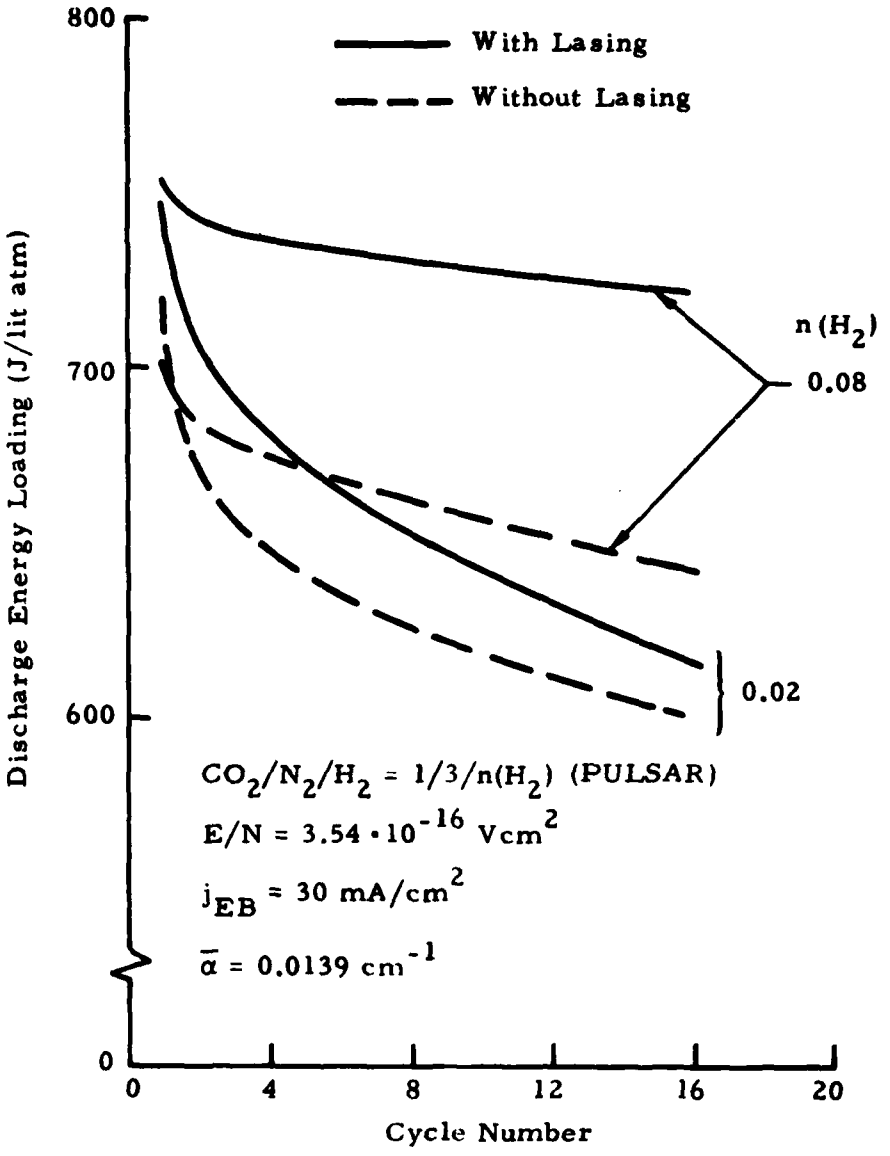

Fig. 54 - Discharge Energy Loading as Function of Recirculation and H_2 Content With and Without Lasing

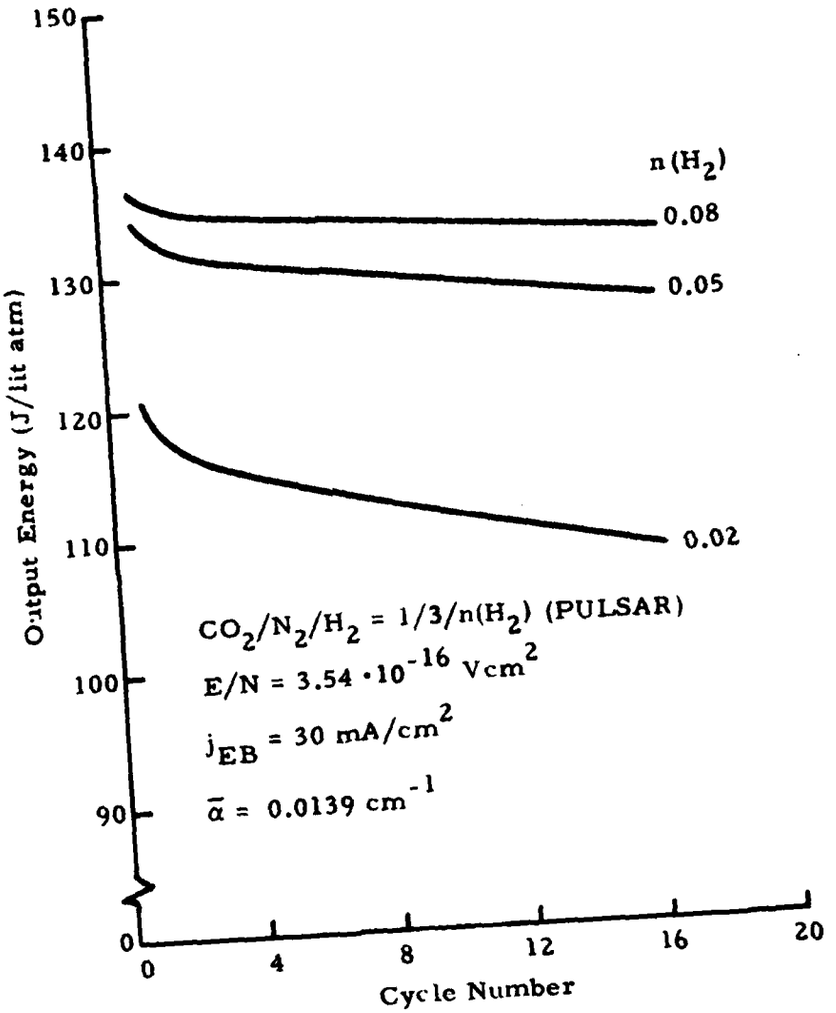

Fig. 55 - P(16) Laser Pulse Output Energy as Function of Recirculation and Gas Mixture Variations

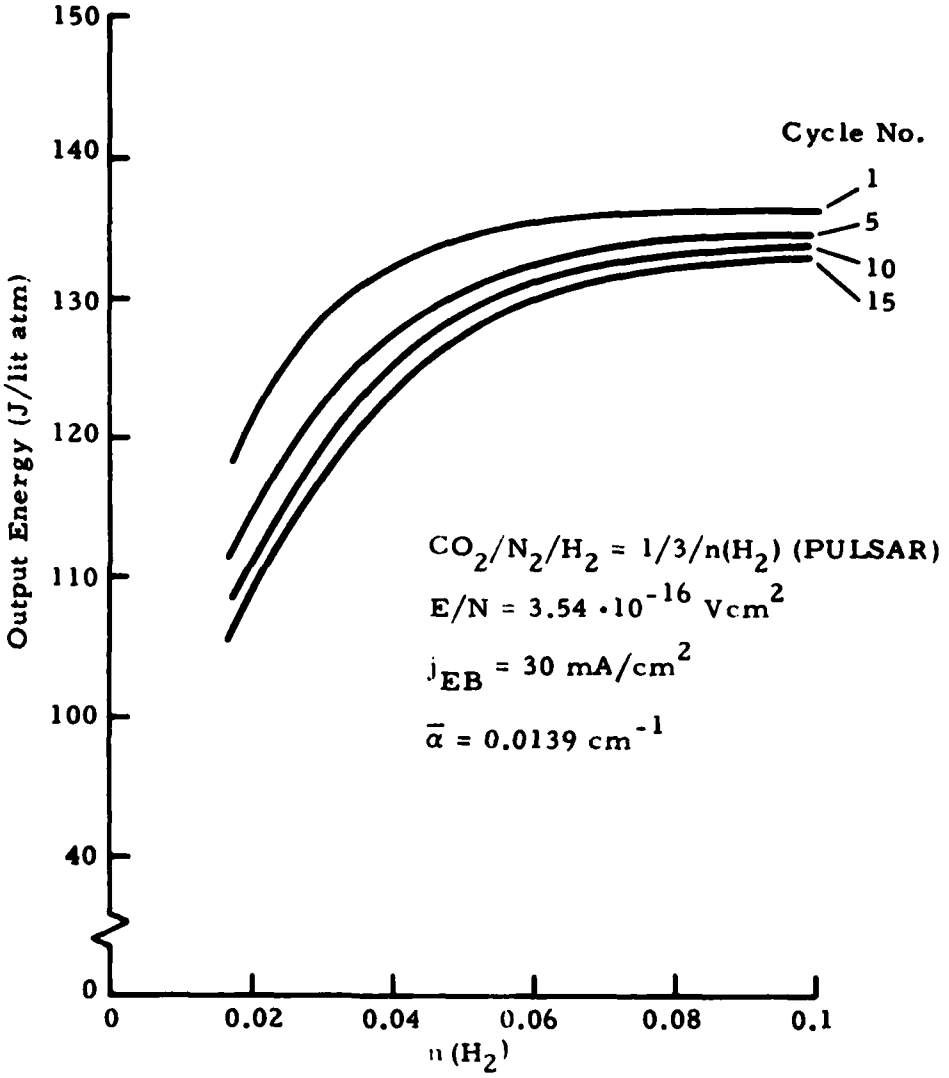

Fig. 56 - Laser Pulse Output Energy as a Function of Hydrogen Content, n(H_2) and Recirculation

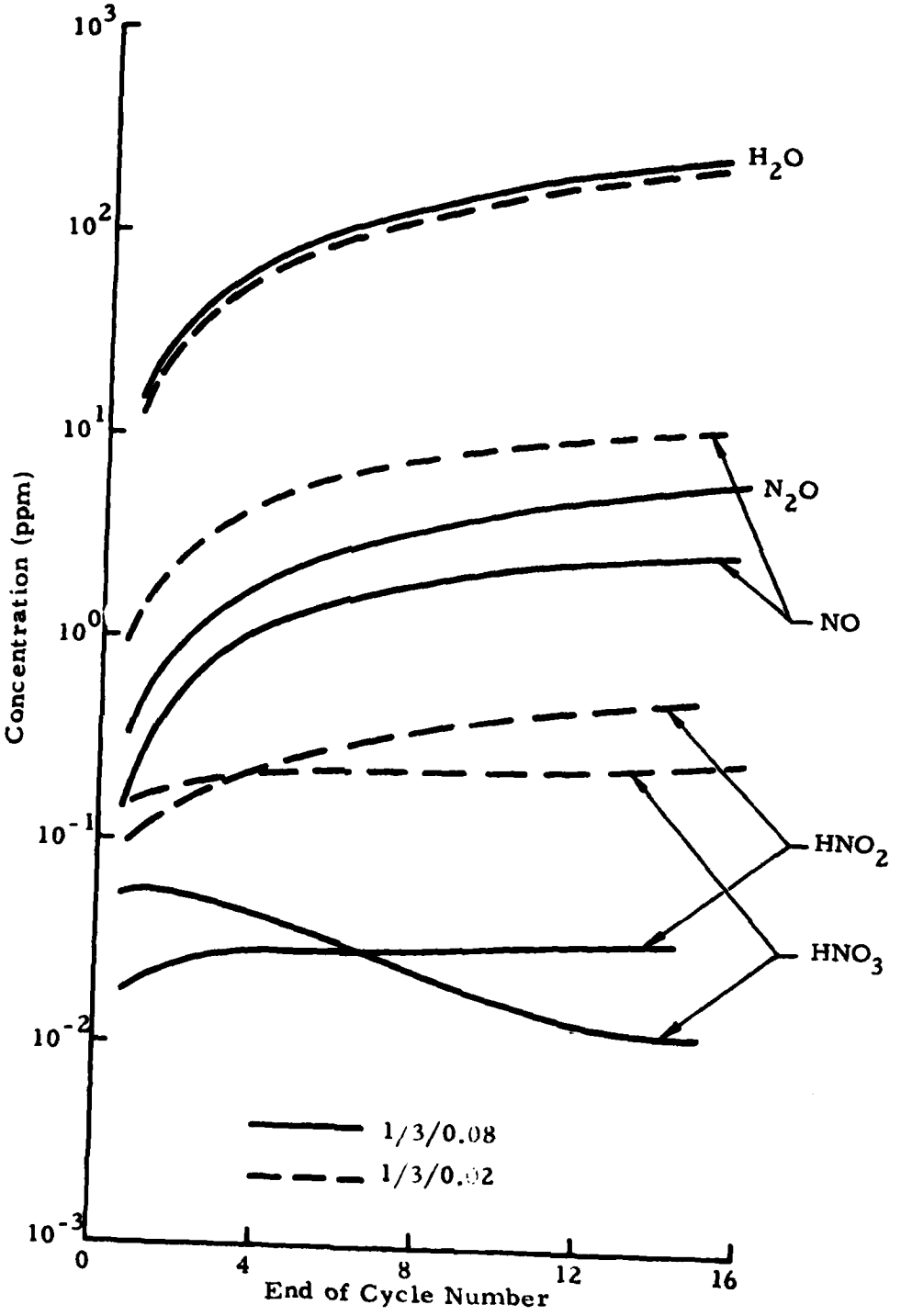

Fig. 57 - Contaminant Buildup During Closed Cycle Operation with Lasing (PULSAR)

decreased output power. It is interesting to note that build up of H_2O, N_2O and HNO_2 shows very little dependence on lasing in contrast to NO and HNO_3. For the case without lasing, shown in Fig. 58, the $CO_2/N_2/H_2$ = 1/3/0.08 mixture shows almost three times the amount of NO and about four times the amount of HNO_3 after 15 pulses as compared to the case with lasing (Fig. 57).

The foregoing results have been obtained without considering catalytic removal of contaminants nor have plasma chemistry effects in the cathode sheath been incorpoated. While it is now generally recognized that long term closed cycle operation may require the use of catalytic reactors in the cycle, the analysis presented here allows some quantitative observations to be made concerning this subject. As has been mentioned already, to extend the plasma chemistry calculations beyond 15 to 20 cycles becomes extremely expensive in terms of computer run time. We shall therefore try to arrive at an estimate of the long term behavior of the device.

Assuming again (see Section 3.2) an exponential decay of performance, we can determine a rate of decay for the laser output power as a function of cycle number. Using the curve for the 1/3/0.08 mixture shown in Fig. 55, this results in

$$E_{out} = 134.79\, e^{-1.19 \cdot 10^{-3} n} \qquad (35)$$

which gives an excellent fit for n = 5 to 15, n denoting the cycle number. Equation (35) yields a "half-life time" of 582 pulses with the usual meaning that after each 582 cycles the laser output power is reduced by 50%. This calculation does not consider a gas utilization factor, and is used only to illustrate the fact that without using a catalytic reactor to remove contaminants such as NO, N_2O, HNO_2 and HNO_3 it will be difficult, if not impossible, to maintain performance for any length of time.

Since catalytic reactors presently considered usually require relatively high temperatures to operate efficiently, the natural place for such a device

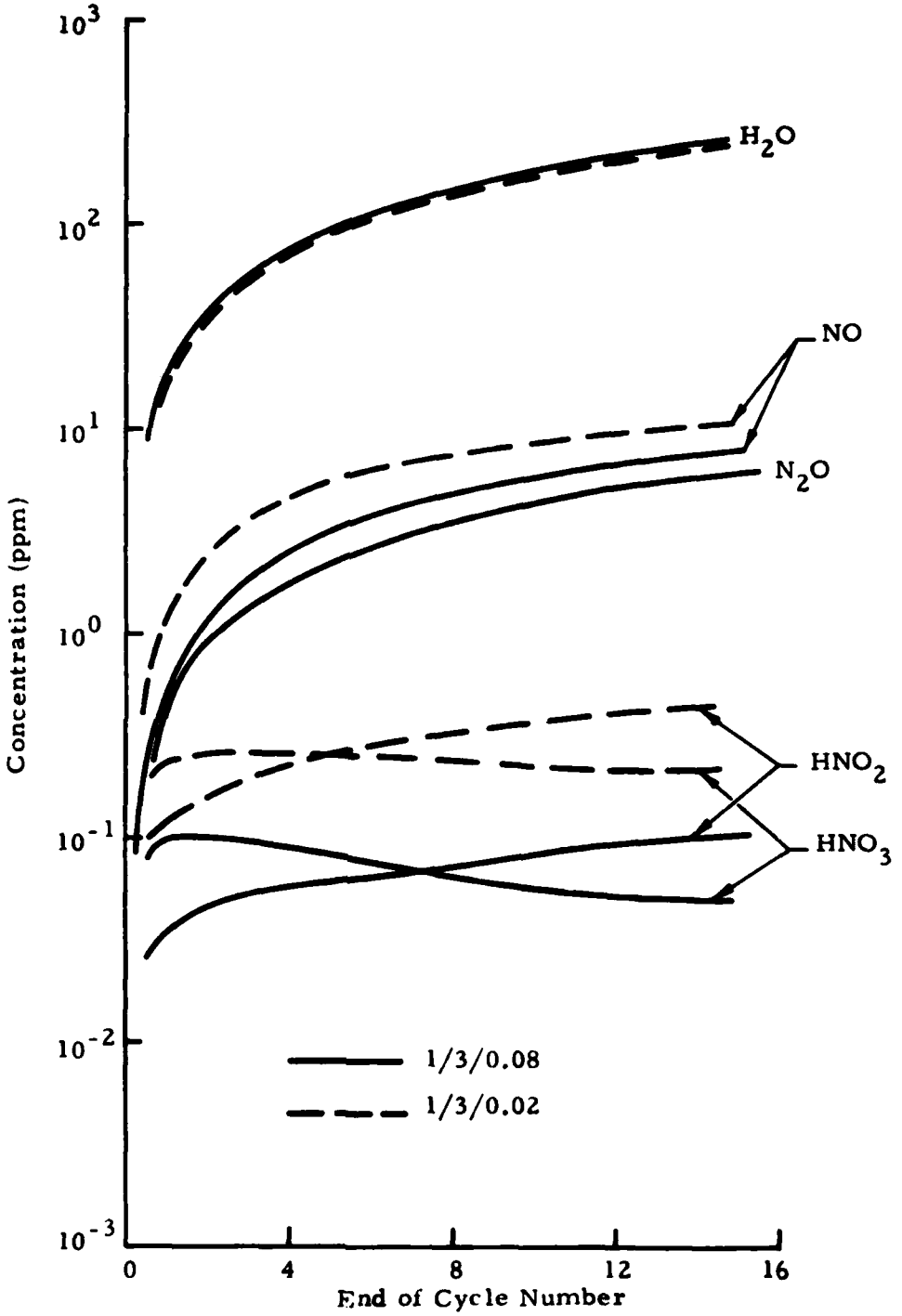

Fig. 58 - Contaminant Buildup During Closed Cycle Operation Without Lasing (PULSAR)

in the recirculation loop would be just downstream of the discharge where the gas reaches its highest temperature. Figure 59 shows temperature distributions around the cycle, with and without lasing, for 1/3/0.08 and 1/3/0.02 mixtures. Also indicated is the "temporal location" of the hot duct downstream of the cavity. Figure 60 shows some typical distributions of major contaminants, as a function of time around the cycle. Note that HNO_2 and HNO_3 are generally destroyed in the discharge and re-formed during the post-pulse relaxation period. NO, N_2O and H_2O maintain an almost constant distribution, whereas OH and NO_2 are mainly generated in the discharge, and then serve as principal reactants, in combination with available NO and H_2O, for the post-pulse regeneration of HNO_2 and HNO_3. This is the environment in which the catalytic reactor will have to function.

The analysis of, and predictions for, the PULSAR device will be concluded with an assessment of the production of electrophilic species in the cathode fall region. The $CO_2/N_2/H_2$ = 1/3/0.08 mixture without lasing will serve as an example (see Fig. 60). From Fig. 54 it is found that the discharge energy loading for this case is typically about 700 J/lit (1 pulse) which, using the given cavity geometry, translates into an average discharge current density of $\bar{j}_D = 5.4$ A/cm^2 during the pulse. Using a reduced pressure of 760 torr, we find that $\bar{j}_D/p_o^2 = 9.3 \cdot 10^{-6}$ (A cm^{-2} torr^{-2}). According to Fig. 1 this yields a cathode fall potential of V_c = 250 V, and $p_o\, d_c$ = 1.0 (cm torr), approximately. Therefore, we compute $d_c = 1.3 \cdot 10^{-3}$ cm, and $E_c = 1.92 \cdot 10^5$ V/cm. The bulk energy input into the cathode fall region therefore is $j_D \cdot E_c = 1.04 \cdot 10^6$ (W/cm^3). Using an approximate value of $k_o = 2.0 \cdot 10^{-4}$ (W/cm K), then Eq. (21) yields $T_c - T_o$ = 1460 K for the temperature rise in the cathode sheath. Assuming a cooled cathode wall temperature of about 300 K, the gas temperature in the sheath is found to be about 1760 K, corresponding to a pressure of about 8.8 atm at constant density. Because of the small volume of the cathode sheath the characteristic time for the relaxation of discharge generated pressure rise is much smaller than in the cavity. Equilibrium calculations were therefore performed at T = 1750 K for several pressures from 8.8 atm down to 1 atm initial cavity pressure. The results are shown in Fig. 61. From the resulting gas composition it is concluded that enough CO_2 is dissociated into CO and O to consume

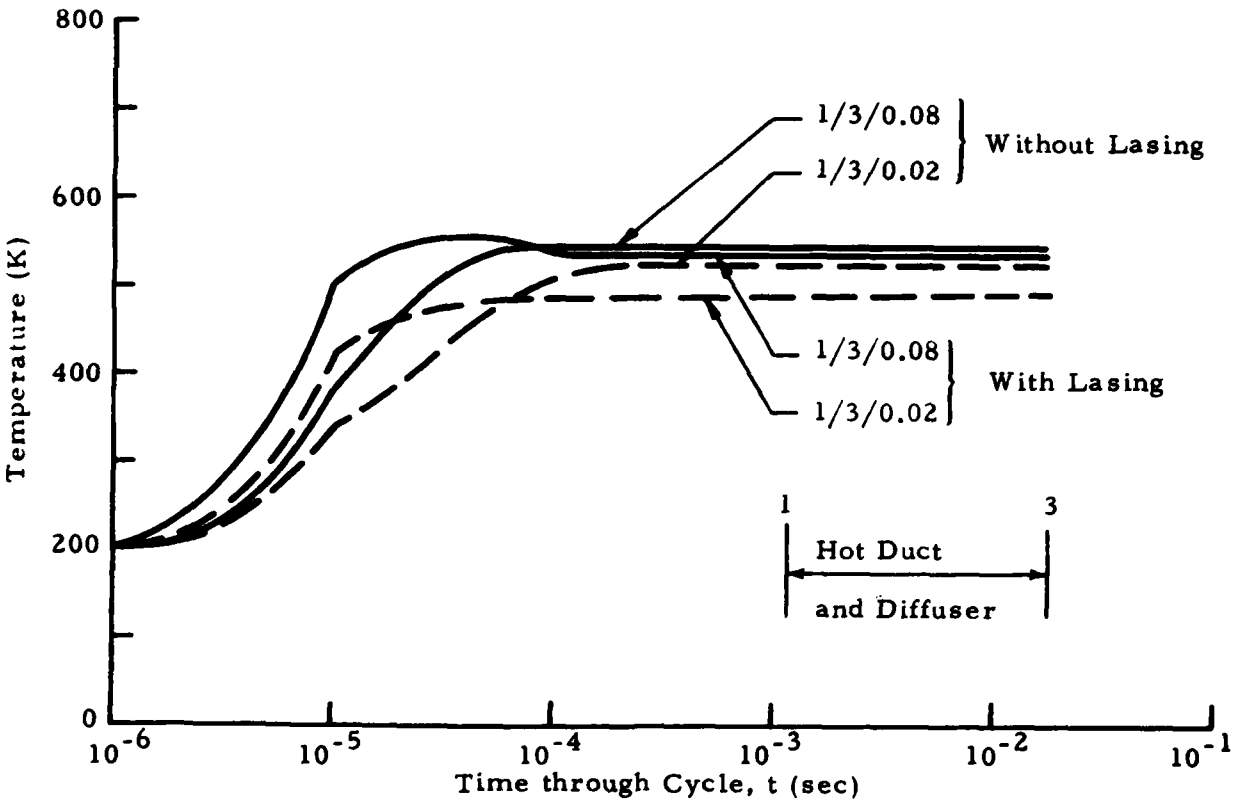

Fig. 59 - Effect of Hydrogen Concentration on Temperature Around Cycle With and Without Lasing (15th Pulse, PULSAR)

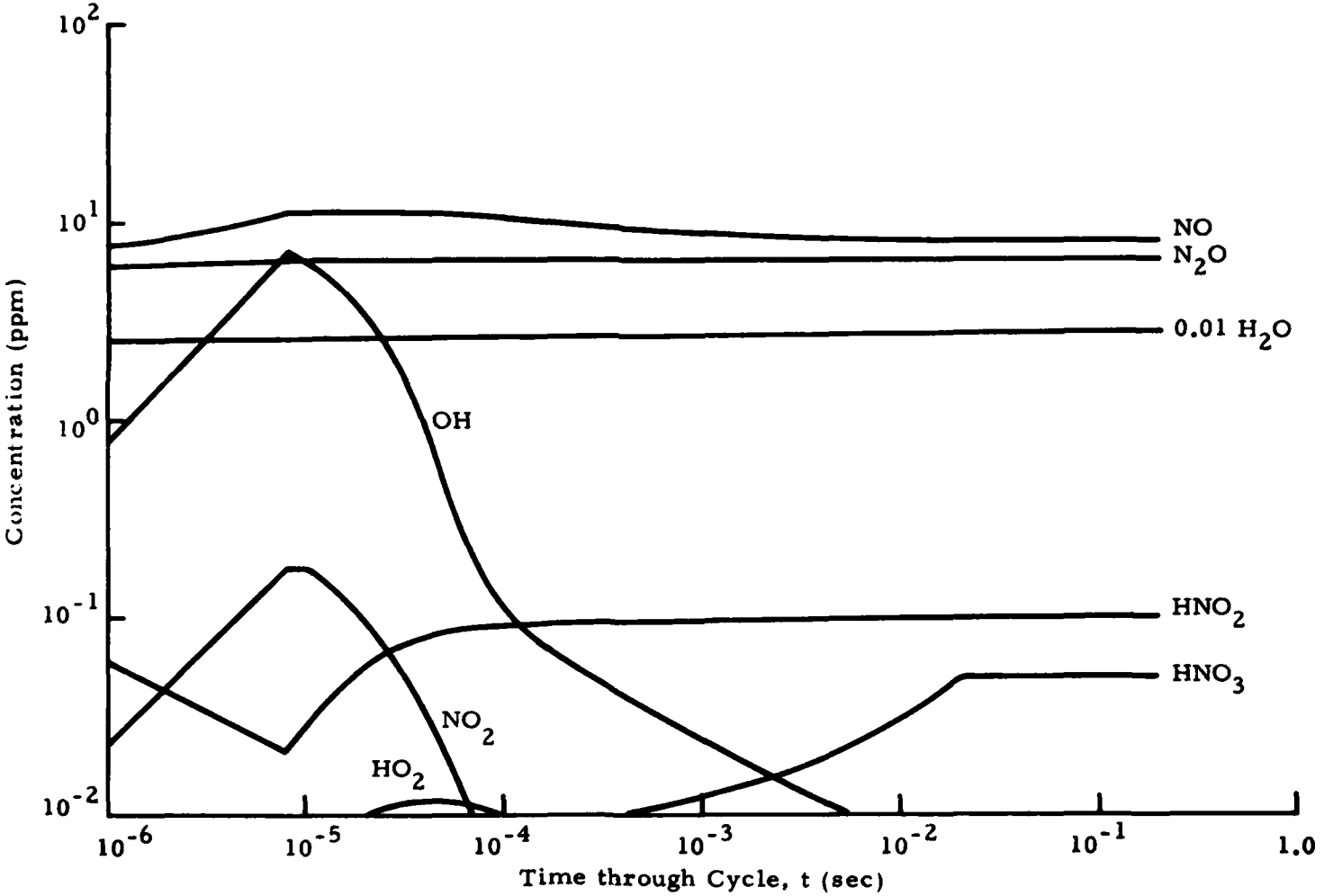

Fig. 60 - Contaminant Formation Around Cycle for $CO_2/N_2/H_2$ = 1/3/0.08 (PULSAR)
(15th Pulse, Without Lasing)

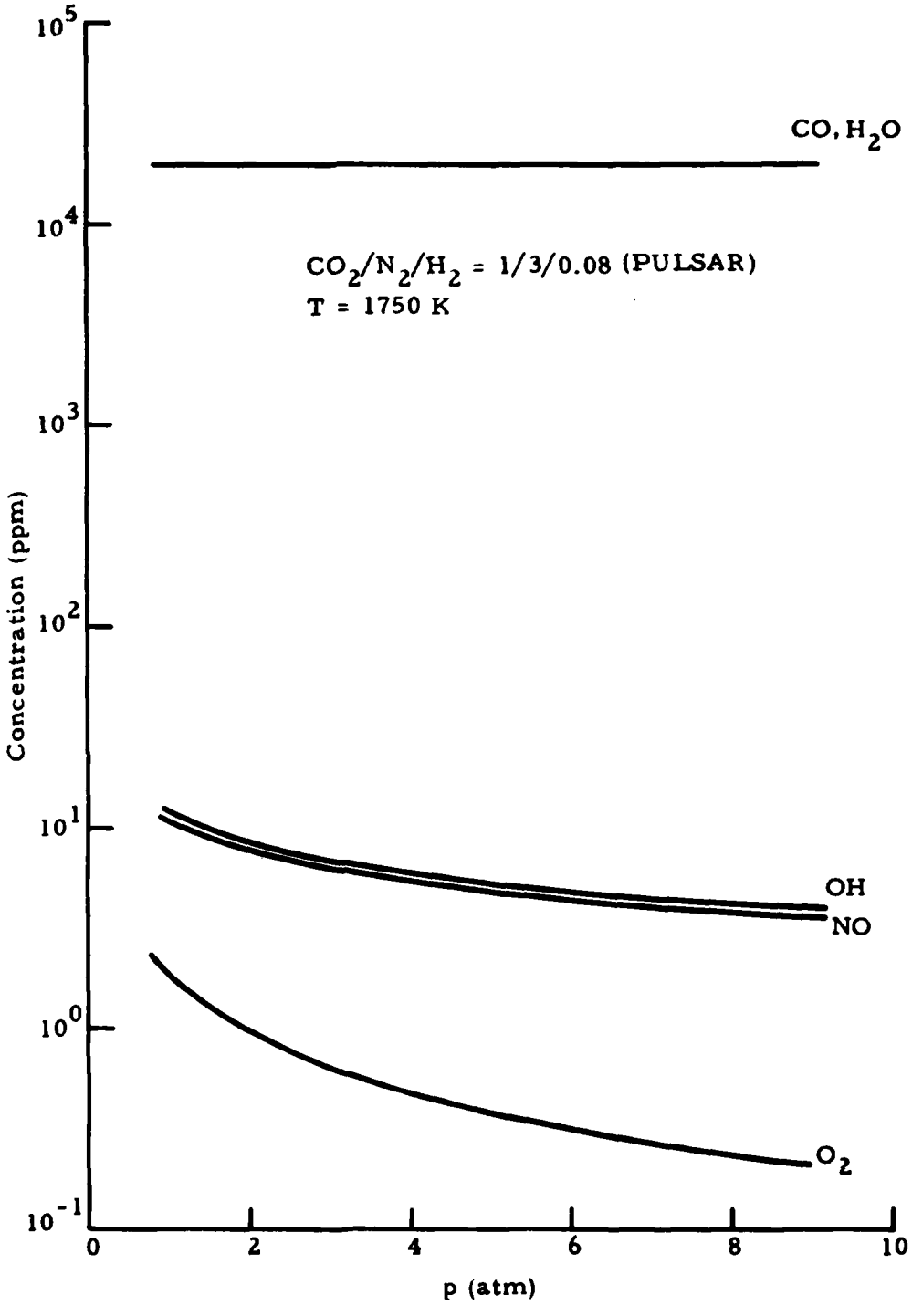

Fig. 61 - Contaminant Formation in Cathode Sheath (for Equilibrium at Assigned Temperature and Pressure)

almost all available H_2 in the formation of H_2O. While the H_2O population in the cathode fall is predicted to be about 2 orders of magnitude higher than in the positive column, populations of OH and NO are about the same as their respective peaks reached in the positive column at the end of the discharge (see Fig. 60). In contrast to the main discharge, populations of NO_2, HO_2 and N_2O do not even reach levels of 10^{-3} ppm. This is significant because in the absence of NO_2, OH and NO are the only principal reactants for the formation of HNO_2. Their populations being comparable to those in the positive column it is concluded that the cathode fall region should certainly not enhance the formation of HNO_2. Without significant amounts of NO_2, NO_3 nor HO_2 which are the principal reaction partners for OH, H_2O and NO, respectively, in the formation of HNO_3, the latter also has little chance of being generated from reactants formed in the cathode fall region under the given conditions. Finally, using Eqs. (25) and (26) it is found that when the H_2O generated in the cathode fall region is allowed to mix with that generated in the positive column, the overall increase in H_2O in the gas amounts to less than 1% under the given conditions.

4.2 ARMY CLOSED CYCLE GAS CIRCULATOR

The Army small scale closed cycle circulator concept is discussed in detail in Ref. 18 Its principal purpose is to furnish experimental data for the design and development of high energy closed cycle laser systems. Some of the main unanswered questions relate to the closed cycle gas stability, plasma formation, level pumping ability and shock wave attenuation ability. The problem dealt with in the present analysis is that of gas stability, particularly the problem of plasma by-product formation and resulting performance degradation.

Basic operating parameters for the small circulator are listed in Table 7. The first question that arises in setting up the analysis is that of the appropriate discharge potential. From the Boltzmann code results for the $CO_2/N_2/He$ = 1/2/3 mixture (see Fig. 6) we find that the discharge voltage should be set such that an E/N of about $2 \cdot 10^{-16}$ (Vcm^2) results which ensures optimum

Table 7

ARMY CLOSED CYCLE GAS CIRCULATOR OPERATING DATA*

Gas Composition	$CO_2/N_2/He = 1/2/3$
Flow Rate	140 to 640 g/sec
Cavity Pressure	760 torr
Cavity Inlet Temperature	200 K
E-Beam Energy	125 to 200 keV
Post-Foil E-Beam Current Density	1 to 100 mA/cm^2
Discharge Potential	10 to 50 kV
Discharge Energy	1000 J/lit (max)
Electrode Gap	5 cm
Cavity Volume	5 x 5 x 25 cm
Gain Length	25 cm
Pulse Width	
E-Beam	2 to 30 μsec
Discharge	1 to 30 μsec

*Data taken from Ref. 18.

upper laser level pumping. Hence, for given temperature and pressure, the desirable electric field is calculated to be approximately 7.4 kV/cm. Using the given electrode separation of 5 cm, the optimum discharge potential becomes 37 kV, which is well inside the range indicated in Table 7.

The next problem which must be addressed is the appropriate electron beam current density. Assuming an effective (post-foil) electron beam energy of 100 keV, and pulse widths of 8 μsec and 10 μsec for the electron beam and the discharge, respectively, the post-foil electron beam current density is limited by the discharge power which can be generated. The computed dependence of discharge energy loading on electron beam current density (for open cycle operation) is shown in Fig. 62, and shows that for a maximum energy loading of 1 kJ/lit, the electron beam current density should not exceed 40 mA/cm^2. For the analysis which follows we have selected a value of 30 mA/cm^2.

The application of our model to closed cycle kinetics calculations requires the gasdynamic conditions around the cycle to be known so that heat exchangers can be simulated appropriately. Unfortunately no such information is presently available for the small circulator. As we had to recognize previously, inaccurate circulator data can lead to very erroneous results (see Fig. 50). Therefore, in order to perform the analysis at least an approximate gasdynamic model had to be constructed which is summarized in Table 8. The table lists the main components and their location along the circulator as interpreted from Fig. 4 of Ref. 18. Approximate flow cross-sectional areas (denoted A) are listed also. The circulator contains three heat exchangers, the first two of which use water as coolant. Since the water is presumably stored at room temperature, we have assumed a gas exit temperature of 300 K for these heat exchangers. As the gas passes through the blower, its temperature is assumed to rise to approximately 350 K. Discharge energy input in the cavity was assumed to heat the gas to roughly 600 K, and the remaining values were fortunately known to be 200 K. Knowing the flow cross sections and the temperatures, one-dimensional continuity and the equation of state can

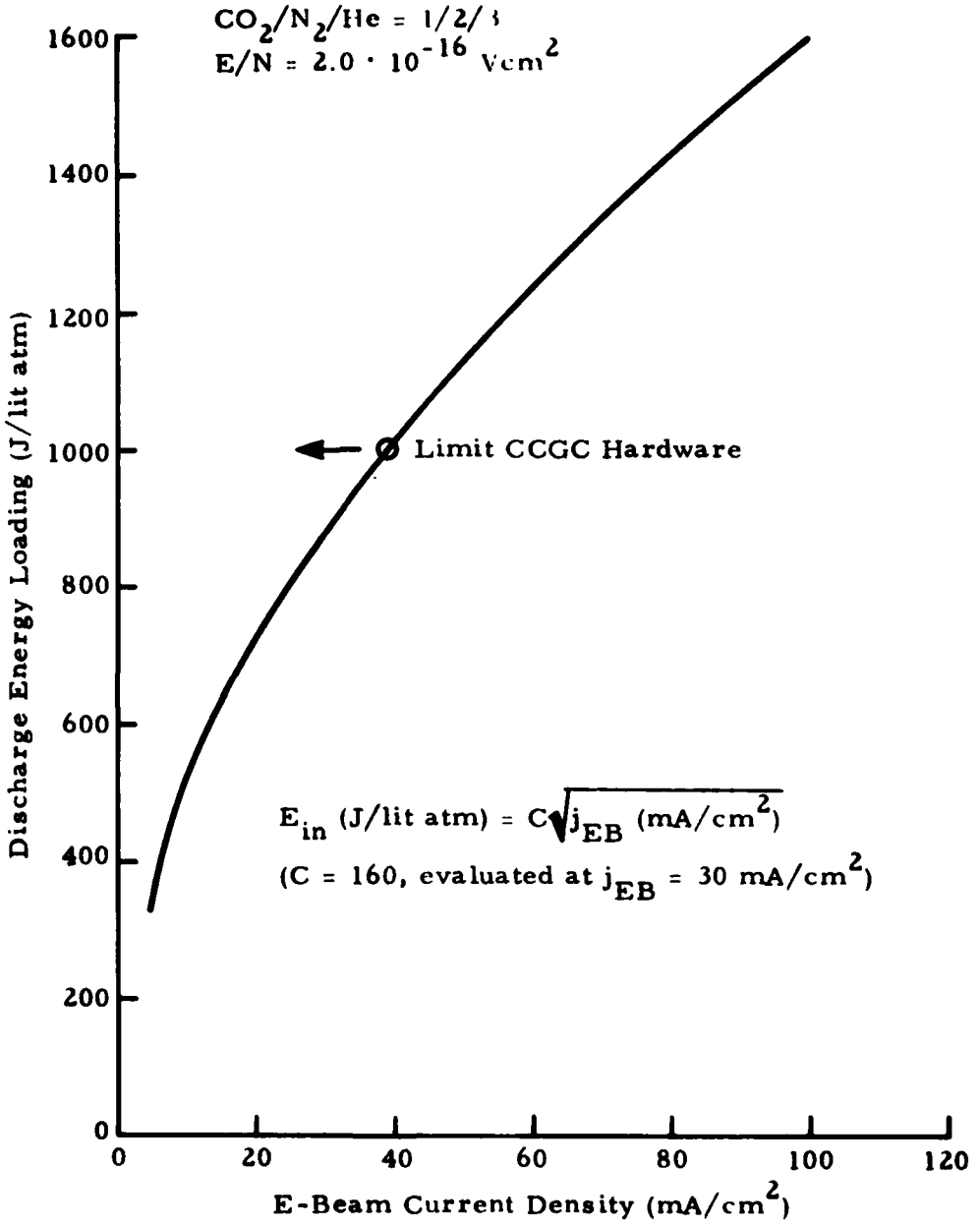

Fig. 62 - Discharge Energy Loading as a Function of Effective E-Beam Current Density (Open Cycle)

Table 8

ARMY CLOSED CYCLE GAS CIRCULATOR DATA*

	Station	X (cm)	A (cm^2)	T (K)	u (m/sec)	t (msec)
0	Cavity Entrance	0	125	200	31.6	0.0
1	Cavity Exit	8	125	600	94.6	1.4
2	Diffuser Exit	72	324	600	36.6	12.0
3	Duct Exit	160	324	600	36.6	36.0
4	Heat Exchanger 1	220	324	300	18.3	59.0
5	Blower Exit	290	324	350	21.4	94.0
6	Duct Exit	555	324	350	21.4	220.0
7	Heat Exchanger 2	630	324	300	18.3	260.0
8	Duct Exit	880	324	300	18.3	390.0
9	Heat Exchanger 3	975	324	200	12.2	460.0
10	Diffuser Exit	1115	390	200	10.1	580.0
0	Nozzle Exit	1190	125	200	31.6	620.0

*See discussion in text.

be used to arrive at an expression for the velocity in various sections of the circulator, i.e.,

$$u = \left(\frac{\dot{m} R}{p}\right) \frac{T}{A} \tag{36}$$

Velocities listed in Table 8 were calculated from Eq. (36) assuming a mass flow of $\dot{m}$ = 450 g/sec and a constant pressure of p = 760 torr. Finally, the last column of Table 8 lists the elapsed time as computed by integrating the reciprocal velocity distribution around the circulator. The temperature versus time history as needed in the plasma kinetics calculations is shown in Fig. 63. Note that the temperature up to the entrance of the first heat exchanger will actually be computed by the plasma kinetics code. Typical computed (first cycle) temperatures are shown in Fig. 64.

One of the questions raised with regard to closed cycle operation was the effect of water vapor in the laser gas on performance and contaminant formation. We have attempted to answer this question by comparing dry gas calculations with those assuming 10 ppm H_2O in the laser gas. Figure 65 shows a comparison of the discharge energy loading as a function of recirculation for the two cases. Note that while the dry gas shows a slight increase (about 5%) with recirculation before leveling off, the moisture contaminated gas shows a 12% decrease in energy loading for the first pulse, which then decreases further with recirculation. Corresponding first pulse discharge current density distributions are shown in Fig. 66. When averaged over the discharge pulse width of 10 μsec these current density distributions represent average discharge currents of 1478 and 1304 A, respectively.

It is surprising to see how little effect the differences in discharge energy loading have on the small signal gain distributions which are shown in Fig. 67. While the peak gain remains virtually the same (at 12% cm^{-1}) the only effect is a slight shift of the peak with time. It should be remembered, however, that the analysis of the PULSAR showed the same phenomenon. While for that device small signal gain distributions were almost identical (see Fig. 46),

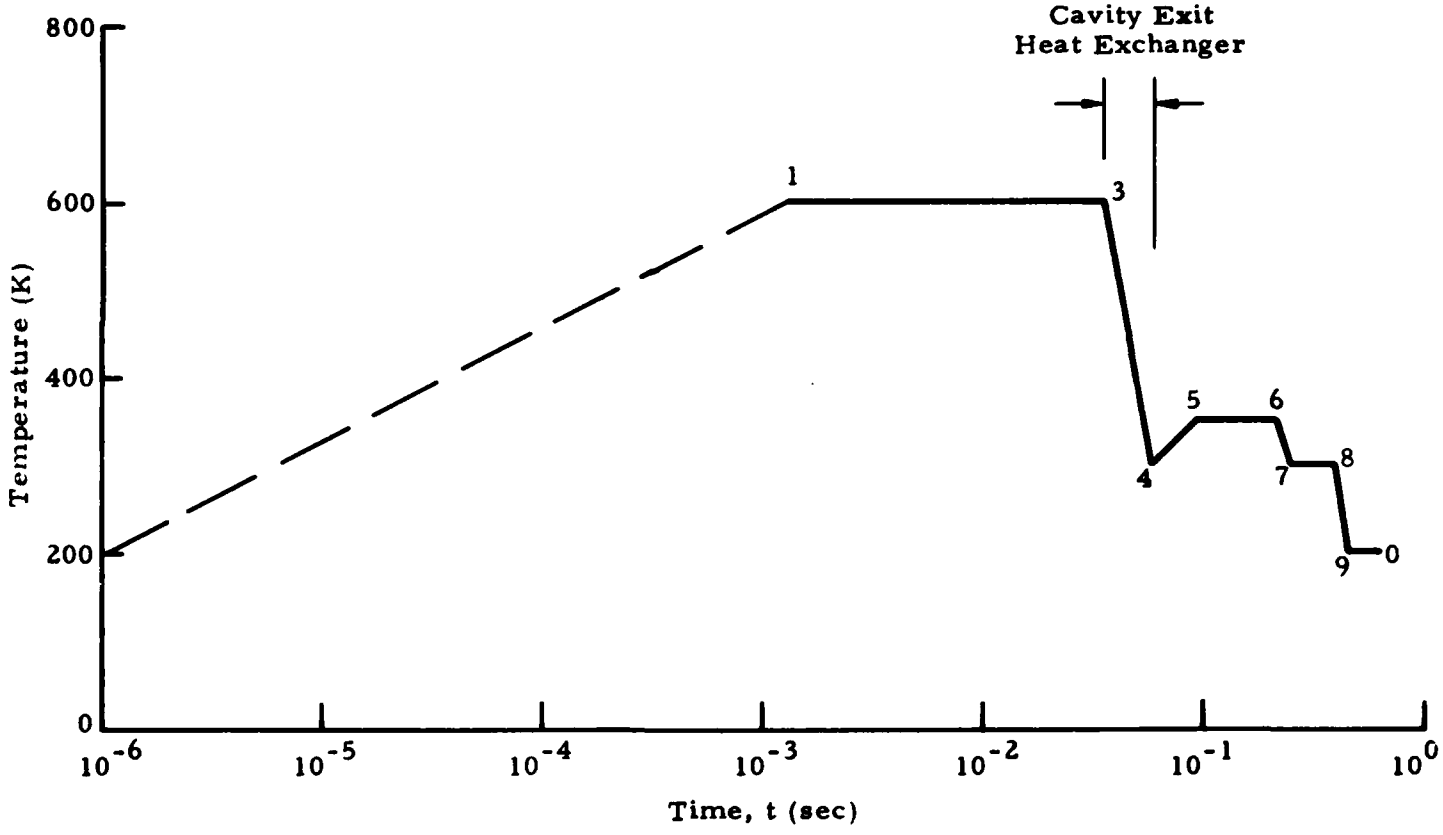

Fig. 63 - Temperature Distribution Around Circulator as a Function of Time

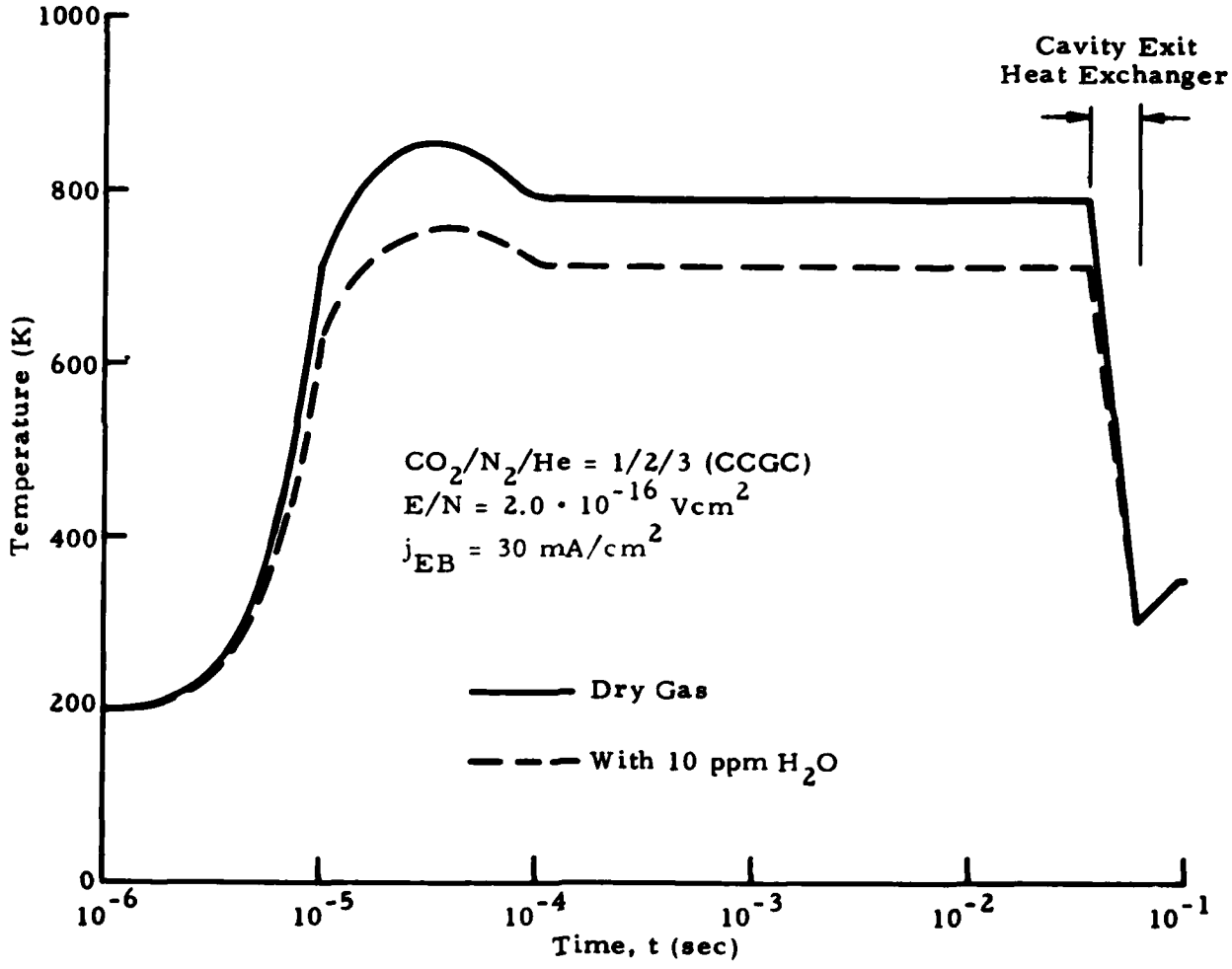

Fig. 64 - Effect of Moisture (10 ppm H_2O) on Temperature During Discharge Pulse and Post-Pulse Expansion

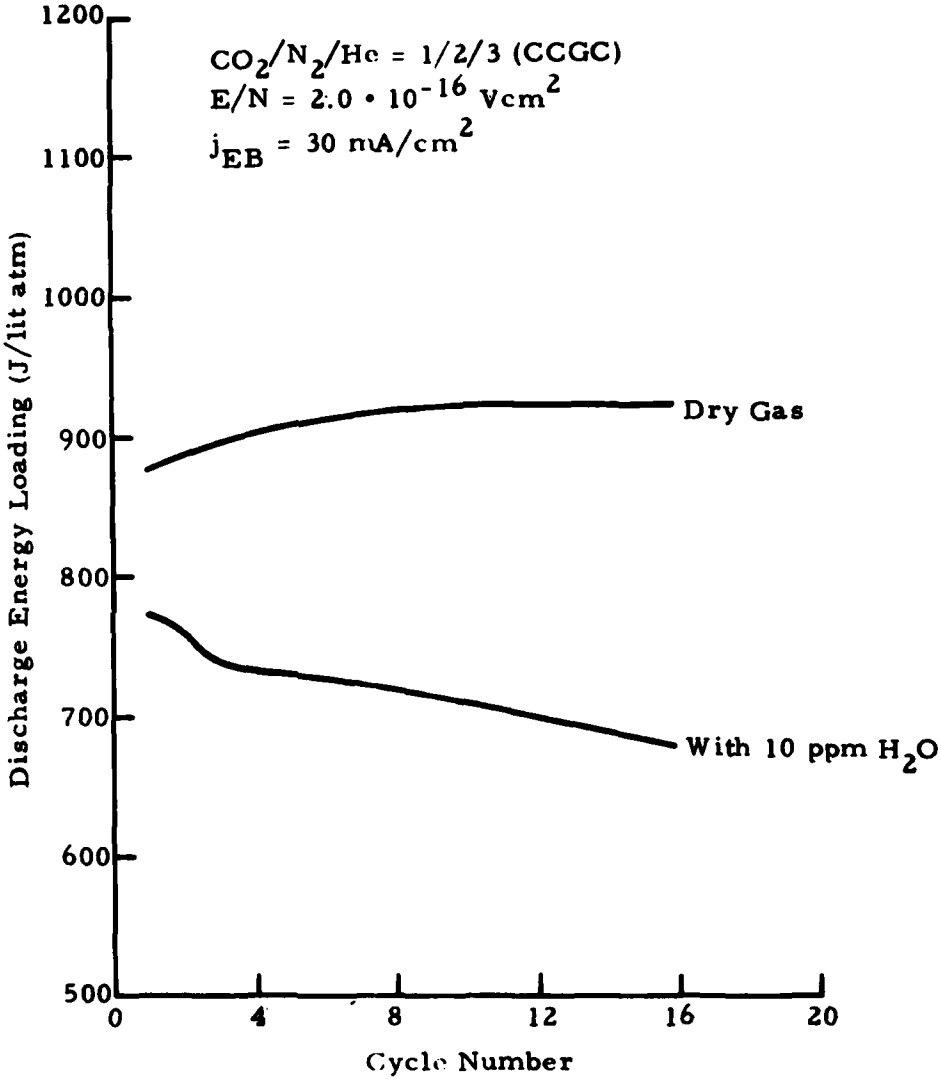

Fig. 65 - Discharge Energy Loading as a Function of Recirculation and H_2O Contamination

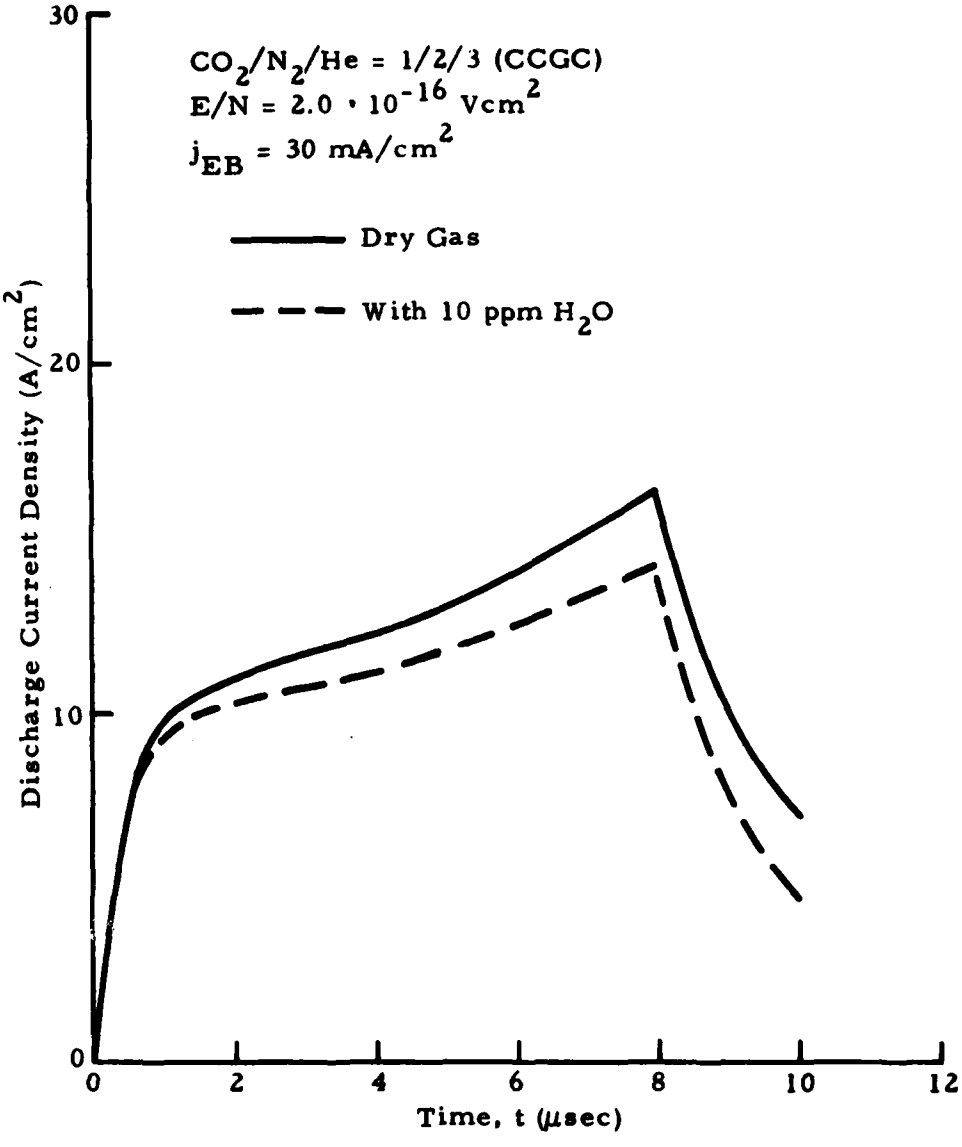

Fig. 66 - Effect of Moisture on First Pulse Discharge Current Density

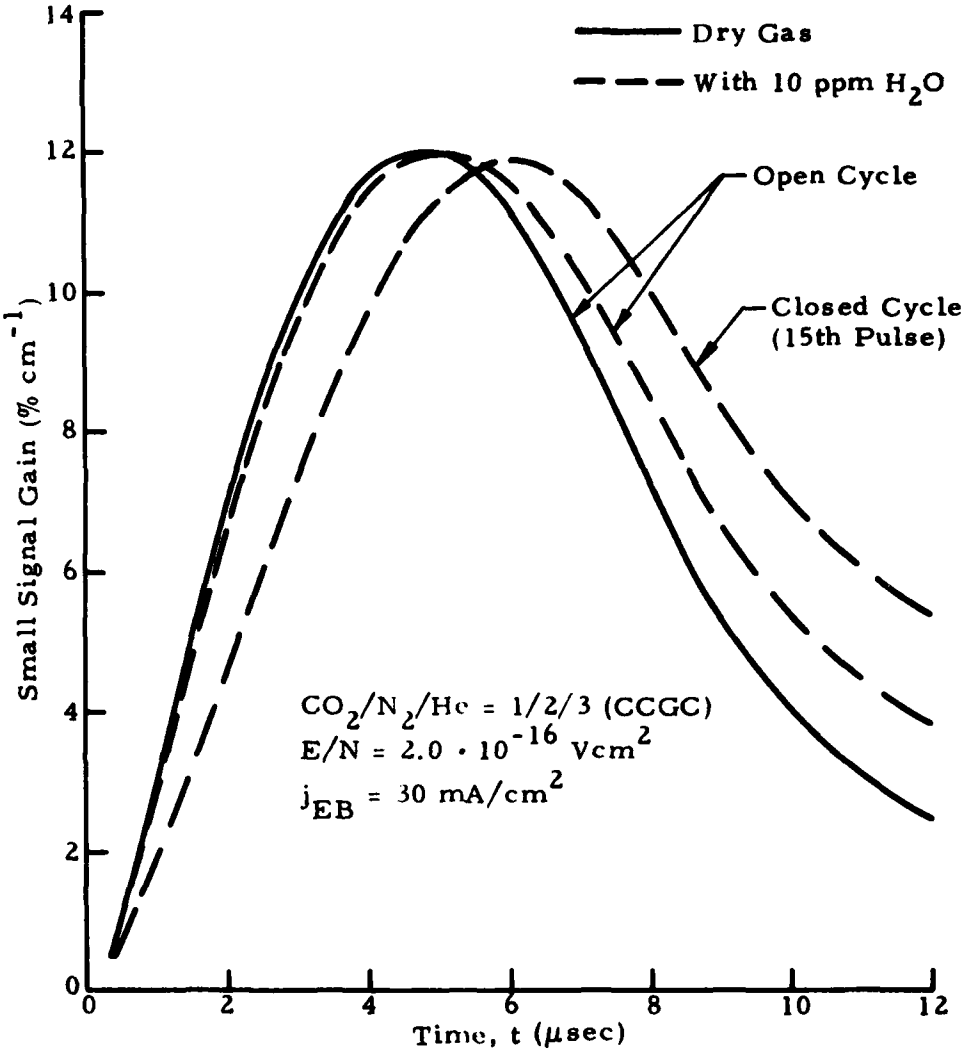

Fig. 67 - P(16) Small Signal Gain Distribution as a Function of Time During Pulse

the corresponding pulse output energies differed substantially (see Fig. 55). It must be concluded that small signal gain distributions by themselves are not necessarily good indicators for the performance of a device.

The decrease in discharge energy loading due to moisture in the gas can be explained by examining by-product concentrations in the gas as a function of recirculation. In a gas with no trace of hydrogen, the various oxides of nitrogen really have no major effect as long as only small quantities are created. Figure 68 shows concentrations of CO, O_2 and O_3, as well as of NO, NO_2 and N_2O as they develop during recirculation of a perfectly clean $CO_2/N_2/He$ = 1/2/3 mixture. These concentrations should be compared to those shown in Fig. 69 which result when the gas is moisture contaminated. The most noticeable difference is that, for the moist gas, the resulting NO_2 concentration is roughly an order of magnitude lower than that for the dry gas. Except for O_3, which for the moist gas shows not only a much lower concentration but also a reversal in trend, the other species do not show any drastic change.

The principal reason for the decrease of the NO_2 *concentration is that* NO_2 reacts with H_2O to form HNO_2 and OH. NO_2 further reacts with OH to form HNO_3 while NO combines with the remaining OH radicals to generate more HNO_2. Figure 70 shows that roughly 90% of the available H_2O is dissociated to form H_2. The remaining 10% (1 ppm in this case), however, is sufficient to combine with the available 1 ppm NO_2 (in the dry gas) to start the chain reaction of forming HNO_2 and HNO_3. Under these conditions, ignoring the NO for the moment, we would expect to see roughly 1 ppm of HNO_2/HNO_3 combined being created. Figure 70 shows that this is precisely the case. We also conclude that formation of HO_2NO_2 plays only a very minor role. It is generated mainly from HO_2 and N_2O_5 both of which are present only in negligible amounts under the present conditions.

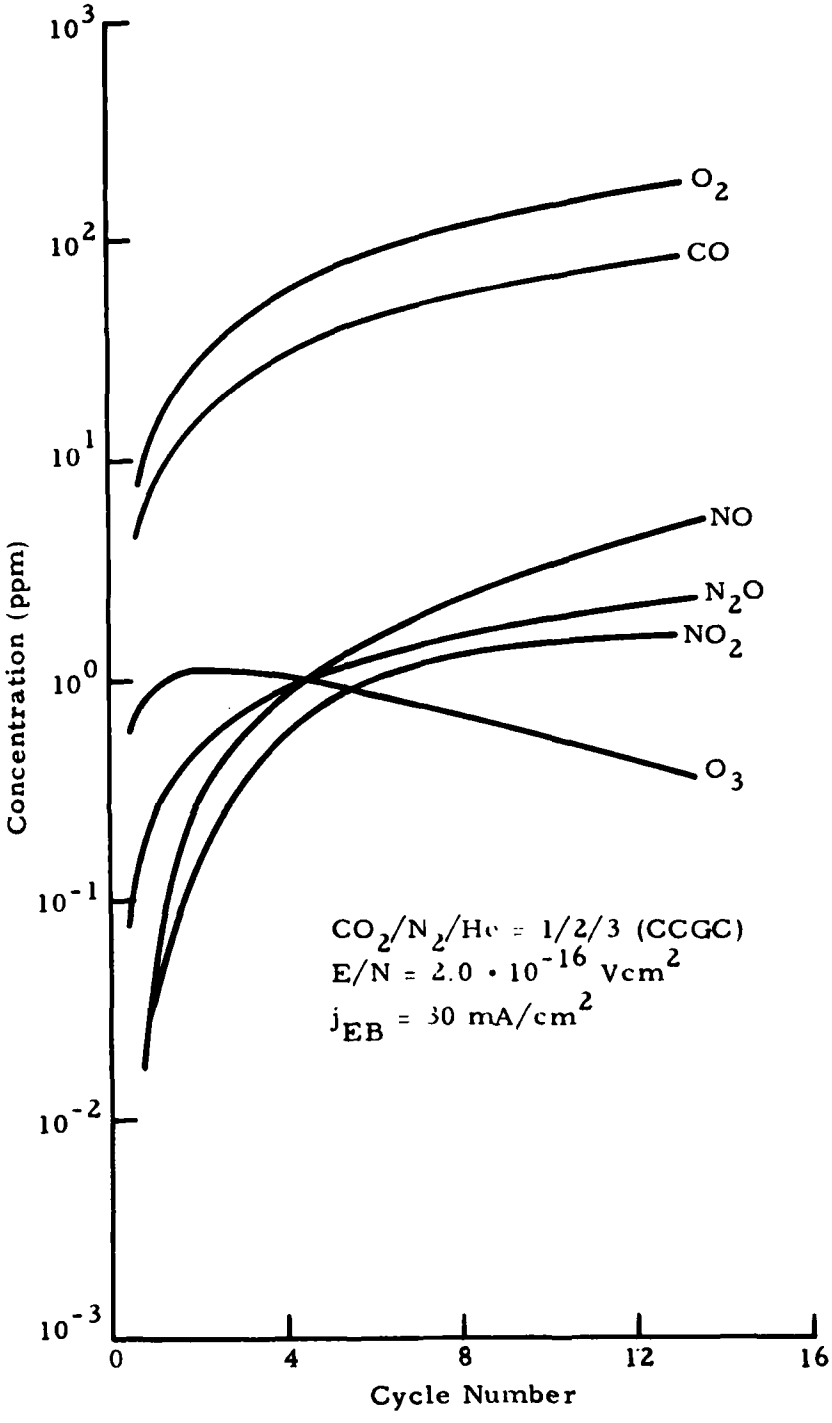

Fig. 68 - Dry Gas Contaminant Generation During Closed Cycle Operation (Without Lasing)

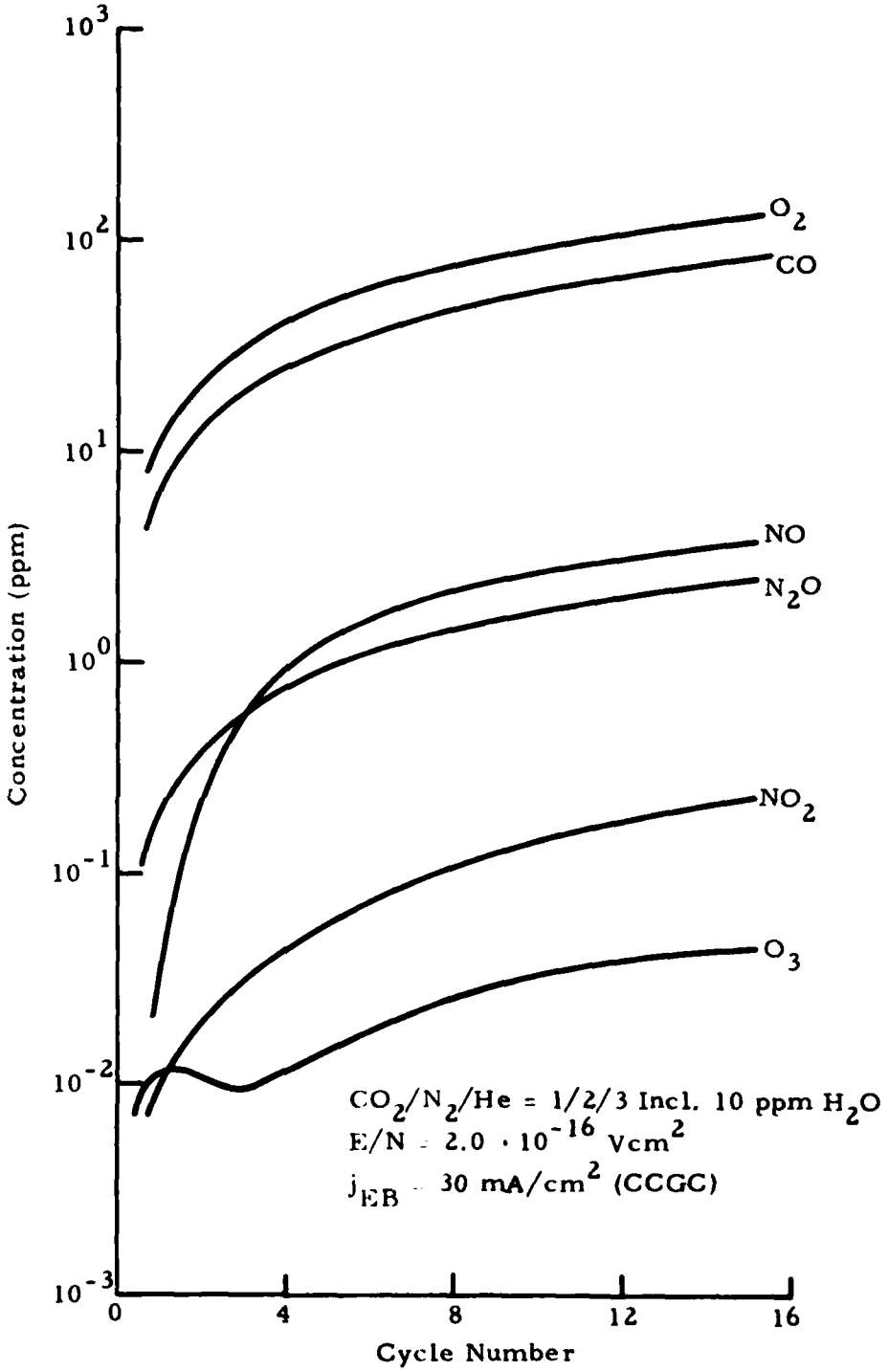

Fig. 69 - Moist Gas Contaminant Generation During Closed Cycle Operation (Without Lasing)

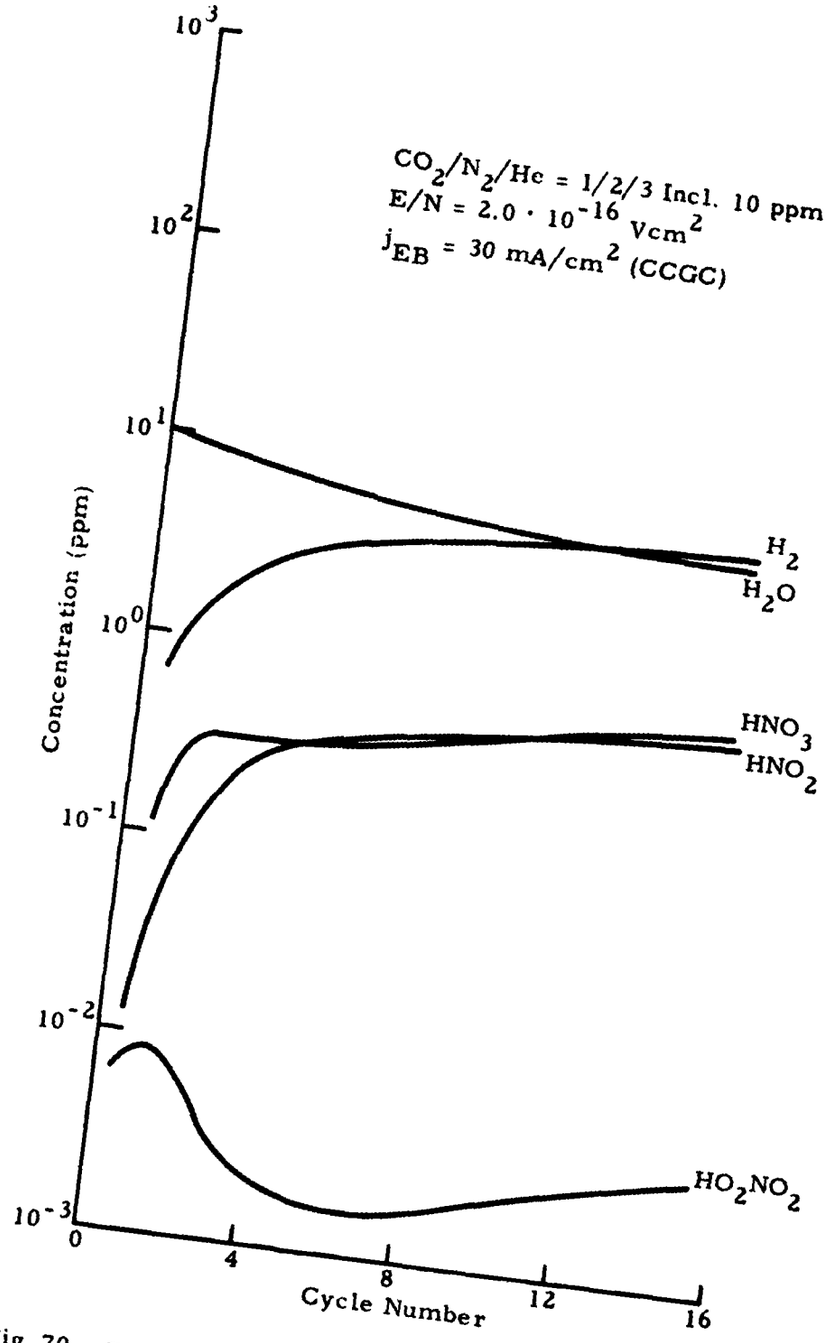

Fig. 70 - Electrophilic Contaminants Generation in Moist Gas During Closed Cycle Operation (Without Lasing)

5. CONCLUSIONS AND RECOMMENDATIONS

The overall objective of the effort described in this report, namely, to extend the existing EDLAMP computer program to account for the electron energy distribution in the plasma chemistry analysis of closed cycle EDL systems, and to evaluate specific operational gas mixtures has been accomplished. The coupling of a Boltzmann code into the analysis via generalized curve fits of the drift field velocity and the various electron impact excitation rates has added substantially to the usefulness of the code in analyzing CO_2 electric discharge lasers using gas mixtures consisting of CO_2, N_2, He, CO and O_2 in arbitrary proportions. Implementation of several other refinements such as a revised model of electron-beam ionization, preparation of a set of updated general reaction mechanisms and rates, and incorporation of at least a simple model to assess the effect of cathode sheath conditions on the plasma chemistry in the discharge have further improved the model as an analytical tool. The improved model has been tested by comparing our predictions with supplied experimental results in one case, and by comparison of our analytical results with those of others in another case. The good agreement achieved lends credibility to our theoretical model and its application to the analysis of closed cycle EDL systems.

A detailed analysis has been presented for two closed cycle EDL devices which are presently under development. For the PULSAR device, which uses a $CO_2/N_2/H_2 = 1/3/0.08$ gas mixture, the effects of variations in discharge voltage, electron-beam current and H_2 concentration on laser pulse energy has been investigated. Variations in the first two parameters basically served to define optimum operating conditions subject to hardware constraints (maximum discharge energy loading). Variations in H_2 content were studied with the aim of minimizing gas contamination under closed cycle operation. It was found that decreasing the H_2 concentration actually increases the concentrations of electrophilic species formed (such as HNO_2 and HNO_3)

which results in decreased output pulse energy as well as a stronger rate of decay under closed cycle operation. From an assessment of the conditions in the cathode sheath for this device it is concluded at this time that the cathode fall region should not significantly contribute to the contamination problem.

Analysis of the Army circulator device centered around studying the effect of contamination of the $CO_2/N_2/He = 1/2/3$ gas mixture by water vapor on closed cycle discharge energy loading and small signal gain. While the effect on small signal gain was found to be negligible, the discharge energy loading decreased noticeably due to the formation of HNO_2 and HNO_3.

A series of calculations was also performed to study the effect of contaminant removal via catalytic reactor. This was done for the $CO_2/CO/N_2/He = 1/0.25/5.5/0.125$ gas mixture in the Army closed cycle circulator, assuming a very simplified temperature history around the cycle. These calculations were completed before the importance of an accurate temperature history was recognized during the analysis of the PULSAR device. Since the results must therefore now be considered in error these calculations have not been documented here. Unfortunately time did not permit repeat of this analysis during the present effort. A preliminary conclusion reached from analyzing various discharge conditions for a variety of gas mixtures is that the selection of discharge voltage and electron-beam current density such that optimum efficiency is achieved for the given maximum discharge energy loading may be one of the best ways to minimize the closed cycle discharge generated contaminant problem.

The comparison of the code results with experimental data and its application to analyzing test cases has brought several specific deficiencies to light which should be remedied in a future effort.

1. While we do not know the reason for the slight discrepancies between our analytical and Freed's experimental results, it may be possible to improve the agreement by further refinement of the kinetics model. As new kinetics information appears in the literature, it must be extracted, evaluated and implemented. This requires an almost continual effort to keep abreast of the latest developments in kinetics research.

2. Whereas our model computes small signal gain values in good agreement with experiment for low discharge energy loading (Freed's case, about 0.1 kJ/lit atm), predicted small signal gain for high energy loading (ABEL, about 0.8 kJ/lit atm) are judged too high although the output power appears to be approximately correct. A possible reason for this behavior of the model may be the truncation of CO_2 vibrational levels above the $CO_2(001)$ level. This simplification may not be valid for high energy loading situations accompanied by comparatively higher gas temperatures leading to non-negligible populations of the ignored higher energy levels. Further analysis of high energy loading cases and comparison with reliable small signal gain measurements should be undertaken to resolve this question.

3. Regarding the EDLAMP code and its capability to predict closed cycle performance the most pressing need is a revision of the catalytic reactor model option. Provision should be made to "scrub" certain species not at the end of the cycle (as presently done) but somewhere between cavity exit and the first heat exchanger because of the high temperature requirements for efficient catalyst operation. Furthermore, contaminant removal efficiency should be redefined to reflect actual catalyst capability to remove certain species down to, for example, one part per million concentration.

4. An effort should be undertaken to incorporate a cathode sheath model in the EDLAMP code in a more rigorous fashion than what was possible under the present effort.

5. Further analysis of test cases should include the effect of variations in resonator output coupling on closed cycle laser performance (results presented here have arbitrarily assumed an output coupling of 50%), as well as other combinations of discharge voltage and electron-beam current density (for given maximum discharge energy loading).

6. Closed cycle laser output performance predictions should be compared with experimental results as these become available. Of particular interest is the validation of predicted decay rates, with and without catalytic removal of key contaminant species.

The last recommendation made is, of course, intimately related to electrophilic plasma byproduct generation. One of the key experiments that can thus be suggested should be the measurement of NO, N_2O, HNO_2, HNO_3 and H_2O concentrations. The analysis has shown that these measurements should be taken somewhere just upstream of the cavity entrance. Measurements of OH and NO_2 concentrations, if possible, should be attempted in the cavity just after the discharge pulse has terminated.

REFERENCES

1. Hill, Alan E., "Uniform Electrical Excitation of Large-Volume High-Pressure Near-Sonic CO_2-N_2-He Flowstream," Appl. Phys. Let., Vol. 18, No. J, March 1971, p. 194.
2. Bletzinger, Peter, David A. LaBorde, William Bailey, William H. Long, Jr., Peter T. Tannen, and Alan Garscadden, "Influence of Contaminants on the CO_2 Electric Discharge Laser," IEE J. Q. E., Vol. QE-11, No. 7, July 1975. p. 317
3. Thoenes, Jürgen and Shelby C. Kurzius, "Plasma Chemistry Processes in Pulsed Electric Discharge Lasers," MICOM Technical Report RH-CR-76-12, Redstone Arsenal, Ala., August 1976.
4. Culick, F. E. C., P. I. Shen and W. S. Griffin, "Acoustic Waves and Heating Due to Molecular Energy Transfer in an Electric Discharge CO Laser," IEEE J. Quantum Electronics, QE-12, No. 10, October 1976, p. 566.
5. Long, W. H., "Plasma Sheath Processes," Quarterly R&D Status Report, Nos. 4 and 5, May-October 1978, Contract F33615-77-C-2048, Northrop Research and Technology Center.
6. Gordon, S., and B. J. McBride, "Computer Program for Calculation of Complex Chemical Equilibrium Compositions, Rocket Performance, Incident and Reflected Shocks and Chapman-Jouguet Detonations," NASA SP-273, NASA-Lewis Research Center, Cleveland, Ohio, 1971.
7. Berger, M. J., and S. M. Seltzer, "Tables of Energy Losses and Ranges of Electrons and Positrons," NASA SP-3012, 1964.
8. Schlie, LaVerne A., "Numerical Solution of Boltzmann Transport Equation," Unpublished Manuscript, Air Force Weapons Laboratory, Kirtland AFB, N. M.
9. Nighan, William L., "Electron Energy Distributions and Collision Rates in Electrically Excited N_2, CO, and CO_2," Physical Review A, Vol. 2, No. 5, November 1970, p. 1989.
10. "JDH Boltzmann Code," No documentation available.
11. Lowke, J. J., A. V. Phelps, and B. W. Irwin, J. Appl. Phys., Vol. 44, 1973, p. 4664.
12. Elliot, C. J., O. P. Judd, A. M. Locket and S. D. Rockwood, "Electron Transport Coefficients and Vibrational Excitation Rates for Electrically Excited CO_2 Gas Lasers," Los Alamos Scientific Laboratory, Research Report No. LA-5562 MS, 1973 (unpublished).

13. Thoenes, Jürgen, Shelby C. Kurzius and Marcus L. Pearson, "EDL Performance Model, Part I, Theory and User's Guide," MICOM Technical Report RG-CR-75-2, Redstone Arsenal, Ala., June 1975.

14. Thoenes, Jürgen and Shelby C. Kurzius, "EDL Performance Model, Part III, Analysis of Closed Cycle Electron-Beam Sustained CO_2 EDL with Air Contaminant," MICOM Technical Report RG-CR-75-2, Redstone Arsenal, Ala., May 1976.

15. Freed, Charles, MIT Lincoln Laboratories; Personal Communication.

16. Roberts, T.G., Army High Energy Laser Laboratory; Personal Communication.

17. Filcoff, John, Air Force Weapons Laboratory, Electric Laser Branch; Personal Communication.

18. Cason, Charles, "A Small Scale Closed Cycle Circulator Experimental Plan for Repetitively Pulsed 200 K High Pressure Electric Discharge Lasers," MICOM Technical Report RH-76-12, Redstone Arsenal, 2 August 1976.

Appendix
REACTION RATE COEFFICIENTS

A	Ionization Reactions
B	Attachment Reactions
C	Detachment Reactions
D	Ion-Electron Recombination Reactions
E	Ion-Ion Recombination Reactions
F	Charge Exchange Reactions
G	Electron Impact Excitation Reactions
H	Vibrational Relaxation Reactions
J	Ternary Recombination Reactions
K	Binary Reactions

	Reaction		Rate Coefficient	Ref.
A1	$CO_2(000) + e_{EB} \longrightarrow CO_2^+ + e + e_{EB}$		$2.9(-7)\ E_{EB}^{-0.23}$	1
A2	$CO_2(010) + e_{EB} \longrightarrow CO_2^+ + e + e_{EB}$		$2.9(-7)\ E_{EB}^{-0.23}$	1
A3	$CO_2(000) + e_{EB} \longrightarrow CO_2^{*+} + e + e_{EB}$		$7.0(-8)\ E_{EB}^{-0.23}$	1
A4	$CO_2(010) + e_{EB} \longrightarrow CO_2^{*+} + e + e_{EB}$		$7.0(-8)\ E_{EB}^{-0.23}$	1
A5	$CO_2(000) + e_{EB} \longrightarrow CO(0) + O + e_{EB}$		$1.6(-9)\ E_{EB}^{-0.23}$	2
A6	$CO_2(000) + e_{EB} \longrightarrow CO_2^* + e_{EB}$		$5.7(-7)\ E_{EB}^{-0.23}$	3
A7	$He + e_{EB} \longrightarrow He^+ + e + e_{EB}$		$2.5(-8)\ E_{EB}^{-0.23}$	1
A8	$CO(0) + e_{EB} \longrightarrow CO^+ + e + e_{EB}$		$1.9(-7)\ E_{EB}^{-0.23}$	1
A9	$CO(0) + e_{EB} \longrightarrow CO^* + e + e_{EB}$		$4.0(-8)\ E_{EB}^{-0.23}$	1
A10	$CO(0) + e_{EB} \longrightarrow CO^* + e_{EB}$		$4.0(-7)\ E_{EB}^{-0.23}$	4
A11	$N_2(0) + e_{EB} \longrightarrow N_2^+ + e + e_{EB}$		$1.9(-7)\ E_{EB}^{-0.23}$	1
A12	$N_2(1) + e_{EB} \longrightarrow N_2^+ + e + e_{EB}$		$1.9(-7)\ E_{EB}^{-0.23}$	1
A13	$N_2(0) + e_{EB} \longrightarrow N_2^{*+} + e + e_{EB}$		$4.0(-8)\ E_{EB}^{-0.23}$	1
A14	$N_2(1) + e_{EB} \longrightarrow N_2^{*+} + e + e_{EB}$		$4.0(-8)\ E_{EB}^{-0.23}$	1
A15	$N_2(0) + e_{EB} \longrightarrow N + N + e_{EB}$		$3.1(-9)\ E_{EB}^{-0.23}$	5
A16	$N_2(0) + e_{EB} \longrightarrow N_2^* + e_{EB}$		$3.7(-7)\ E_{EB}^{-0.23}$	4
A17	$O_2 + e_{EB} \longrightarrow O_2^+ + e + e_{EB}$		$1.9(-7)\ E_{EB}^{-0.23}$	1
A18	$O_2 + e_{EB} \longrightarrow O_2^{*+} + e + e_{EB}$		$7.0(-8)\ E_{EB}^{-0.23}$	1
A19	$O_2 + e_{EB} \longrightarrow O + O + e_{EB}$		$1.9(-9)\ E_{EB}^{-0.23}$	6
A20	$CO_2(000) + e \longrightarrow CO_2^+ + e + e$		$5.0(-9)\ u_e^{-2.3} \exp(-13.5/u_e)$	7
A21	$CO(0) + e \longrightarrow CO^+ + e + e$		$1.3(-10)\ u_e^{-0.42} \exp(-14.0/u_e)$	8

NOTE: Reactions A1 through A19 are of type 14 or 15 (see Vol. II, EDLAMP User's Manual). For program use, only the constant factor of the rate coefficient is read (the factor $E_{EB}^{-0.23}$ is coded into the program).

	Reaction	Rate Coefficient	Ref.
B1	$O + e + M1 \longrightarrow O^- + M1$	$1.0(-31)$	
B2	$O_2 + e + M1 \longrightarrow O_2^- + M1$	$1.5(-29)\,T^{-1.0}$	9, 104
B3	$O_2 + e + M5 \longrightarrow O_2^- + M5$	$4.2(-27)\,T^{-1.0}\exp(-1200/RT)$	9
B4	$CO_2(000) + e \longrightarrow O^- + CO(0)$	$\dfrac{3.1(-5)\exp(-15.7/u_e)}{1+1.68(+7)\exp(-11.7/u_e)}$	10
B5	$H_2O + e \longrightarrow OH^- + H$	$2.8(-6)\,u_e^{-7.2}\exp(-12.9/u_e)$	10
B6	$HNO_2 + e \longrightarrow NO_2^- + H$	$5.0(-8)$	11
B7	$HNO_3 + e \longrightarrow NO_2^- + OH$	$5.0(-8)$	12
B8	$HNO_4 + e \longrightarrow NO_3^- + OH$	$5.0(-8)$	11
B9	$NO + e \longrightarrow O^- + N$	$3.4(-6)\,u_e^{-8.2}\exp(-15.2/u_e)$	10
B10	$NO_2 + e \longrightarrow NO_2^-$	$4.0(-11)$	13
B11	$NO_2 + e \longrightarrow O^- + NO$	$3.4(-10)\,u_e^{-2.4}\exp(-3.0/u_e)$	10
B12	$N_2O + e \longrightarrow O^- + N_2(0)$	$5.0(-9)\,u_e^{-2.65}\exp(-3.05/u_e)$	10
B13	$N_2O_5 + e \longrightarrow NO_3^- + NO_2$	$5.0(-9)\,u_e^{-2.65}\exp(-3.05/u_e)$	14
B14	$O_2 + e \longrightarrow O^- + O$	$2.8(-6)\,u_e^{-7.9}\exp(-13.5/u_e)$	10
B15	$O_3 + e \longrightarrow O^- + O_2$	$4.0(-11)$	9
B16	$C_5H_{12} + e \longrightarrow C_5H_{12}^-$	$1.0(-12)$	15

	Reaction	Rate Constant	Ref.
C1	$O^- + CO(0) \longrightarrow CO_2(020) + e$	$5.8(-9)\ T^{-0.4}$	16
C2	$O^- + H_2 \longrightarrow H_2O + e$	$2.5(-9)\ T^{-0.25}$	16
C3	$O^- + NO \longrightarrow NO_2 + e$	$1.8(-8)\ T^{-0.75}$	16
C4	$O^- + N \longrightarrow NO + e$	2.2(-10)	17
C5	$O^- + 0 \longrightarrow O_2 + e$	1.9(-10)	17
C6	$OH^- + H \longrightarrow H_2O + e$	1.8(-9)	18
C7	$OH^- + O \longrightarrow HO_2 + e$	2.0(-10)	18
C8	$O_2^- + H \longrightarrow HO_2 + e$	1.5(-9)	19
C9	$O_2^- + N \longrightarrow NO_2 + e$	4.0(-10)	17
C10	$O_2^- + O \longrightarrow O_3 + e$	3.3(-10)	17
C11	$O_3^- + O \longrightarrow O_2 + O_2 + e$	1.0(-10)	20
C12	$O_3^- + O_3 \longrightarrow O_3 + O_3 + e$	1.0(-10)	21

	Reaction	Rate Constant	Ref.
D1	$CO_2^+ + e \longrightarrow CO(1) + O$	$2.0(-5)\ T^{-1.0}\ u_e^{-0.5}$	10, 22, 23, 24
D2	$HCO^+ + e \longrightarrow CO(1) + H$	$1.0(-5)\ T^{-1.0}\ u_e^{-0.5}$	25
D3	$HCO_2^+ + e \longrightarrow CO_2(020) + H$	$4.0(-5)\ T^{-1.0}\ u_e^{-0.5}$	26
D4	$H_3O^+ + e \longrightarrow H_2O + H$	$3.0(-4)\ T^{-1.0}\ u_e^{-0.5}$	27
D5	$NO^+ + e \longrightarrow NO$	$3.0(-4)\ T^{-10}\ u_e^{-0.5}$	27
D6	$O_2^+ + e \longrightarrow O + O$	$6.0(-7)\ T^{-0.5}\ u_e^{-0.5}$	28

	Reaction			Rate Coefficient	Ref.
E1	$CO_2^+ - CO_3^-$	→	$CO_2(020) + CO_2(020) + O$	5.0(-7)	29
E2	$CO_2^+ + CO_4^-$	→	$CO_2(020) + CO_2(020) + O_2$	5.0(-7)	29
E3	$CO_2^+ + NO_2^-$	→	$CO(1) + NO_2 + O$	6.0(-7)	29
E4	$CO_2^+ + NO_3^-$	→	$CO(1) + NO_3 + O$	5.0(-7)	29
E5	$CO_2^+ + O_2^-$	→	$CO(1) + O_2 + O$	6.0(-7)	29
E6	$CO_2^+ + O_4^-$	→	$CO_2(020) + O_2 + O_2$	5.0(-7)	29
E7	$HCO^+ + CO_3^-$	→	$CO_2(020) + CO(1) + OH$	3.0(-7)	29
E8	$HCO^+ + CO_4^-$	→	$CO_2(020) + CO(1) + HO_2$	3.0(-7)	29
E9	$HCO^+ + O_2^-$	→	$CO(1) + O_2 + H$	3.0(-7)	29
E10	$HCO_2^+ + CO_3^-$	→	$CO_2(020) + CO_2(020) + OH$	1.0(-6)	29
E11	$HCO_2^+ + CO_4^-$	→	$CO_2(020) + CO_2(020) + HO_2$	1.0(-6)	29
E12	$HCO_2^+ + O_2^-$	→	$CO_2(020) + O_2 + H$	1.2(-6)	29
E13	$H_3O^+ + CO_3^-$	→	$CO_2(020) + H_2O + OH$	2.4(-6)	29
E14	$H_3O^+ + CO_4^-$	→	$CO_2(020) + H_2O + HO_2$	2.4(-6)	29
E15	$H_3O^+ + NO_2^-$	→	$NO_2 + H_2O + H$	2.4(-6)	29
E16	$H_3O^+ + NO_3^-$	→	$NO_2 + H_2O + OH$	2.4(-6)	29
E17	$H_3O^+ + O_2^-$	→	$H_2O + O_2 + H$	2.4(-6)	29

	Reaction			Rate Constant	Ref.
E18	$NO^+ + CO_3^-$	→	$CO_2(020) + NO + O$	6.0(-7)	29
E19	$NO^+ + CO_4^-$	→	$CO_2(020) + NO + O_2$	6.0(-7)	29
E20	$NO^+ + NO_2^-$	→	$NO_2 + N + O$	5.0(-7)	30
E21	$NO^+ + NO_3^-$	→	$NO_3 + N + O$	8.0(-7)	30
E22	$NO^+ + O_2^-$	→	$O_2 + N + O$	6.0(-7)	30
E23	$NO^+ + O_4^-$	→	$NO + O_2 + O_2$	6.0(-7)	29
E24	$O_2^+ + CO_3^-$	→	$CO_2(020) + O_2 + O$	3.0(-7)	29
E25	$O_2^+ + CO_4^-$	→	$CO_2(020) + O_2 + O_2$	3.0(-7)	29
E26	$O_2^+ + NO_2^-$	→	$NO_2 + O + O$	4.0(-7)	30
E27	$O_2^+ + NO_3^-$	→	$NO_3 + O + O$	1.3(-7)	30
E28	$O_2^+ + O_2^-$	→	$O_2 + O + O$	4.0(-7)	30
E29	$O_2^+ + O_4$	→	$O_2 + O_2 + O_2$	3.0(-7)	29

	Reaction			Rate Coefficient	Ref.
F1	$CO_2^+ + O$	→	$O_2^+ + CO(0)$	2.6 (-10)	31
F2	$CO_2^+ + H$	→	$HCO^+ + O$	6.0 (-10)	31
F3	$CO_2^+ + H_2$	→	$HCO_2^+ + H$	1.4 (-9)	31
F4	$CO_2^+ + H_2O$	→	$HCO_2^+ + OH$	1.4 (-9)	31
F5	$CO_2^+ + NO$	→	$NO^+ + CO_2(000)$	4.5 (-10)	38
F6	$CO_2^+ + O_2$	→	$O_2^+ + CO_2(000)$	1.1 (-14) T exp (1800/RT)	17
F7	$CO^+ + CO_2(000)$	→	$CO_2^+ + CO(0)$	1.2 (-9)	17
F8	$HCO^+ + H_2O$	→	$H_3O^+ + CO(1)$	3.0 (-9)	32
F9	$HCO^+ + NO$	→	$NO^+ + CHO$	1.2 (-10)	33
F10	$HCO_2^+ + CO(0)$	→	$HCO^+ + CO_2(020)$	3.0 (-9)	34
F11	$HCO_2^+ + H_2$	→	$H_3O^+ + CO(1)$	3.0 (-9)	35
F12	$HCO_2^+ + H_2O$	→	$H_3O^+ + CO_2(020)$	3.0 (-9)	34
F13	$He^+ + CO_2(000)$	→	$CO^+ + O + He$	1.2 (-9)	17
F14	$N^+ + CO_2(000)$	→	$CO^+ + NO$	2.3 (10)	37
F15	$N^+ + CO_2(000)$	→	$CO_2^+ + N$	7.5 (-10)	37
F16	$N^+ + CO(0)$	→	$CO^+ + N$	4.5 (-10)	37
F17	$N^+ + O_2$	→	$NO^+ + O$	2.6 (-10)	37

	Reaction			Rate Coefficient	Ref.
F18	$N^+ + O_2$	→	$O^+ + NO$	3.7 (-11)	37
F19	$N^+ + O_2$	→	$O_2^+ + N$	3.1 (-10)	37
F20	$N_2^+ + CO_2(000)$	→	$CO_2^+ + N_2(0)$	1.0 (-9)	17
F21	$O^+ + CO_2(000)$	→	$O_2^+ + CO(1)$	9.4 (-10)	37
F22	$O^+ + N_2(0)$	→	$NO^+ + N$	1.2 (-12)	37
F23	$O^+ + O_2$	→	$O_2^+ + O$	1.9 (-11)	37
F24	$O_2^+ + N$	→	$NO^+ + O$	1.8 (-10)	17
F25	$O_2^+ + NO$	→	$NO^+ + O_2$	4.5 (-10)	38
F26	$CO_2^{*+} + M1$	→	$CO^+ + O + M1$	3.0 (-10)	39
F27	$CO_2^{*+} + M1$	→	$O^+ + CO(0) + M1$	3.0 (-10)	39
F28	$N_2^{*+} + M1$	→	$N^+ + N + M1$	3.0 (-10)	39
F29	$O_2^{*+} + M1$	→	$O^+ + O + M1$	3.0 (-10)	39
F30	$CO^{*+} + CO_2(000)$	→	$O^+ + CO(0) + CO(0)$	1.0 (-9)	39
F31	$CO_3^- + H$	→	$OH^- + CO_2(000)$	1.7 (-10)	18
F32	$CO_3^- + HNO_3$	→	$NO_3^- + OH + CO_2(000)$	8.0 (-10)	12
F33	$CO_4^- + H$	→	$CO_3^- + OH$	2.2 (-10)	18

	Reaction			Rate Coefficient	Ref.
F34	$O^- + CO_2(000) + M1$	→	$CO_3^- + M1$	$5.0(-25)\ T^{-1.0}$	40
F35	$O^- + NO + M1$	→	$NO_2^- + M1$	$3.0(-28)\ T^{-1.0}$	41
F36	$O^- + O_2 + M1$	→	$O_3^- + M1$	$3.0(-28)\ T^{-1.0}$	10,20
F37	$O^- + O_2 + M5$	→	$O_3^- + M5$	$2.0(-30)$	20
F38	$O_2^- + CO_2(000) + M5$	→	$CO_4^- + M5$	$5.2(-29)$	42
F39	$O_2^- + NO + M1$	→	$NO_3^- + M1$	$3.0(-28)\ T^{-1.0}$	10,20
F40	$O_2^- + O + M1$	→	$O_3^- + M1$	$3.0(-28)\ T^{-1.0}$	10,20
F41	$O_2^- + O_2 + M1$	→	$O_4^- + M1$	$2.0(-27)\ T^{-1.5}$	43
F42	$CO_3^- + NO$	→	$NO_2^- + CO_2(020)$	$1.8(-11)$	17
F43	$CO_3^- + NO_2$	→	$NO_3^- + CO_2(000)$	$2.0(-10)$	42
F44	$CO_3^- + O$	→	$O_2^- + CO_2(020)$	$8.0(-11)$	17
F45	$CO_4^- + NO$	→	$NO_3^- + CO_2(000)$	$4.8(-11)$	21
F46	$CO_4^- + O$	→	$CO_3^- + O_2$	$1.5(-10)$	21
F47	$CO_4^- + O_3$	→	$O_3^- + CO_2(000) + O_2$	$1.3(-10)$	42
F48	$NO_2^- + H$	→	$OH^- + NO$	$3.7(-10)$	18
F49	$NO_2^- + HNO_3$	→	$NO_3^- + HNO_2$	$1.6(-9)$	12
F50	$NO_2^- + NO_3$	→	$NO_3^- + NO_2$	$3.0(-10)$	17

	Reaction			Rate Coefficient	Ref.
F51	$NO_2^- + O_3$	→	$NO_3^- + O_2$	1.8 (-11)	21
F52	$O^- + H_2O$	→	$OH^- + OH$	1.4 (-9)	31
F53	$O^- + HNO_3$	→	$NO_3^- + OH$	3.0 (-9)	12
F54	$O^- + NO_2$	→	$NO_2^- + O$	1.2 (-9)	17
F55	$O^- + O_3$	→	$O_3^- + O$	5.3 (-10)	17
F56	$OH^- + NO_2$	→	$NO_2^- + OH$	1.9 (-9)	18
F57	$O_2^- + HNO_3$	→	$NO_3^- + HO_2$	2.8 (-9)	12
F58	$O_2^- + NO_2$	→	$NO_2^- + O_2$	1.2 (-9)	42
F59	$O_2^- + OH$	→	$OH^- + O_2$	6.0 (-10)	17,42
F60	$O_2^- + O_3$	→	$O_3^- + O_2$	3.0 (-10)	17
F61	$O_3^- + CO_2(000)$	→	$CO_3^- + O_2$	6.0 (-10)	42
F62	$O_3^- + H$	→	$OH^- + O_2$	8.4 (-10)	19
F63	$O_3^- + NO$	→	$NO_3^- + O$	1.0 (-11)	17
F64	$O_3^- + NO_2$	→	$NO_3^- + O_2$	2.8 (-10)	17
F65	$O_3^- + O$	→	$O_2^- + O_2$	1.0 (-10)	20
F66	$O_4^- + CO_2(000)$	→	$CO_4^- + O_2$	4.8 (-10)	21
F67	$O_4^- + NO$	→	$NO_3^- + O_2$	2.5 (-10)	21

	Reaction			Rate Coefficient	Ref.
F68	$O_4^- + O$	→	$O_3^- + O_2$	4.0(-10)	21
F69	$C_5H_{12}^- + N_2O$	→	$O^- + N_2(0) + C_5H_{12}$	1.0(-9)	44
F70	$C_5H_{12}^- + O$	→	$O^- + C_5H_{12}$	1.0(-9)	44
F71	$C_5H_{12}^- + O_2$	→	$O_2^- + C_5H_{12}$	1.0(-9)	44
F72	$C_5H_{12}^- + NO_2$	→	$NO_2^- + C_5H_{12}$	1.0(-9)	44

	Reaction			Rate Coefficient	Ref.
G1	$CO_2(000) + e$	$\rightleftharpoons$	$CO_2(010) + e$	$7.7(-9)\ \exp(-0.21/u_e)$	45
G2	$CO_2(000) + e$	$\rightleftharpoons$	$CO_2(100) + e$	$1.0(-9)\ u_e^{0.36}\ \exp(-0.23/u_e)$	46
G3	$CO_2(000) + e$	$\rightleftharpoons$	$CO_2(020) + e$	$4.0(-9)\ u_e^{0.36}\ \exp(-0.23/u_e)$	47
G4	$CO_2(000) + e$	$\rightleftharpoons$	$CO_2(030) + e$	$\frac{1.4(-13)\ \exp(10.6\ u_e)}{1 + 1.9(-5)\exp(10.6\ u_e)}$	48
G5	$CO_2(000) + e$	$\rightleftharpoons$	$CO_2(001) + e$	$6.8(-9)\ \exp(-0.25/u_e)$	49
G6	$N_2(0) + e$	$\rightleftharpoons$	$N_2(1) + e$	$\frac{5.4(-12)\ \exp(10.1\ u_e)}{1 + 2.33(-4)\ \exp(10.1\ u_e)}$	50
G7	$CO(0) + e$	$\rightleftharpoons$	$CO(1) + e$	$\frac{2.4(-7)\ u_e^{0.5}\ \exp(-1.31/u_e)}{1 + 5.33\ u_e\ \exp(-1.31/u_e)}$	51
G8	$CO_2(000) + e$	$\rightarrow$	$CO_2^* + e$	$\frac{1.0\ \exp(-22.4/u_e)}{1 + 3.28(+8)\ \exp(-15.93/u_e)}$	52
G9	$N_2(0) + e$	$\rightarrow$	$N_2^* + e$	$\frac{3.56(+4)\ \exp(-27.0/u_e)}{1 + 1.9(+12)\ \exp(-21.6/u_e)}$	52
G10	$CO(0) + e$	$\rightarrow$	$CO^* + e$	$\frac{1.15(-2)\ \exp(-17.3/u_e)}{1 + 1.7(+6)\ \exp(-12.0/u_e)}$	53
G11	$CO_2^* + M1$	$\rightarrow$	$CO_2(000) + M1$	$1.0(-11)$	54

	Reaction			Rate Coefficient	Ref.
G12	$CO_2^* + CO_2(000)$	→	$CO_2(000) + CO(0) + O$	1.0(-10)	55
G13	$CO^* + CO_2(000)$	→	$CO(0) + CO(0) + O$	1.0(-10)	55
G14	$CO^* + M1$	→	$CO(0) + M1$	1.0(-11)	56
G15	$N_2^* + M1$	→	$N_2(0) + M1$	1.0(-11)	57
G16	$N_2^* + CO_2(000)$	→	$N + NO + CO(0)$	1.0(-10)	55
G17	$N_2^* + CO_2(000)$	→	$N_2(0) + CO(0) + O$	1.0(-11)	55
G18	$N_2^* + CO_2(000)$	→	$N_2O + CO(0)$	1.0(-11)	55
G19	$N_2^* + O_2$	→	$NO + NO$	1.0(-10)	55

	Reaction			Rate Coefficient	Ref.
H1	$CO_2(001) + N_2(O)$	$\rightleftharpoons$	$CO_2(000) + N_2(1)$	$8.3(-12)\ T^{-0.5}$	58
H2	$CO_2(001) + N_2(0)$	$\rightleftharpoons$	$CO_2(000) + N_2(1)$	$6.4(-12)\ \exp(-11700.0/RT)$	58
H3	$CO_2(001) + CO(0)$	$\rightleftharpoons$	$CO_2(000) + CO(1)$	$1.4(-17)\ T^{1.65}$	59
H4	$CO_2(020) + CO_2(000)$	$\rightleftharpoons$	$CO_2(010) + CO_2(010)$	$1.4(-12)\ T^{0.5}$	60
H5	$CO_2(030) + CO_2(000)$	$\rightleftharpoons$	$CO_2(020) + CO_2(010)$	$3.1(-13)\ T^{0.5}$	60
H6	$CO(1) + CO_2(000)$	$\rightleftharpoons$	$CO(0) + CO_2(030)$	$1.0(-11)\ \exp(-50.0/RT^{0.33})$	61
H7	$N_2(1) + CO(0)$	$\rightleftharpoons$	$N_2(0) + CO(1)$	$2.7(-18)\ T^{1.5}$	62
H8	$CO_2(001) + M_2$	$\rightleftharpoons$	$CO_2(030) + M_2$	$1.2(-21)\ T^{2.6}$	63
H9	$CO_2(001) + M_2$	$\rightleftharpoons$	$CO_2(030) + M_2$	$1.4(-10)\ T^{-2.0}$	63
H10	$CO_2(001) + M_3$	$\rightleftharpoons$	$CO_2(030) + M_3$	$3.0(-21)\ T^{2.3}$	64
H11	$CO_2(001) + H_2$	$\rightleftharpoons$	$CO_2(030) + H_2$	$1.7(-17)\ T^{1.5}$	65
H12	$CO_2(001) + H_2O$	$\rightleftharpoons$	$CO_2(030) + H_2O$	$2.5(-15)\ T^{1.0}$	66
H13	$CO_2(100) + CO_2(000)$	$\rightleftharpoons$	$CO_2(020) + CO_2(000)$	$4.2(-12)$	67
H14	$CO_2(030) + M4$	$\rightleftharpoons$	$CO_2(020) + M4$	$1.9(-24)\ T^{3.6}\ \exp(30.0/RT^{0.33})$	68
H15	$CO_2(020) + M4$	$\rightleftharpoons$	$CO_2(010) + M4$	$1.25(-24)\ T^{3.6}\ \exp(30.0/RT^{0.33})$	68
H16	$CO_2(010) + M4$	$\rightleftharpoons$	$CO_2(000) + M4$	$6.2(-25)\ T^{3.6}\ \exp(30.0/RT^{0.33})$	69
H17	$CO_2(030) + CO(0)$	$\rightleftharpoons$	$CO_2(020) + CO(0)$	$1.4(-9)\ T^{-1.0}$	70

	Reaction			Rate Coefficient	Ref.
H18	$CO_2(020) + CO(0)$	$\rightleftharpoons$	$CO_2(010) + CO(0)$	$9.0(-10)\ T^{-1.0}$	70
H19	$CO_2(010) + CO(0)$	$\rightleftharpoons$	$CO_2(000) + CO(0)$	$4.5(-10)\ T^{-1.0}$	71
H20	$CO_2(030) + He$	$\rightleftharpoons$	$CO_2(020) + He$	$3.0(-21)\ T^{3.0}\ \exp(843/RT)$	72
H21	$CO_2(020) + He$	$\rightleftharpoons$	$CO_2(010) + He$	$2.0(-21)\ T^{3.0}\ \exp(843/RT)$	72
H22	$CO_2(010) + He$	$\rightleftharpoons$	$CO_2(000) + He$	$1.0(-21)\ T^{3.0}\ \exp(843/RT)$	60
H23	$CO_2(030) + H_2$	$\rightleftharpoons$	$CO_2(020) + H_2$	$2.3(12)\ T^{0.25}$	73
H24	$CO_2(020) + H_2$	$\rightleftharpoons$	$CO_2(010) + H_2$	$1.5(-12)\ T^{0.25}$	73
H25	$CO_2(010) + H_2$	$\rightleftharpoons$	$CO_2(000) + H_2$	$7.5(-13)\ T^{0.25}$	69
H26	$CO_2(030) + H_2O$	$\rightleftharpoons$	$CO_2(020) + H_2O$	$4.2(-11)$	74
H27	$CO_2(020) + H_2O$	$\rightleftharpoons$	$CO_2(010) + H_2O$	$2.8(-11)$	74
H28	$CO_2(010) + H_2O$	$\rightleftharpoons$	$CO_2(000) + H_2O$	$1.4(-11)$	69
H29	$CO(1) + M1$	$\rightleftharpoons$	$CO(0) + M1$	$6.7(-8)\ \exp(-414/RT^{0.33})$	75
H30	$CO(1) + H_2$	$\rightleftharpoons$	$CO(0) + H_2$	$2.1(-8)\ \exp(-249/RT^{0.33})$	76
H31	$CO(1) + H_2O$	$\rightleftharpoons$	$CO(0) + H_2O$	$3.1(-10)\ \exp(-129/RT^{0.33})$	75
H32	$N_2(1) + M1$	$\rightleftharpoons$	$N_2(0) + M1$	$8.5(-7)\ \exp(-543/RT^{0.33})$	75
H33	$N_2(1) + H_2O$	$\rightleftharpoons$	$N_2(0) + H_2O$	$1.5(-10)\ \exp(-139/RT^{0.33})$	77,69

	Reaction			Rate Coefficient	Ref.
J1	$H + H + M6$	$\rightleftharpoons$	$H_2 + M6$	$2.8(-30)\ T^{-1.0}$	78
J2	$H + OH + M6$	$\rightleftharpoons$	$H_2O + M6$	$6.1(-26)\ T^{-2.0}$	79
J3	$H + O_2 + M6$	$\rightleftharpoons$	$HO_2 + M_6$	$2.1(-32)\ \exp(580/RT)$	80
J4	$CO(0) + H + M6$	$\rightleftharpoons$	$CHO + M6$	$2.0(-33)\ \exp(-1700/RT)$	81
J5	$HO_2 + NO + M6$	$\rightleftharpoons$	$HNO_3 + M6$	$3.5(-31)$	82
J6	$HO_2 + NO_2 + M6$	$\rightleftharpoons$	$HNO_4 + M6$	$2.1(-31)$	83
J7	$N + N + M6$	$\rightleftharpoons$	$N_2(1) + M6$	$8.3(-34)\ \exp(1000/RT)$	80
J8	$N + O + M6$	$\rightleftharpoons$	$NO + M6$	$1.8(-31)\ T^{-0.5}$	80
J9	$O + CO(0) + M7$	$\rightleftharpoons$	$CO_2(020) + M7$	$2.0(-33)\ \exp(-4000/RT)$	84, 85, 86
J10	$O + H + M6$	$\rightleftharpoons$	$OH + M6$	$1.0(-32)$	87
J11	$O + NO + M6$	$\rightleftharpoons$	$NO_2 + M6$	$4.0(-33)\ \exp(-1880/RT)$	30
J12	$O + NO_2 + M6$	$\rightleftharpoons$	$NO_3 + M6$	$1.8(-32)\ \exp(1000/RT)$	80
J13	$O + O + M6$	$\rightleftharpoons$	$O_2 + M6$	$3.8(-30)\ T^{-1.0}\ \exp(-340/RT)$	80
J14	$O + O_2 + M6$	$\rightleftharpoons$	$O_3 + M_6$	$1.0(-34)\ \exp(1010/RT)$	80

	Reaction			Rate Coefficient	Ref.
K1	$CH_2O + M6$	$\rightleftharpoons$	$CO(0) + H_2 + M6$	3.5(-8) exp(-35000/RT)	88
K2	$CH_2O + H$	$\rightleftharpoons$	$CHO + H_2$	2.2(-11) exp(-3800/RT)	89
K3	$CH_2O + O$	$\rightleftharpoons$	$CHO + OH$	1.6(-13)	90
K4	$CH_2O + OH$	$\rightleftharpoons$	$CHO + H_2O$	9.0(-13) $T^{0.5}$	88, 91
K5	$CHO + O$	$\rightleftharpoons$	$CO(0) + OH$	2.1(-10)	80
K6	$CHO + OH$	$\rightleftharpoons$	$CO(0) + H_2O$	2.1(-10)	92
K7	$CHO + O_2$	$\rightleftharpoons$	$CO(0) + HO_2$	8.3(-11) exp(-1600/RT)	80, 88
K8	$H + NO_2$	$\rightleftharpoons$	$OH + NO$	6.0(-10) exp(-1500/RT)	79
K9	$H + O_3$	$\rightleftharpoons$	$OH + O_2$	2.6(-11)	93
K10	$HO_2 + H$	$\rightleftharpoons$	$H_2 + O_2$	4.2(-11) exp(-700/RT)	79
K11	$HO_2 + H$	$\rightleftharpoons$	$OH + OH$	4.2(-10) exp(-1900/RT)	79
K12	$HO_2 + NO$	$\rightleftharpoons$	$NO_2 + OH$	2.0(-13)	93
K13	$HO_2 + N_2O_5$	$\rightleftharpoons$	$HNO_4 + NO_3$	1.0(-11)	94
K14	$HO_2 + O$	$\rightleftharpoons$	$OH + O_2$	8.0(-11) exp(-1000/RT)	95
K15	$HO_2 + OH$	$\rightleftharpoons$	$H_2O + O_2$	8.3(-11) exp(-1000/RT)	95
K16	$HO_2 + O_3$	$\rightleftharpoons$	$OH + O_2 + O_2$	1.0(-13) exp(-2500/RT)	93
K17	$N + NO$	$\rightleftharpoons$	$N_2(O) + 0$	2.7(-11)	80

	Reaction			Rate Coefficient	Ref.
K18	$N + NO_2$	$\rightleftharpoons$	$N_2O + O$	2.0(-11) exp(-1600/RT)	96
K19	$N + NO_3$	$\rightleftharpoons$	$NO + NO_2$	5.7(-13)	97
K20	$N + O_2$	$\rightleftharpoons$	$NO + O$	1.1(-14) T exp(-6300/RT)	80
K21	$N + O_3$	$\rightleftharpoons$	$NO + O_2$	5.7(-13)	80
K22	$O + NO_2$	$\rightleftharpoons$	$O_2 + NO$	1.6(-10) $T^{-0.5}$	98
K23	$O + NO_3$	$\rightleftharpoons$	$O_2 + NO_2$	5.7(-13)	97
K24	$O + N_2O_5$	$\rightleftharpoons$	$NO_2 + NO_2 + O_2$	1.0(-14)	93
K25	$O + O_3$	$\rightleftharpoons$	$O_2 + O_2$	1.9(-11) exp(-4600/RT)	80
K26	$OH + CO(0)$	$\rightleftharpoons$	$CO_2(000) + H$	1.1(-19) $T^{2.0}$ exp(1600/RT)	99
K27	$OH + H_2$	$\rightleftharpoons$	$H_2O + H$	1.0(-17) $T^{2.0}$ exp(-2900/RT)	100
K28	$OH + HNO_2$	$\rightleftharpoons$	$H_2O + NO_2$	3.5(-13) exp(-600/RT)	101
K29	$OH + HNO_3$	$\rightleftharpoons$	$H_2O + NO_3$	3.5(-13) exp(-600/RT)	93
K30	$OH + N$	$\rightleftharpoons$	$NO + H$	5.3(-11)	79
K31	$OH + NO$	$\rightleftharpoons$	HNO_2	2.0(-12)	79
K32	$OH + NO_2$	$\rightleftharpoons$	HNO_3	1.0(-11) exp(-340/RT)	79
K33	$OH + O$	$\rightleftharpoons$	$H + O_2$	4.0(-11)	79, 102
K34	$OH + OH$	$\rightleftharpoons$	$H_2O + O$	1.0(-11) exp(-1100/RT)	79

	Reaction			Rate Coefficient	Ref.
K35	$OH + O_3$	$\rightleftharpoons$	$HO_2 + O_2$	1.6(-12) exp(-2000/RT)	93
K36	$NO + NO_3$	$\rightleftharpoons$	$NO_2 + NO_2$	8.7(-12)	80
K37	$NO + O_3$	$\rightleftharpoons$	$NO_2 + O_2$	9.0(-13) exp(-2400/RT)	80
K38	$NO_2 + NO_3$	$\rightleftharpoons$	N_2O_5	4.0(-12)	79
K39	$NO_2 + NO_3$	$\rightleftharpoons$	$NO_2 + O_2 + NO$	2.3(-13) exp(-3200/RT)	80
K40	$NO_2 + O_3$	$\rightleftharpoons$	$NO_3 + O_2$	1.2(-13) exp(-4900/RT)	103
K41	$NO_3 + NO_3$	$\rightleftharpoons$	$NO_2 + O_2 + NO_2$	5.0(-12) exp(-6000/RT)	80

Catalytic Species

M1	All
M2	1.0 CO_2, 0.6 CO
M3	1.0 N_2, 1.2 O_2, 0.8 He
M4	All, except He, H_2, H_2O, CO
M5	1.0 O, 1.0 O_2, 1.0 O_3
M6	2.0 CO_2, 0.5 He, 1.0 all other
M7	All, except 3.0 CO_2, 1.5 CO, 20.0 O_2

ANNOTATED REFERENCES

1. This work, Eq. (29), using ionization energies from D.H. Douglas-Hamilton, R.S. Lowder, "Carbon Dioxide Electric Discharge Laser Kinetics Handbook," AFWL-TR-74-216, p. 57. Rates have been split roughly 0.8/0.2 for ground state ionization and electronically excited ionization, respectively. The latter is an artifice allowing treatment of the quartic processes $A + e_{EB} \rightarrow B^+ + C + e + e_{EB}$, using cross sections reported in Ref. 105 for guidance.
2. Estimated equal to 0.005 times ionization rate based on a cross section reported in Ref. 105.
3. Estimated equal to twice the ionization rate based on mean energy loss per ion pair (33.8 eV) and mean excitation energy (6.7 eV).
4. Estimated equal to twice the ionization rate.
5. Estimated equal to 0.015 times ionization rate based on cross section reported in Ref. 105.
6. Estimated equal to 0.01 times ionization rate based on cross section reported in Ref. 105.
7. See Fig. 18. Best fit to data for $CO_2/N_2/H_2 = 1/3/0.1$. For $CO_2/N_2/He = 1/2/3$, multiply by 0.5. For $CO_2/CO/N_2/He = 1/1/4/6$, use $k = 2.3\,(-10) \times u_e^{0.19} \exp(-13.5/u_e)$.
8. See Fig. 19.
9. Bortner, M.H., A Review of Rate Constants of Selected Reactions of Interest in Reentry Flow Fields in the Atmosphere, National Bureau of Standards Technical Note 484, Washington, D.C., May 1969.
10. Nighan, W.L., and W.J. Wiegand, "Influence of Negative-Ion Processes on Steady-State Properties and Striations in Molecular Gas Discharges," Phys. Rev. A, Vol. 10, 1974, p. 922.
11. Assumed equal to rate for B7.
12. Fehsenfeld, F.C., C.J. Howard and A.L. Schmeltekopf, "Gas Phase Ion Chemistry of HNO_3," J. Chem. Phys., Vol. 63, 1975, p. 2835.
13. Mahan, B.H., and I.C. Walker, "Rate of Attachment of Gaseous Electrons to Nitrogen Dioxide," J. Chem. Phys., Vol. 47, 1967, p. 3780.
14. Assumed equal to rate for B12.
15. Estimate based in part on the observation that both n-Butane and n-Hexane have been used as inert carriers in determination of the electron attachment coefficients of SF_6 and $CC\ell_4$ at concentration levels of about 10 ppm.

16. McFarland, M., D. L. Albritton, F. C. Fehsenfeld, E. E. Ferguson and A. L. Schmeltekopf, "Flow Drift Technique for Ion Mobility and Ion Molecule Reaction Rate Constant Measurements, III. Negative Ion Reactions of 0^- with CO, NO, H_2 and D," J. Chem. Phys., Vol. 59, 1973, p. 6629.

17. Fehsenfeld, F. C., A. L. Schmeltekopf, D. B. Dunkin and E. E. Ferguson, "Compilation of Reaction Rate Constants Measured in the ESSA Flowing Afterglow System to August 1969," ESSA Technical Report ERL 135-AL3, Boulder, Colo., September 1969.

18. Ferguson, E. E., "Laboratory Measurements of Ionospheric Ion-Molecule Reaction Rates," Rev. Geophys. Space Phys., Vol. 12, 1974, p. 703.

19. Fehsenfeld, F. C., "Reaction of CO_3^-, NO_3^-, and CO_4^- with Atomic Hydrogen," J. Chem. Phys., Vol. 63, 1975, p. 1686.

20. Sutton, E. A., "Chemistry of Electrons in Pure-Air Hypersonic Wakes," AIAA J., Vol. 6, p. 1873, 1968.

21. Thomas, L., P. M. Gondhalekar and M. R. Bowman, "The Negative Ion Composition of the Daytime D-Region," J. Atmospheric and Terrestrial Physics, Vol. 35, 1973, p. 397.

22. Biondi, M. A., "The Effects of Ion Complexity on Electron-Ion Recombination," Comments on Atomic and Molecular Physics, Part D, 1974, p. 85.

23. Bates, D. R., and A. Dalgarno, "Electronic Recombination," in Atomic and Molecular Processes (Ed. D. R. Bates), Academic Press, New York, 1962, pp. 245-279.

24. Theoretical analysis by Bates (Ref. 23) predicts the limiting T^{-1} ion temperature dependence (and also $u_e^{-0.5}$ for all conditions) for recombination in which neutral product stabilization, rather than radiationless transition is rate-limiting. Intuitively, it seems that the multiplicity of rovibronic states available to complex ions should favor radiationless transition by increasing the overlap between bound and unbound states.

25. Assumed equal to 0.5 times rate of D1.

26. Assumed equal to twice the rate of D1.

27. Mitra, A. P., and J. N. Rowe, "Ionospheric Effects of Solar Flares — VI. Changes in D-Region Ion Chemistry During Solar Flares," J. Atmos. Terr. Phys., Vol. 34, 1972, p. 795.

    For cluster ions proceeding through the sequence NO^+ (or H_3O^+) to $H_3O^+(H_2O)_n$ which may be anticipated in the environments of interest.

28. Kasner, W. H., and M. A. Biondi, "Temperature Dependence of the Electron-O_2^+ Ion Recombination Coefficient," Phys. Rev., Vol. 174, 1968, p. 139.

29. The largely unknown ionic mutual neutralization rate coefficients have all been estimated by scaling of the few available measurements by the reciprocal square root of the reduced mass of the interacting ions within the positive ion groupings O_2^+, NO^+, and CO_2^+, also scaling via the ratio of the CO_2^+ to O_2^+ dissociative ion-electron recombination coefficients.

30. Moseley, J. T., R. E. Olson and J. R. Peterson, Case Studies in Atomic Physics, Vol. 5, (E. W. McDaniel and M. R. C. McDowell), North Holland Publishers, Amsterdam, 1975, pp. 1-45.

31. Ferguson, E. E., "Rate Constants of Thermal Energy Binary Ion-Molecule Reactions of Aeronomic Interest," Atomic Data and Nuclear Data Tables, Vol. 12, 1973, p. 159.

32. Pritchard, H., and G. Harrison, "Ion-Molecule Reactions of Oxygenated Species. Proton-Transfer Reactions Involving CHO^+," J. Chem. Phys., Vol. 48, 1968, p. 5623.

33. Hurle, I. R., T. M. Sugden and G. B. Nutt, "Chemi-Ionization of Nitric Oxide in Flames Containing Hydrocarbon Additives," Twelfth Symposium (International) on Combustion, The Combustion Institute, Pittsburgh, Pa., 1969, p. 387.

34. Estimate, based on Ref. 32.

35. Estimated at one third the rate for the process $HCO_2^+ + H_2O$, based on finding (this work) that exclusion of this process leads to ion species distributions in the presence of H_2 which are inconsistent with mass spectral observations made in Ref. 36.

36. Smith, A. L. S., and H. Shields, "Positive Ion Processes in the Positive Column of CO_2 Laser Electrical Discharges," J. Chem. Phys., Vol. 67, 1977, p. 1594.

37. Smith, D., N. G. Adams and T. M. Miller, "A Laboratory Study of the Reactions of N^+, N_2^+, N_3^+, N_4^+, O^+, O_2^+ and NO^+ Ions with Several Molecules at 300 K," J. Chem. Phys., Vol. 69, 1978, p. 308.

38. Johnson, R., H. L. Brown and M. A. Biondi, "Ion-Molecule Reactions Involving N_2^+, N^+, O_2^+ and O^+ ions from 300 K to ~1 eV," J. Chem. Phys., Vol. 52, 1970, p. 5080.

39. Reactions involving electronically excited ions have been added to avoid the necessity of introducing yet another reaction type such as $A + e_{EB} \rightarrow B^+ + C + e + e_{EB}$. All of the dissociation rates for these excited ionic species have been assumed to proceed at essentially the collision frequency, except for the $CO^{*+} + CO_2$ reaction rate which was assumed to be quite rapid.

40. Mitchum, R. K., J. P. Freeman and G. G. Meisels, "Arrival Time Distribution in High Pressure Mass Spectrometry, VI. Formation and Reaction of Negative Ions in Carbon Dioxide," J. Chem. Phys., Vol. 62, 1975, p. 2464.

41. Assumed equal to rate F36.

42. Fehsenfeld, F. C., and E. E. Ferguson, "Laboratory Studies of Negative Ion Reactions with Atmospheric Trace Constituents," J. Chem. Phys., Vol. 61, 1974, p. 3181.

43. Spjeldvik, W. N., and R. M. Thorne, "A Simplified D-Region Model and Its Application to Magnetic Storm After-Effects," J. Atmos. Terr. Phys., Vol. 37, 1975, p. 1313.

44. The rates involving C_5H_{12} are unknown. They have here been simply assumed to be quite rapid to avoid further complexities involving the unknown plasma chemistry of the C_5H_{12} ions.

45. Curve fit to data in Fig. 10 (this work).

46. Curve fit to data in Fig. 11 (this work). This rate represents 20% of the total rate of Fig. 11 (see p. 35 for comment).

47. Curve fit to data in Fig. 11 (this work). This rate represents 80% of the total rate of Fig. 11 (see p. 35 for comment).

48. Curve fit to data in Fig. 13 (this work).

49. Curve fit to data in Fig. 12 (this work).

50. Curve fit to data in Fig. 14 (this work).

51. Curve fit to data in Fig. 15 (this work).

52. Curve fit to data in Fig. 16 (this work).

53. Curve fit to data in Fig. 17 (this work).

54. Estimated at 10% of rate for process G12.

55. Estimate based on data in Gilmore, F. R., E. Bauer and J. W. McGowan, "A Review of Atomic and Molecular Excitation Mechanisms in Nonequilibrium Gases up to 20,000 K," J. Quant. Spectrosc. Radiat. Trans., Vol. 9, 1969, p. 157.

56. Estimated at 10% of rate for process G13.

57. Estimated at 10% of rate for process G16.

58. Processes H1 and H2 represent a compound rate. Curve fit data reviewed in: Center, R. E., J. F. Newton and D. C. Quimby, "Investigation of the High-Temperature Kinetics of the CO_2 Gas Dynamic Laser," AFWL-TR-77-59, Mathematical Sciences Northwest, Inc., Bellevue, Wash., July 1977.

59. Rosser, W. A., A. D. Wood and E. T. Gerry, "Deactivation of Vibrationally Excited Carbon Dioxide (ν_3) by Collisions with Carbon Dioxide or with Nitrogen," J. Chem. Phys., Vol. 50, 1969, p. 4996.

60. Kerber, R. L., N. Cohen and G. Emanuel, "A Kinetic Model and Computer Simulation for a Pulsed DF-CO_2 Chemical Transfer Laser," IEEE J. Quant. Elect., Vol. QE-9, 1973, p. 94.

61. Estimate (this work).

62. Sato, Y., S. Tsuchiya and K. Kuratani, "Shock-Wave Study of Vibrational Energy Exchange Between Diatomic Molecules," J. Chem. Phys., Vol. 50, 1969, p. 1911.

63. H8 and H9 represent a compound rate. Curve fit to data reviewed in Ref. 58.

64. Curve fit to data reviewed in Ref. 58.

65. Curve fit to data reviewed in: Stricker, J., "Deactivation of CO_2(010) and CO_2(001) by Hydrogen and Deuterium," J. Chem. Phys., Vol. 64, 1976, p. 1261.

66. Curve fit to data reviewed in: Anderson, J. D., "The Effect of Kinetic Rate Uncertainties in Gasdynamic Laser Performance," AIAA Paper No. 74-176, February 1974.

67. Garside, B. K., J. Reid, and E. A. Ballik, "TE CO_2 Laser Pulse Decay and Molecular Relaxation Rates," IEEE J. Quant. Elec., Vol. QE-11, 1975, p. 583.

68. Based on process H16, assuming v scaling.

69. Curve fit to data reviewed in: Lewis, P. F., and D. W. Trainor, "Survey of Vibrational Relaxation Data for O_2, N_2, NO, H_2, CO, HF, HCl, CO_2 and H_2O," AMP 422, Avco Everett Research Laboratory, Inc., Everett, Mass., November 1974.

70. Based on process H19, assuming v scaling.

71. Gower, M. C., and A. I. Carswell, "Vibration-Translation Rates in CO_2 Glow Discharges," Appl. Phys. Lett., Vol. 22, 1973, p. 321.

72. Based on process H22, assuming v scaling.

73. Based on process H25, assuming v scaling.

74. Based on process H28, assuming v scaling.

75. Taylor, R. L., "Energy Transfer Processes in the Stratosphere," Can. J. Chem., Vol. 52, 1974, p. 1436.

76. Miller, D. J., and R. C. Milikan, J. Chem. Phys., Vol. 53, 1970, p. 3384.

77. Whitson, M. E., and R. J. McNeal, "Temperature Dependence of the Quenching of Vibrationally Excited N_2 by NO and H_2O," J. Chem. Phys., Vol. 66, 1977, p. 2696.

78. Cohen, N., "A Review of Rate Coefficients for Reactions in the H_2-F_2 Laser Systems," SAMSO-TR-209, The Aerospace Corp., El Segundo, Calif., November 1972.

79. Baulch, D. L., D. D. Drysdale and D. G. Horne, Evaluated Kinetic Data for High Temperature Reactions – Vol. 2, Homogeneous Gas Phase Reactions of the H_2-N_2-O_2 System, Butterworth, London, 1973.

80. Garvin, D., and R. F. Hampson, eds., Chemical Kinetics Data Survey VII. Tables of Rate and Photochemical Data for Modeling of the Stratosphere (Revised), NBSIR 74-430, Washington, D. C., January 1974.

81. Jensen, D. E., and G. A. Jones, "Reaction Rate Coefficients for Flame Calculations," Tech. Report No. 35, Propellants, Explosives and Rocket Motor Establishment, Buckinghamshire, England, May 1977.

82. Shimazaki, T., and T. Ogawa, "A Theoretical Model of Minor Constituent Distributions in the Stratosphere Including Diurnal Variations," J. Geophys. Res., Vol. 79, 1974, p. 3411.

83. Howard, C. J., "Kinetics of the Reaction of HO_2 with NO_2," J. Chem. Phys., Vol. 67, 1977, p. 5258.

84. Inn, E. C. Y., "Rate of Recombination of Oxygen Atoms and CO at Temperatures Below Ambient," J. Chem. Phys., Vol. 61, 1974, p. 1589.

85. Slanger, T.G., B.J. Wood and G. Black, "Kinetics of $O(^3P)$ + CO + M Recombination," J. Chem. Phys., Vol. 57, 1972, p. 233.

86. Simonaitis, R., and J. Heicklen, "Kinetics and Mechanism of the Reaction of $O(^3P)$ with CO," J. Chem. Phys., Vol. 56, 1972, p. 2004.

87. Estimated at half the value given in Ref. 80, which is for a combustion environment.

88. Peeters, J., and G. Mahnen, "Reaction Mechanisms and Rate Constants of Elementary Steps in Methane-Oxygen Flames," Fourteenth Symposium (International) on Combustion, The Combustion Institute, Pittsburgh, 1973, p. 133.

89. Westenberg, A.A., and N. de Haas, "Measurement of the Rate Constants for $H + H_2CO \rightarrow H_2 + HCO$ at 297-652°K," J. Chem. Phys., Vol. 76, 1972, p. 2213.

90. Demerjian, K.L., J.A. Kerr, and J.G. Calvert, "The Mechanism of Photochemical Smog Formation," Adv. Environ. Sci. and Technology, Vol. 4, 1974, pp. 1-262. J.N. Pitts, Jr., and R.L. Metcalf, eds., Wiley-Interscience, New York.

91. Morris, E.D., Jr., and H. Niki, "Reaction of Methyl Radicals with Atomic Oxygen," Internatl. J. Chem. Kinet., Vol. 5, 1972, p. 47

92. Assumed equal to the rate for process K5.

93. , D.J., and J.S. Chang, "Sensitivity of Time-Varying Parameters in Stratospheric Modeling," J. Geophys. Res., Vol. 80, 1975, p. 2637.

94. Estimated at 1/30 the collision frequency, based on low k for the ternary analogous process $HO_2 + NO_2 + M$.

95. Lloyd, A.C., "Evaluated and Estimated Kinetic Data for Gas Phase Reactions of the Hydroperoxyl Radical," Typescript, Univ. of California, Riverside, October 1973, (as cited in Ref. 80).

96. Garvin, D., and R.F. Hampson, eds., Reaction Rate and Photochemical Data for Atmospheric Chemistry – 1977, NBS Special Publication 513, May 1978.

97. Estimated equal to rate for process K21 ($N + O_3$ reaction).

98. Slanger, T.G., B.J. Wood and G. Black, "Investigation of the Rate Coefficient for $O(^3P) + NO_2 \rightarrow O_2 + NO$," Int. J. Chem. Kinetics, Vol. 5, 1973, p. 615.

99. Garvin, D., and R.F. Hampson, eds., "Chemical Kinetic and Photochemical Data for Modeling Atmospheric Chemistry," NBS TN 866, U.S. Department of Commerce, June 1975.

100. Gardiner, W.C., Jr., W.G. Mallard and J.H. Owen, "Rate Constant of $OH + H_2 \rightleftharpoons H_2O + H$ from 1350 to 1600 K," J. Chem. Phys., Vol. 60, 1974, p. 2290.

101. Estimate based on rate for process K29 (Ref. 93).

102. Wilson, W.E., "A Critical Review of the Gas-Phase Reaction Kinetics of the Hydroxyl Radical," J. Phys. Chem. Ref. Data, Vol. 2, 1973, p. 535.

103. Huie, R.E., and J.T. Herron, "The Rate Constant for the Reaction O_3 + $NO_2 \rightarrow O_2$ + NO_3 Over the Temperature Range 259-362°K," Chem. Phys. Lett., Vol. 27, 1974, p. 411.

104. According to Ref. 9, the rate constant for process B2 is 1.0 (-31). Comparison of experimental and theoretical results (this work) suggests the value given, obtained by multiplying with 0.5 and attaching T^{-1} dependence such that k = 0.5 (-31) at 300 K.

105. Kieffer, L.J., "A Compilation of Electron Collision Cross Section Data for Modeling Gas Discharge Lasers," JILA Report 13, Univ. of Colorado, Boulder, Colorado, September 1973.

DISTRIBUTION LIST

1. Defense Advanced Research Projects Agency — 1
   1400 Wilson Blvd.
   Arlington, VA 22209
   ATTN: LT COL Malcom R. O'Neill

2. ODDR&E — 1
   The Pentagon
   Washington, DC 20301
   ATTN: Ass't. Dir. (Space and Adv. Systems)

3. NASA-Lewis Research Center — 1
   21000 Brookpark Road
   Cleveland, OH 44135
   ATTN: Dr. John W. Dunning, Jr.

4. Defense Documentation Center — 2
   Cameron Station
   Alexandria, VA 22314

5. Department of the Army — 1
   DCSRDA
   Washington, DC 20310
   ATTN: DAMA-WSM-A (LTC Holmes)

6. Commander — 10
   US Army Missile Command
   Redstone Arsenal, AL 35809
   ATTN: DRSMI-RHS, Mr. Charles Cason

7. Commander — 1
   US Army Mobility Equipment R&D Center
   Ft. Belvoir, VA 22060
   ATTN: DRDME-R

8. Commander — 1
   US Army Electronics Command
   Ft. Monmouth, NJ 07703
   ATTN: DRSEL-CT-L (Dr R.G. Buser)

9. Project Mgr, High Energy Laser Project — 1
Naval Sea Systems Command
Washington, DC 20362
ATTN: CPT James G. Wilson, PMS 405

10. Air Force Weapons Laboratory — 4
Kirtland AFB, NM 87117
ATTN: Dr. John Filcoff

11. AF Aero Propulsion Laboratory — 1
Wright-Patterson AFB, OH 45356
ATTN: LT COL Bobbie L. Jones

12. Commander — 1
Naval Surface Weapons Center
Silver Spring, MD 20910
ATTN: Dr. Walt Graham, WA-21

13. Director — 1
Ballistic Missile Defense Advanced Technology Center
P.O. Box 1500
Huntsville, AL 35807
ATTN: Dr. Michael Lavan

14. Director — 1
Ballistic Missile Defense Advanced Technology Center
P.O. Box 1500
Huntsville, AL 35807
ATTN: Mr. J.D. Carlson

15. Aerospace Corporation — 1
P.O. Box 92957
Los Angeles, CA 90009
ATTN: Dr. Walter Warren

16. Airesearch Manufacturing Company — 1
2525 West 190th Street
Torrance, CA 90503
ATTN: Mr. A. Colin Stancliffe

17. AVCO-Everett Research Lab — 2
2385 Revere Beach Parkway
Everett, MA 02149
ATTN: Dr. Jack Daugherty

18. Battelle Columbus Laboratories 1
505 King Avenue
Columbus, OH 43201
ATTN: Mr. Fred Tietzel (STOLAC)

19. Hughes Research Laboratories 1
3011 Malibu Canyon Road
Malibu, CA 90265
ATTN: Dr. Authur N. Chester

20. Hughes Aircraft Company 1
Centinela and Teale Streets
Culver City, CA 90230
ATTN: Dr. Eugene Peressini (Bldg. 6, MS/E-125)

21. Lawrence Livermore Laboratory 1
P.O. Box 808
Livermore, CA 94550
ATTN: Dr. John Emmett

22. Los Alamos Scientific Labs 1
P.O. Box 1663
Los Alamos, NM 87544
ATTN: Dr. Keith Boyer (MS 530)

23. Mathematical Sciences Northwest, Inc. 1
4545 15th Avenue, NE
Seattle, WA 98105
ATTN: Mr. Peter H. Rose

24. Massachusetts Institute of Technology 1
Lincoln Lab
P.O. Box 73
Lexington, MA 02173
ATTN: Dr. Shin Shey

25. Northrop Corporation 1
3401 West Broadway
Hawthorne, CA 90250
ATTN: Dr. Gerard Hasserjian

26. Rockwell International Corporation 1
Rocketdyne Division
6637 Canoga Avenue
Canoga Park, CA 91304
ATTN: Marc T. Constantine

27. Science Applications, Inc. 1
6666 Powers Ferry Road, Suite 202
Atlanta, GA 30339

ATTN: Mr. Harvey Ford

28. Systems, Science and Software 1
P.O. Box 4803
Hayward, CA 94540

ATTN: Mr. Alan F. Klein

29. United Technologies Research Center 1
400 Main Street
East Hartford, CT 06108

ATTN: Mr. Bob Bullis

30. Westinghouse Electric Corporation 1
Defense and Space Center
Friendship International Airport, Box 746
Baltimore, MD 21203

ATTN: Mr. W.F. List